

Experimental and Model-based Investigations on Gas Crossover in Polymer Electrolyte Membrane Water Electrolyzers

Von der Fakultät für Elektrotechnik und Informatik
der Gottfried Wilhelm Leibniz Universität Hannover
zur Erlangung des akademischen Grades
Doktor-Ingenieur
(abgekürzt: Dr.-Ing.)
genehmigte Dissertation

von Herrn
M. Sc.
Patrick Trinke

geboren am 19.01.1989
in Soltau

2021

1. Referent: Prof. Dr.-Ing. Richard Hanke-Rauschenbach
2. Referent: Prof. Dr.-Ing. Thomas Turek
Tag der Promotion: 27.05.2020

Abstract

Gas crossover of the product gases, hydrogen and oxygen, through the thin membranes of polymer electrolyte membrane (PEM) water electrolyzers is a major challenge for its further commercialization. It causes safety issues, efficiency losses and triggers degradation mechanisms. In particular, the effects on gas crossover during PEM water electrolysis are not fully understood yet. In the context of the present work, these effects will be investigated experimentally and model-based.

In the first part of the dissertation the influences of different operating conditions: pressure, temperature as well as current density and changes of the electrode structure on gas crossover are experimentally investigated. It is shown that both hydrogen and oxygen crossover increase strongly with current density. However, an increase of the cathode pressure shows no significant influence on the qualitative extent of this correlation. Thus it is assumed that the underlying mechanisms for this crossover increase are also independent of pressure. This finding stands in contrast to the common explanation in the literature. It is commonly assumed that the crossover increases due to local pressure enhancements. However, since gas transport in general is strongly dependent on pressure this approach contradicts the experimental findings. An alternative explanatory approach is discussed within this work, in which the focus is on the transport of dissolved gases from the catalyst particles through the ionomer to the pore space. Transport limitations on this path, which are independent of pressure, lead to supersaturated dissolved gas concentrations. These concentrations increase with current density, which leads to higher concentration gradients across the membrane and thus to gas crossover increases. The experimental variation of the cathode ionomer content supports this explanation approach. Higher ionomer contents lead to significantly steeper crossover increases, which can be explained by the increase of the transport resistances due to thicker ionomer films. The investigation of the cell voltage reveals a direct correlation of the increased crossover and mass transport based voltage losses.

In the second part, a comprehensive one-dimensional model is formulated to investigate the experimental findings in more detail. The focus is on the previously described theory of supersaturated dissolved gas concentration within the catalyst layers. The simulation results based on literature parameters strengthen this theory. The local profiles reveal that the supersaturated concentrations occur directly at the membrane/catalyst layer interfaces, where the local gas formation is maximal. Furthermore, the complex interactions between ohmic, kinetic and mass transport losses of the catalyst layers are investigated. Finally, the gas crossover is studied by a system consideration with regard to safety and efficiency.

Keywords: PEM water electrolysis; gas crossover; modelling; safety issue; hydrogen in oxygen

Kurzfassung

Der Gas Crossover der Produktgase, Wasserstoff und Sauerstoff, durch die dünnen Membranen von Polymer Elektrolyt Membran (PEM) Wasserelektrolyseuren ist ein Hindernis für deren Kommerzialisierung. Diesbzüglich besteht ein großes Potential in der Lösung von Sicherheitsproblemen, der Reduzierung von Wirkungsgradverlusten und der Identifikation von Degradationsmechanismen. Dabei sind vor allem die Effekte während des Elektrolysebetriebs noch nicht vollständig verstanden. In Rahmen der vorliegenden Dissertation werden diese Effekte experimentell und modelltheoretisch untersucht.

Im ersten Teil werden die Einflüsse von unterschiedlichen Betriebsbedingungen: Druck, Temperatur und Stromdichte sowie Veränderungen von der Elektrodenstruktur, am Beispiel der Änderung des Ionomergehalts in der Kathoden-Katalysatorschicht, auf den Gas Crossover experimentell untersucht. Es zeigt sich, dass sowohl der Wasserstoff sowie der Sauerstoff Crossover mit der Stromdichte stark ansteigen. Eine Erhöhung des Kathodendrucks hat allerdings keinen signifikanten Einfluss auf die Crossoverzunahme. Daher wird vermutet, dass die zugrundeliegenden Ursachen für diese Crossovererhöhung druckunabhängig sind. Dieser Befund steht im Gegensatz zur gängigen Erklärung in der Literatur. Bis jetzt wurde davon ausgegangen, dass der Crossover aufgrund von lokalen Druckerhöhungen ansteigt. Allerdings ist der Gastransport selbst stark druckabhängig und somit kann dieser Ansatz die Messwerte qualitativ nicht beschreiben. In der vorliegenden Arbeit wird ein neuer Erklärungsansatz diskutiert, bei dem der Transport gelöster Gase von den Katalysatorpartikeln durch das Ionomer zum Porenraum im Fokus steht. Durch Transportlimitierungen führt dieser druckunabhängige Transport zu übersättigten Konzentrationen in den Katalysatorschichten. Diese Gaskonzentrationen sind je höher desto größer die angelegte Stromdichte ist und in Folge dessen steigt der Gas Crossover an. Experimente mit geänderten Ionomerbeladungen unterstützen diese Theorie. Höhere Ionomergehalte erhöhen die Transportlimitierungen durch dickere Ionomerschichten, die wiederum zu einer stärkeren Erhöhung des Gas Crossovers führen. Gleichzeitig wird auch der Effekt der Variation des Ionomergehalts auf die Zellspannung untersucht und die Korrelation zwischen Crossovererhöhung und Stofftransport basierten Spannungsverlusten gezeigt.

Im zweiten Teil wird ein umfangreiches, eindimensionales Modell formuliert, um die experimentellen Ergebnisse detaillierter zu analysieren. Dabei liegt der Fokus auf der vorher beschriebenen Theorie der Übersättigung von gelösten Gasen in den Elektroden. Die auf Literaturparametern basierenden Simulationsergebnisse unterstützen diese Theorie. Vor allem entstehen die Übersättigungen direkt an den Membran/Katalysatorgrenzen, da dort die lokalen Gas-Entstehungsraten am größten sind. Des Weiteren werden die komplexen Zusammenhänge zwischen ohmschen, kinetischen und Stofftransport-Spannungsverlusten in den Katalysatorschichten untersucht. Abschließend wird der Gas Crossover unter Systemaspekten hinsichtlich Sicherheit und Wirkungsgrad betrachtet.

Schlagnote: PEM Wasserelektrolyse; Gas Crossover; Modellierung; Sicherheitsproblem; Wasserstoff in Sauerstoff

Contents

Abstract	III
Kurzfassung	IV
1 Introduction	1
2 State of the Art of PEM Water Electrolysis	3
2.1 Working Principle, Cell Setup and Operating Behavior	3
2.1.1 Working Principle and Cell Setup	3
2.1.2 Cell Performance and Polarization Behavior	7
2.1.3 Faraday Efficiency	9
2.2 Fundamentals of Gas Crossover	10
2.2.1 Gas Crossover Mechanisms	11
2.2.2 Gas Crossover Dependencies	13
2.3 Critical Discussions of recent Findings	15
2.3.1 Hydrogen in Oxygen Content	15
2.3.2 Calculation of the Hydrogen Crossover	16
2.3.3 Initial Considerations to the Crossover Increase	18
2.4 Research Questions	21
3 Experimental Setup	23
3.1 Test Bench	23
3.2 Sensors, Instrumentation and Methods	24
3.2.1 Measurement Devices	24
3.2.2 Measurement Procedures	25
3.3 Test Cells	26
3.4 Materials	27
3.4.1 Porous Transport Layers	28
3.4.2 Catalyst Coated Membranes	28
4 Effect of Current Density on Gas Crossover	30
4.1 Current Density Effect on Hydrogen Crossover	31
4.1.1 Comparison to Literature Results	31
4.1.2 Temperature Variation	33
4.1.3 Pressure Variation	34
4.2 Theoretical Explanation – Supersaturation of dissolved Hydrogen	35
4.3 Oxygen Crossover	39
4.4 Concluding Remarks	43

5	Influence of Ionomer Content on Crossover and Cell Performance	45
5.1	Ionomer Variation	45
5.2	Effect on Hydrogen Crossover	47
5.3	Effect on Cell Performance	51
5.3.1	Differences in Cell Voltage	51
5.3.2	Mass Transport Losses	53
5.3.3	Mass Transport free Tafel Analysis	54
5.4	Concluding Remarks	56
6	Model Formulation and Validation	58
6.1	Potential Fields	58
6.2	Concentration Fields	60
6.2.1	Dissolved Gases	60
6.2.2	Dissolved Water Content	63
6.2.3	Gases and Liquid Water	65
6.3	Temperature Field	68
6.4	Base Case Parameter Set	69
6.5	Model Base Case Results	71
6.5.1	Integral Cell Behavior	71
6.5.2	Local Profiles	72
6.6	Concluding Remarks	76
7	Model-based Investigations	77
7.1	Influences of the different Transport Mechanisms	77
7.2	Voltage Loss Breakdown	80
7.3	Cathode Pressure Variation	83
7.4	Ionomer Variation	85
7.5	System Considerations	90
7.5.1	Cell Efficiency	90
7.5.2	Operating Window	93
7.6	Concluding Remarks	94
8	Summary, Conclusion and Outlook	96
	References	101
	A Supporting Equations	110
	List of Abbreviations and Symbols	113
	Scientific career	116
	Publications and Statements on Authorship	119

1 Introduction

The global warming is one of the most important issues of the 21st century humanity has to deal with, due to the immense challenges that the corresponding climate change will bring, e. g. the significant and complex changes of the ecosystems [1] or the migration of environmental refugees due to droughts, desertification, sea level rise and disruption of seasonal weather patterns [2]. The target of the Paris Agreement¹ is to keep the temperature rise below 2 °C compared to a pre-industrial level [3]. To achieve this, it is essential to reduce the greenhouse gas emissions significantly. Exemplary, Germany's climate action plan contains a reduction of the greenhouse gas emissions to at least 20 % until 2050 compared to the greenhouse gas emissions of 1990 [4]. Following, it is necessary to transform the fossil-fuel economy into a low-fossil-fuel economy. In this context, hydrogen from renewable sources will be able to contribute a significant share due to the following potentials of hydrogen: i) defossilization of the mobility, ii) substitution of fossil-based raw materials in the primary industry/chemical industry, iii) defossilization of the heat sector, iv) supporting the electric transport infrastructure and reducing the necessary expansion of the electricity grid and v) long-term storage of renewable energy [5].

This hydrogen from renewable sources can be produced by the electrolysis of water, which is the electrochemical splitting of water into hydrogen and oxygen due to electrical and thermal energy. The electrolysis of water can be realized by the following three technologies: i) at high temperatures (500–900 °C) via solid oxide electrolysis (SOE) [6] and at low temperatures (20–100 °C) by ii) alkaline water electrolysis (AEL) and iii) polymer electrolyte membrane (PEM) water electrolysis [7]. On latter is the focus of the present work.

Many advantages are ascribed to the PEM technology, such as operation at high current densities (large operational range), fast dynamics and high pressure operation even at differential pressure conditions [7–9], under which hydrogen and oxygen can be produced at different pressure levels. Nevertheless, the PEM water electrolysis has also different challenges, such as life time issues due to degradation or high costs [8–10].

Another major challenge is the crossover of product gases through the thin membrane, which separate the two compartments in which the gases are produced. The crossover of hydrogen to the oxygen side and the crossover of oxygen to the hydrogen side are critical issues for the further commercialization of PEM water electrolysis [10], due to the following three problems: i) safety issues [11–14], ii) efficiency losses [11–14] and iii) degradation [15, 16]. These issues are described in more detail in the following.

Due to the hydrogen crossover from the cathode (hydrogen side) to the anode (oxygen side) the hydrogen enters the oxygen compartment, which leads to a gas mixture of

¹Agreement of the 21st Conference of the parties of the United Nations Framework Convention on Climate Change in Le Bourget, signed by 195 members.

hydrogen and oxygen. Since the lower explosion limit (LEL) of hydrogen in oxygen is around 4 vol.% [17], this low value can lead to safety issues, which causes a negative part load behavior [10]. This is a problem that exists especially at high cathode pressures and thin membranes for low to moderate current densities [13,18]. Whereas, at higher current densities the increased oxygen evolution rate dilutes the hydrogen content.

In addition to this uneconomical part load behavior due to hydrogen crossover, the hydrogen crossover causes also a direct efficiency loss that can be described by the Faraday efficiency [11], which is the ratio of the actual hydrogen flux within the electrolyzer cathode outlet to the theoretical hydrogen flux (Faraday's laws of electrolysis) [19,20]. Consequently, the Faraday efficiency decreases with increasing crossover fluxes and is small at low current densities, but it increases towards higher current densities, since the ration of gas crossover flux to the theoretical flux decreases with increasing current density. The Faraday efficiency is usually very high (>95%)[11,14]. Nevertheless, at higher pressures and thin membranes the efficiency losses due to gas crossover are significantly increased [13].

The third issue concerning gas crossover is the trigger for degradation mechanisms. Most degradation mechanisms in PEM water electrolysis are not fully understood yet [10,21], such as the degradation due to the formation of radicals or other harmful molecules due to unwanted side reactions [21], e. g. hydrogen peroxide, which was observed on the cathode side [15,16]. On this side, the permeated oxygen can react with the evolved hydrogen to form hydrogen peroxide [15]. This hydrogen peroxide causes degradation of the membrane and catalyst layer [15,16]. Consequently, the gas crossover can lead to degradation phenomena, if catalysts or feed water with metal ions (impurities) [22] are used, which enables negative side reactions.

The previously described gas crossover issues highlight the importance of this research topic in PEM water electrolysis. However, the gas crossover is not fully understood yet [10]. In the context of the present work the gas crossover is investigated experimentally and model-based in more detail during PEM water electrolysis operation. Within the next chapter the state of the art of PEM water electrolysis is described, such as the working principle, cell setup, electrochemical basics and fundamentals of gas crossover. This chapter also includes critical consideration of literature data. Following, the research questions of this dissertation are successively derived. Subsequently, the experimental setup is described in chapter 3. Then the experimental and model-based results of this dissertation are discussed within the chapters 4 to 7. First, the effect of current density on both, hydrogen and oxygen crossover is shown in chapter 4. The observed effects of chapter 4 are investigated experimentally in more detail in chapter 5. Therefore, cathode catalyst layers were specially designed to investigate the effect of mass transport resistances within the cathode catalyst layer on hydrogen crossover as well as the effects and correlations on the electrochemical performance. Chapter 6 includes the formulation of the physical model, which is applied in chapter 7 for the model-based investigation of the experimental findings of chapter 4 and 5. Furthermore, the model is used to investigate system considerations concerning the cell efficiency and safety issue. Finally, the findings are summarized in chapter 8 by recalling the research questions.

2 State of the Art of PEM Water Electrolysis and Critical Considerations to the Gas Crossover

In this chapter the fundamentals and state-of-the-art information on polymer electrolyte membrane (PEM) water electrolysis are described with focus on gas crossover. The first section is about the working principle, typical cell setup and polarization behavior. Within the second section the fundamentals of the main topic gas crossover are described. In section 2.3 recent experimental findings according the hydrogen crossover are critically discussed. At the end of this chapter the research questions for this work are derived based on the given state-of-the-art information and critical discussion concerning the literature data.

2.1 Working Principle, Cell Setup and Operating Behavior

In general the electrolysis of water is the electrochemical splitting of water into molecular oxygen and hydrogen by use of thermal and electrical energy [7,9]. A typical layer based cell setup has been established for the technical implementation of PEM water electrolysis. The working principle and the typical cell setup are described within the next subsection. Subsequently, the electrochemical cell performance, polarization behavior and Faraday efficiency are described.

2.1.1 Working Principle and Cell Setup

On the left hand side of Fig. 2.1 the typical setup of a PEM water electrolysis cell is shown and on the right hand side reaction equations and state-of-the-art material information are given. In the center of the water electrolysis cell is the PEM. It separates the cell into two half-cells, the anode (oxygen side) and cathode (hydrogen side). The water electrolysis cells are designed symmetrically, with the catalyst layers (CLs) on both sides next to the membrane, followed by porous transport layers (PTLs) and completed by flow fields [8,9]. The catalyst layers are often placed on the membrane by different techniques, e. g. decal method or spray coating [8]. This unit is called catalyst coated membrane (CCM) as well as membrane electrode assembly (MEA).

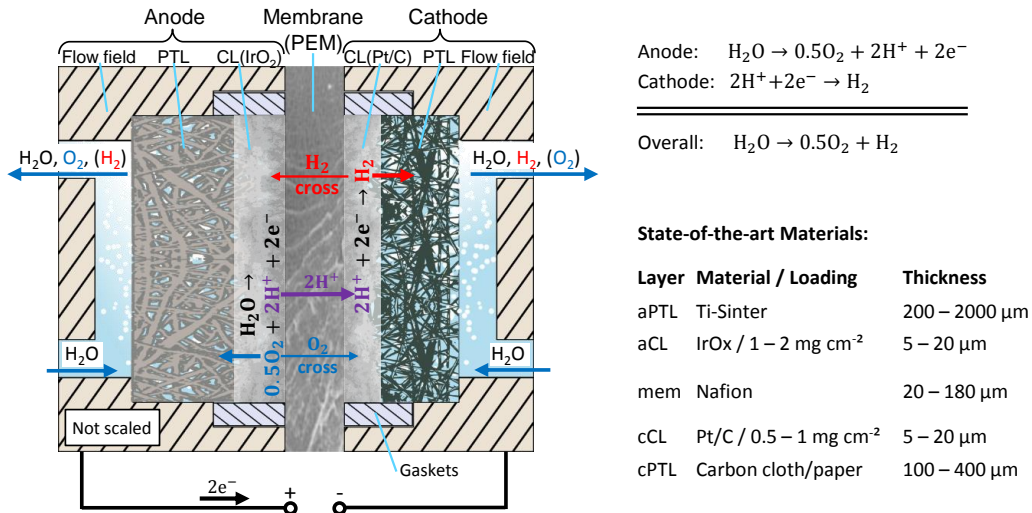


Figure 2.1: Scheme of a PEM water electrolysis cell with information to the state-of-the-art materials. Additionally, the important fluxes are sketched, e. g. hydrogen and oxygen crossover.

The anode is fed with deionized (DI) water, which is flowing through the flow field towards the PTL. Because of capillary forces the liquid water penetrates the PTL. At the anode CL the water is oxidized to molecular oxygen, protons and electrons by applying a voltage on the electrical connections. The membrane is capable to transport the protons to the cathode CL, but it is an electronic insulator. Consequently, the electrons are conducted through the electrical connections towards the cathode CL, where the protons and electrons reduce to molecular hydrogen. The removal of the produced gases and excess water is realized by the PTLs. A small part of the produced gases permeates through the thin membrane. This transport is called gas crossover. In the following each layer of the typical cell setup is described in more detail concerning the tasks, state-of-the-art information and important research topics, whereby due to the symmetric sandwich design the cell is described from the outer layers towards the membrane.

Flow Fields The flow fields support the inner cell layers as a mechanical backup and they have to ensure that the active area is homogeneously pressed to reduce contact resistances. Often the sealing system is also integrated within the flow fields by O-rings, which are often made out of Viton [18] or flat gaskets, such as PTFE gaskets sheets [23, 24]. Depending on the definition and system, the flow fields are also called bipolar plates (in a cell stack) or sometimes the flow fields are implemented in the end plates or current collectors.

Another main task of the flow fields is the transport of feed water to the active are and the removal of the water/gas mixtures. This is often realized by a flow field with lands and channels [8, 9]. Therefore, the design of the flow field is an important research topic [25, 26]. It is also possible to substitute the classical flow fields structures [27, 28], e. g. by expanded metals [18]. In the following, only the typical flow field design is considered.

The flow fields need high electron and thermal conductivities to transport the current and heat, which is generated by irreversible processes. In contrast to fuel cells a cooling system is often not included within the flow field plates, since the liquid feed water is used for this task.

Because of the high potentials on the anode side, the flow fields have to be made out of materials with a high thermodynamic stability. Often Titanium is used [8, 9], but also other materials/alloys [29] and also protective coatings [29–32] are important research topics to reduce costs, contact resistances and increase the durability. On the cathode side the potentials are lower. Consequently, it is possible to use more materials, such as graphite or stainless steel [8, 33], which is used within PEM fuel cells [33, 34]. However, it is not typical to use different materials for the flow fields/bipolar plates on the cathode and anode side of PEM water electrolysis stacks. Consequently, the flow fields of PEM water electrolysis stacks are commonly made out of titanium, which can cause the problem with hydrogen embrittlement [35].

Porous Transport Layers The porous transport layers (PTLs) have also the same tasks as the flow fields: transport of i) current, ii) water/gas mixtures, iii) heat and iv) the mechanical support of the MEAs. Therefore, thin porous structures are used. The pores of the PTLs have diameters of several micro meters, which is enough for the fluid transport and the fine solid structure realize a good electrical contact to the catalyst layers.

For the anode side titanium is used, because of the high thermodynamic stability as previously stated. These titanium PTLs are typically manufactured by sintering of titanium powder or fibres, but also titanium foams or titanium expanded metals [8, 10, 36] are used. Typical thicknesses of anode PTLs are 0.2 – 2 mm with pore diameters around 50 μm [37].

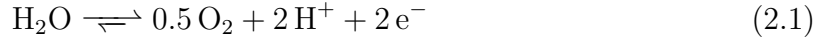
On the cathode side carbon based PTLs are used. Most cathode PTLs were originally developed for the application in PEM fuel cells, where PTLs are called gas diffusion layers (GDLs). The cathode PTLs are manufactured as papers or cloths [8, 9] with typical thicknesses between 100 – 400 μm and mean pore diameters of 0.8 – 34 μm [38]. To improve the electrical contact to the catalyst layers some carbon PTLs consist also of micro porous layers (MPLs) [39]. For a better gas/water transport the carbon PTLs have also hydrophobic treatments, e. g. PTFE [40, 41].

Main research topics for the PTLs are currently optimizing the structure to improve gas/water transport [42, 43], to reduce contact resistances, e. g. by applying MPLs [28, 44, 45] and to decrease production costs [28, 30]. Especially, for the anode PTLs main interests are to find other materials/alloys instead of titanium or to use coatings [46], which is very similar to the previously discussed research effort of flow fields.

Catalyst Layers Within the catalyst layers (CLs) the electrochemical reactions take place. These layers are also porous structures as the PTLs, but much finer to increase the volume specific surface of the catalyst particles, which lead to a higher electrochemical performance. The catalyst layers consist of a proton conducting phase, e. g. Nafion,

the pore volume to transport the gas/water mixture and the catalyst particles. These catalyst particles have two tasks, i) enabling the specific electrochemical reaction and ii) transport of electrons. The latter task can also be supported by a carrier material, such as carbon for the cathode [8] and titanium based materials for the anode [23, 47, 48].

The catalyst layers are very thin, typically several micro meters [23]. On the anode side the oxygen evolution reaction (OER) takes place, which is stated in the following equation:



The OER is sluggish and therefore this reaction leads to very high kinetic losses. Quite high catalyst loadings are currently necessary to keep the kinetic losses as low as possible, such as 2 mg cm^{-2} of iridium based catalyst [8], which is the state-of-the-art catalyst material. Unfortunately, iridium is an expensive material. Consequently, due to the high activation overpotentials and the high price, improving the catalytic efficiency while reducing the catalyst loading [49] or the development of other catalysts are of high research interest. However, this is not easy, because of the harsh conditions due to the acidic environment and high half-cell potentials. For example ruthenium is also a good catalyst [50], but it is not stable under these conditions [51].

On the cathode side the hydrogen evolution reaction (HER) takes place:



For this reaction platinum is a very good catalyst material. Often platinum on advanced carbon is used with loadings of $0.5 - 1 \text{ mg cm}^{-2}$ [8]. The kinetic losses of the HER are small in comparison to the overpotentials of the sluggish OER. However, reducing the catalyst loading [52] or the development of platinum free catalysts [53, 54] are also of high research interest.

Membrane Core of each PEM water electrolysis cell is the eponymous polymer electrolyte membrane. This layer has three tasks, namely i) transport of protons from the anode to the cathode catalyst layer, ii) separating both half-cells, so that the produced hydrogen and oxygen do not enter the other sides and iii) electrical insulation of the half-cells. Consequently, the membrane materials should have the following properties: a high proton conductivity, small gas permeabilities (gas-tight) and a high electric resistance, but it also needs further properties, such as high chemical, thermal stabilities and high mechanical strength. The state-of-the-art material is Nafion (Chemours) a perfluorosulfonic acid (PFSA) membrane, but there exists also other membrane manufactures as 3M, Gore or Fumatech. The improvement of existing membranes, e. g. with additives [55, 56] or reinforcements [57, 58] and the development of improved, reliable membranes [59–61] are very important research topics.

The PFSA membranes consist out of polymer backbones and sulfonic acid end-groups ($\text{R}-\text{SO}_2-\text{OH}$, R stands for the polymer backbone). The end-groups enable the proton transport, which takes place via Vehicle and Grotthuss mechanism [62, 63]. For a good proton conductivity the PFSA membranes have to be well humidified [64–66],

which is realized through the liquid water feed during PEM water electrolysis. PFSA membranes immersed into liquid water have relatively high water uptakes (over $\lambda = 20 \text{ mol}_{\text{H}_2\text{O}} \text{ mol}_{-\text{SO}_3\text{H}}^{-1}$ [64]) and consequently they are swelling strongly, e. g. 10 – 15 % in through plane direction for a N212 membrane [67].

Typical membrane thicknesses are between 20 and 180 μm . Whereby, the trend is going to thin membranes to reduce the proton resistances, but this is an ongoing challenge, since thinner membranes have shorter lifetimes and the thinner the membrane the higher the hydrogen and oxygen crossover that can lead to the following three problems: i) safety issues, ii) efficiency losses and iii) degradation, which are discussed in the introduction. The previously mentioned membrane lifetime problem is a very important topic and yet not fully understood [10, 21].

2.1.2 Cell Performance and Polarization Behavior

The overall cell efficiency of produced hydrogen η_{cell} is the product of the voltage efficiency η_U and the Faraday efficiency of hydrogen η_{H_2} Eq. (2.3). The thermal efficiency is not considered within this Equation, consequently the cell efficiency of this dissertation is based on the lower heating value (reversible cell voltage) instead of the higher heating value (thermoneutral cell voltage).

$$\eta_{\text{cell}} = \eta_U \eta_{\text{H}_2} \quad (2.3)$$

For PEM water electrolysis a voltage efficiency η_U of 64 – 76 % (based on the reversible cell voltage) is targeted before 2030 [68]. The voltage efficiency η_U can be calculated by the following equation:

$$\eta_U = \frac{U_{\text{rev}}}{U_{\text{cell}}} \quad (2.4)$$

where U_{rev} is the reversible cell voltage according to the operating conditions. The reversible cell voltage describes the minimal cell voltage that is required to split water electrochemically, which can be calculated by the Nernst equation [69, 70]:

$$U_{\text{rev}} = U_{\text{rev}}^0(T) + \frac{RT}{zF} \ln \left(\frac{a_{\text{Ox}}}{a_{\text{Red}}} \right) \quad (2.5)$$

where R is the gas constant, z is the number of electrons transferred in the cell reaction, F is the Faraday constant and U_{rev}^0 is the reversible cell voltage at standard conditions as a function of temperature T according to the Gibbs free energy ΔG^0 [8]:

$$U_{\text{rev}}^0 = \frac{\Delta G^0}{zF} \quad (2.6)$$

At standard conditions and 25 °C the reversible cell voltage of the electrolysis of is 1.23 V [8].

In a real PEM water electrolysis cell the applied cell voltage is higher as the reversible cell voltage due to different irreversible processes and it increases with current density.

This polarization behavior is schematically shown in Fig. 2.2. The polarization curve can be separated into three regions. The first region at low current densities is predominated by activation overpotentials with a logarithmic correlation [23]. The second region from moderate to high current densities shows a linear trend, which originates from the ohmic losses [23] and the third region usually only becomes apparent at very high current densities, when mass transport losses strongly increase [71].

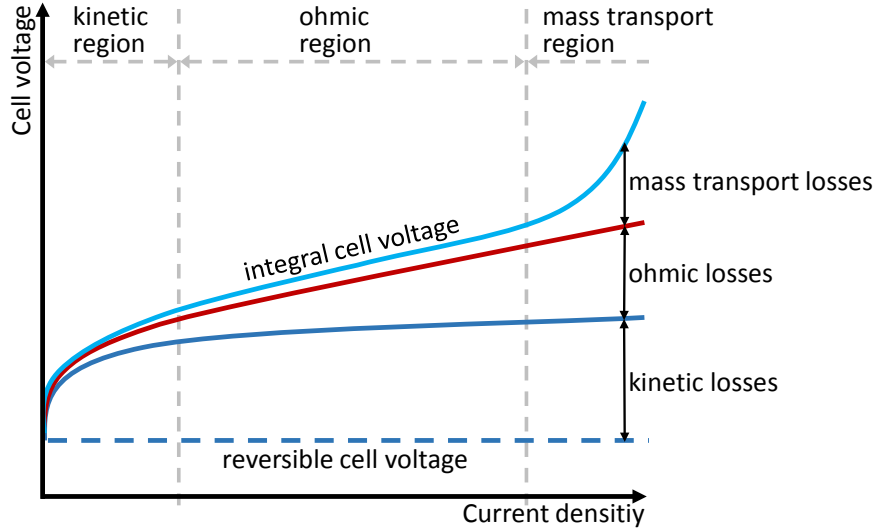


Figure 2.2: Schematic polarization behavior of a PEM water electrolysis cell. Allocating the overpotentials into kinetic η_{act} , ohmic η_{ohm} and mass transport losses η_{mt} .

Fig. 2.2 shows also a cell voltage breakdown. The different voltage losses are indicated between the cell voltage U_{cell} and the reversible cell voltage U_{rev} . The single voltage loss terms are stated in more detail in the following equation:

$$U_{cell} = U_{rev} + \underbrace{i \left(R^{mem} + R_{el} + R_{H^+}^{a,eff} + R_{H^+}^{c,eff} \right)}_{\text{ohmic losses}} + \underbrace{\eta_{act}^a + |\eta_{act}^c|}_{\text{kinetic losses}} + \underbrace{\eta_{mt}}_{\text{mass transport losses}} \quad (2.7)$$

where, R^{mem} is the membrane resistance of the proton transport, R_{el} the electrical resistances of the cell including also the contact resistances between each layer, $R_{H^+}^{a,eff}$ and $R_{H^+}^{c,eff}$ the effective proton resistances of the anode and cathode catalyst layer, respectively. The kinetic losses are represented by the activation overpotentials of each half-cell reaction η_{act}^a and η_{act}^c and lead to the mass transport losses represented by η_{mt} . The single electrochemical performance losses are described in the following.

Kinetic Losses The activation overpotentials η_{act} of both half-cell reactions can be described by the Butler-Volmer approach [69, 70]:

$$i = i_0 \left[\exp \left(\frac{\alpha_{ox} F}{RT} \eta_{act} \right) - \exp \left(-\frac{\alpha_{red} F}{RT} \eta_{act} \right) \right] \quad (2.8)$$

herein i_0 is the exchange current density, α_{ox} and α_{red} the charge transfer coefficients of the oxidation and reduction reaction of the respective half-cell reaction. At high current densities, when the current density is significantly higher than the exchange current density, the Butler Volmer equation can be simplified by the Tafel equation [69, 70]:

$$\eta_{\text{act}} = b \log \left(\frac{i}{i_0} \right) \quad (2.9)$$

where b is the Tafel slope, which includes the charge transfer coefficient of the rate determining step [69, 70].

The activation overpotential of the anode side is much higher because of the sluggish OER [8]. The determined Tafel slope of the iR -free cell voltage are published in the range of 38.9 mVdec^{-1} [72] to 81 mVdec^{-1} [73] and the exchange current density is reported in various ranges: $1.548 \cdot 10^{-3} - 1 \cdot 10^{-12} \text{ A cm}^{-2}$ [8]. For example a Tafel slope of 81 mVdec^{-1} [73] and an exchange current density of $8 \cdot 10^{-6} \text{ A cm}^{-2}$ [73] result in an activation overpotential of 423 mV at a current density of 1 A cm^{-2} .

Ohmic Losses Ohmic losses result due to protonic and electric resistances. The main part of the ohmic losses are caused by the membrane and contact losses [73]. Typically, the protonic membrane and electrical resistances are measured by the electrochemical impedance spectroscopy (EIS) [23]. Active area specific resistances R_{HFR} are measured in ranges of $50 \text{ m}\Omega \text{ cm}^2$ (N212) [23] to $250 \text{ m}\Omega \text{ cm}^2$ (N117) [73]. Consequently, the voltage losses are in ranges $50 - 250 \text{ mV}$ at a current density of 1 A cm^{-2} .

Mass Transport Losses Mass transport overpotentials occur, when the water transport towards the anode catalyst layer or the removal of the evolved gases, hydrogen and oxygen, are hindered. These mass transport overpotentials can be caused by the following mechanisms: i) increases in thermodynamic cell potentials (Nernst equation (2.5)), ii) increased kinetic losses and iii) higher ohmic losses. The first two effects originate from reduced water and increased gas activities. The latter effect becomes important, when the membrane or catalyst layers are not fully humidified, e. g. when not enough feed water is supplied [71]. The mass transport losses are reported in ranges of $20 - 60 \text{ mV}$ [73] at a current density of 1 A cm^{-2} .

2.1.3 Faraday Efficiency

In addition to the previously described predominant voltage losses, also other losses exist, which are included in the Faraday efficiency [20]. The Faraday efficiency of hydrogen η_{H_2} can be expressed by the following equation:

$$\eta_{\text{H}_2} = \frac{N_{\text{H}_2}^{\text{c,out}}}{N_{\text{H}_2}^{\text{theo}}} = 1 - \frac{N_{\text{H}_2}^{\text{cross}} + N_{\text{H}_2}^{\text{recomb}} + \frac{i_{\text{short}}}{2F}}{\frac{i}{2F}} \quad (2.10)$$

where $N_{\text{H}_2}^{\text{c,out}}$ is the actual molar flux of hydrogen at the cathode outlet that is divided by the theoretical molar flux $N_{\text{H}_2}^{\text{theo}}$, which can be calculated from Faraday's law. That the actual flux of hydrogen is lower than the theoretical flux and consequently the Faraday efficiency is below 100 % can be caused by different processes: i) electrical short currents, e. g. electric currents through the membrane [74], ii) losses of produced hydrogen due to leakages and especially because of the hydrogen crossover through the membrane [11] and iii) unwanted side reactions, e. g. the recombination of hydrogen with permeated oxygen to water within the cathode [11]. The short currents are low, since the membrane is a good electrical insulator. Consequently, the gas crossover has the greatest influence on the Faraday efficiency of hydrogen, since both the direct loss of hydrogen and the recombination of produced hydrogen with permeated oxygen to water negatively affects the Faraday efficiency [11].

Fig. 2.3 shows the experimental determined Faraday efficiency of hydrogen for a N117 membrane at 2 and 30 bar. The Faraday efficiency increases with current density, since the produced hydrogen flux (Faraday's law) increases with current density. Consequently, the ratio of permeated hydrogen to evolved hydrogen reduces with increasing current density, thus lead to an increase of the Faraday efficiency. At higher pressures the crossover is increased which results in higher losses. Overall due to such unwanted processes several percents of produced hydrogen are getting lost.

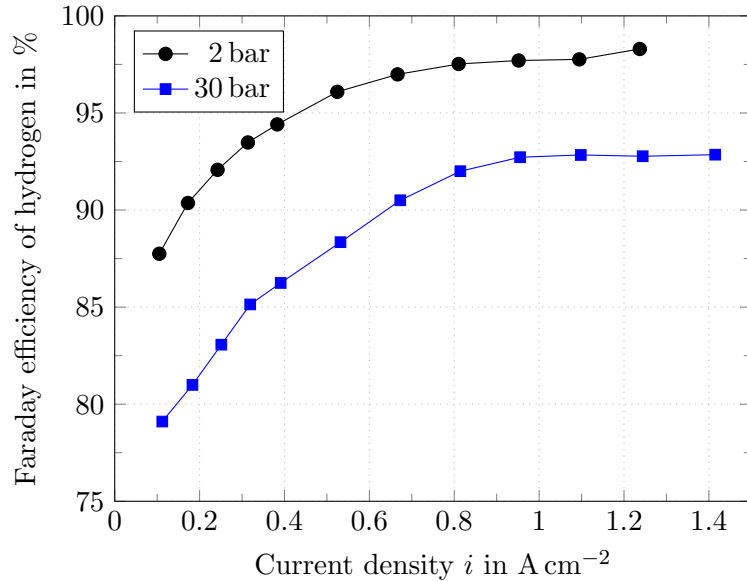


Figure 2.3: Faraday efficiency of hydrogen with a N117 membrane at 2 and 30 bar (data from Grigoriev et al. [11]).

2.2 Fundamentals of Gas Crossover

As previously described, the gas crossover leads to Faraday efficiency losses, additionally as mentioned in the introduction, the gas crossover also causes safety and degradation

issues. Therefore, the gas crossover is an important topic in PEM water electrolysis and also the main focus of this dissertation. Thus, in this section the fundamentals of gas crossover are described to the state of the art as the author started with the doctorate.

2.2.1 Gas Crossover Mechanisms

In PEM water electrolysis cell gas can enter the other half-cell side due to two different transport modes: diffusive and convective. Both transport mechanisms are described in the following.

Diffusion of Dissolved Gas The major part of gas crossover is transported by diffusion through the membrane [66, 75]. Generally, the gases could diffuse through the solid, aqueous or gas phase of the membrane. However, due to the high capillary pressures of the narrow membrane channels, which are filled by water the membrane is presumed to be impermeable for gaseous species [76]. Additionally, it is reported that diffusion through the solid phase of a fully hydrated Nafion membrane is roughly one order of magnitude smaller compared to the diffusion through the liquid phase [66, 77, 78]. Thus, the major part of the gas crossover is caused by diffusion of dissolved gases within the membrane water.

The transport of dissolved gases through the membrane can be described fundamentally by the Maxwell-Stefan approach [79]. However, this transport is typically considered by Fick's first law of diffusion Eq. (2.11) [12, 13, 80, 81]. Fick's law is a simplification of the Maxwell-Stefan approach [82]. In PEM fuel cell simulations at typical conditions the Fickian equation is sufficiently precise compared to the Maxwell-Stefan approach [83]. Consequently, it is assumed that this simplification is a good approximation. In the following, the equations are explicitly given for hydrogen, which also apply to oxygen.

$$N_{\text{H}_2, \text{diff}}^{\text{cross}} = -D_{\text{H}_2}^{\text{eff}} \frac{\Delta c_{\text{H}_2}}{\delta^{\text{mem}}} \quad (2.11)$$

Where Δc_{H_2} represents the difference of the dissolved hydrogen concentration across the membrane with the thickness δ^{mem} and $D_{\text{H}_2}^{\text{eff}}$ denotes the effective diffusion coefficient of dissolved hydrogen in the aqueous phase of the membrane. The estimation of the effective diffusion coefficient in membranes [84] or porous media [85] is typically done by correction of the molecular diffusion coefficient in the aqueous solvent D_{H_2} with the water fraction $\varepsilon_{\text{H}_2\text{O}}$ and the tortuosity τ_{ion} of the ionomer channels (Eq. (2.12)).

$$D_{\text{H}_2}^{\text{eff}} = \frac{\varepsilon_{\text{H}_2\text{O}}}{\tau_{\text{ion}}} D_{\text{H}_2} \quad (2.12)$$

In PEM water electrolysis the concentration difference across the membrane Δc_{H_2} can be estimated equal to the cathodic concentration of dissolved hydrogen $c_{\text{H}_2}^{\text{c}}$ as the anodic hydrogen concentration $c_{\text{H}_2}^{\text{a}}$ is approximately zero [86]:

$$\Delta c_{\text{H}_2} \approx c_{\text{H}_2}^{\text{c}} - \overset{0}{c_{\text{H}_2}^{\text{a}}} \quad (2.13)$$

The dissolved gas concentration can be estimated by Henry's law (Eq. (2.14)), which states that the dissolved gas concentration is directly proportional to its partial pressure in the gas phase. Within the following Eq. (2.14) S_{H_2} denotes the hydrogen solubility in water, whereas the cathodic hydrogen partial pressure is represented by $p_{\text{H}_2}^c$.

$$c_{\text{H}_2}^c = S_{\text{H}_2} p_{\text{H}_2}^c \quad (2.14)$$

Data of the hydrogen solubility in pure water was published by Young et al. [87] for atmospheric pressure conditions. Further data for pressures ranging from 25 to 1000 atm can be found in the publication by Wiebe and Gaddy [88].

The cathodic hydrogen partial pressure can be obtained, when assuming that the cathodic oxygen partial pressure is negligible and that the hydrogen is saturated with water vapor. Then the following Eq. (2.15) applies, where p^c denotes the total cathodic pressure:

$$p_{\text{H}_2}^c = p^c - p_{\text{vap}}^c \quad (2.15)$$

The calculation of the water vapor pressure p_{vap}^c may be performed by application of the Antoine equation with parameters for pure water [89].

Finally, the diffusive hydrogen flux across the membrane can be described with the following Eq. (2.16), if the aforementioned assumptions are applied and inserted into Eq. (2.11).

$$N_{\text{H}_2, \text{diff}}^{\text{cross}} = -D_{\text{H}_2}^{\text{eff}} S_{\text{H}_2} \frac{p_{\text{H}_2}^c}{\delta_{\text{mem}}} \quad (2.16)$$

The product of the effective diffusion and solubility coefficient $D_{\text{H}_2}^{\text{eff}} S_{\text{H}_2}$ is frequently provided in form of the permeability coefficient K_{P, H_2} , which is a classical material property for membranes. For Nafion the permeability coefficients of hydrogen and oxygen at 80 °C are $K_{\text{P}, \text{H}_2} = 5.32 \cdot 10^{-14} \text{ mol m}^{-1} \text{ s}^{-1} \text{ Pa}^{-1}$ and $K_{\text{P}, \text{O}_2} = 2.52 \cdot 10^{-14} \text{ mol m}^{-1} \text{ s}^{-1} \text{ Pa}^{-1}$, respectively [78].

Convective Gas Transport The other possible gas transport mechanism is convection. Generally, convection is the transport of a species with the center of the mass of a fluid element and could be mathematically expressed by Eq. (2.17) [79]. There, v_1 describes the velocity of liquid water moving perpendicular to the membrane, whereas c_{H_2} denotes the concentration of dissolved hydrogen within the moving water.

$$N_{\text{H}_2, \text{conv}}^{\text{cross}} = v_1 c_{\text{H}_2} \quad (2.17)$$

A water flow through the membrane that transport dissolved hydrogen by convection can be caused by the following mechanisms: i) diffusion, ii) hydraulic and iii) electro-osmotic drag [90, 91]. However, the convective gas crossover mechanism is not so well investigated and understood yet. In the following, a rough estimation is described for an evaluation of the impact of the convective gas crossover.

The diffusive transport of dissolved water is an important mechanism for PEM fuel cells in context of humidification of the membrane. However, in PEM water electrolysis cell liquid water feeds are used that keep the membrane well hydrated. Consequently, the

concentration gradients of water are small and this leads to very small diffusive water fluxes.

The hydraulic flow of water through the porous membrane can be commonly described by Darcy's law (Eq. (2.18)) [80,91]. This flow of water is driven by the pressure difference across the membrane.

$$v_{1,\text{hyd}} = -\frac{K_{\text{hyd}}}{\mu_1} \frac{\Delta p}{\delta^{\text{mem}}} \quad (2.18)$$

Here, μ_1 is the dynamic viscosity of water, whereas Δp describes the absolute pressure difference between the cathodic and anodic compartment and K_{hyd} denotes the permeability of the membrane, which can be estimated by the Hagen-Poiseuille or Kozeny-Carman equations [92]. For the state-of-the-art membrane Nafion this transport mechanism is small, because of the small pores, which lead to a very low hydraulic permeability of $4 \cdot 10^{-14} \text{ m}^2$ (at water content $\lambda = 20$) [93]. Consequently, the convective gas transport due to pressure difference driven hydraulic water flux is small. Experiments with Nafion showed no convective crossover [78]. If other membranes with higher permeabilities are used this mechanism would be more important [86], which is especially the case for the classical alkaline water electrolysis with Zirfon separators [94].

The electro-osmotic drag occur due to the electric field and the associated movement of ions, the water molecules can be dragged with them across the membrane. Hence, dissolved gas may also be transported through it [13,90]. Thus, in PEM water electrolysis dissolved oxygen may be dragged along with the transport of protons from the anodic into the cathodic half-cell. In contrast, the electro-osmotic drag could also be capable of reducing hydrogen permeation as it may transport dissolved hydrogen back to the cathode. For Nafion membranes electro-osmotic drag cause the highest liquid water flux across the membrane, especially at higher current densities [91]. Consequently, this could be the most important convective gas crossover mechanism. However, compared to the diffusive flux of dissolved gas the impact is estimated still low and this effect was not experimentally investigated/observed yet.

2.2.2 Gas Crossover Dependencies

As previously described the main gas crossover mechanism for PEM water electrolyzers is the diffusive transport of dissolved gases across the membrane [66]. This transport has certain dependencies, which are discussed in the following. Therefore, the previously derived Eq. (2.16) for the diffusive crossover of dissolved hydrogen is shown below with an indication of the important dependencies:

$$N_{\text{H}_2,\text{diff}}^{\text{cross}} = D_{\text{H}_2}^{\text{eff}}(T, \lambda) S_{\text{H}_2}(T) \frac{\Delta p_{\text{H}_2}^c(T, p^c)}{\delta^{\text{mem}}(T, \lambda)} \quad (2.19)$$

Partial Pressure The partial pressure gradient across the membrane is the driving force for the diffusive crossover transport. By increasing the operating pressure of the cathode the partial hydrogen pressure increase also. Consequently, the partial pressure gradient

increases and hence the crossover flux, which is directly proportional to the hydrogen partial pressure [95,96]. This can be seen in Fig. 2.4 up to cathode pressures of 225 bar.

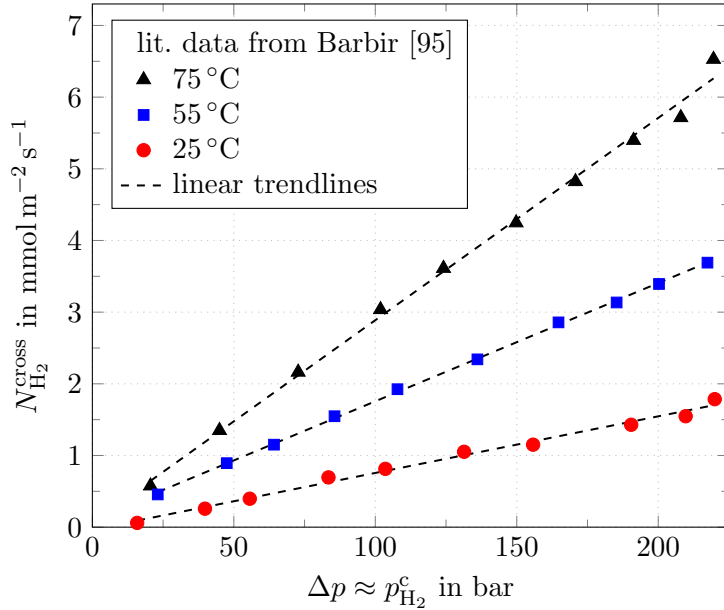


Figure 2.4: Hydrogen crossover flux as a function of pressure for three different temperatures with a N117 membrane (data from Barbir [95]).

Temperature The gas crossover increase with temperature [78,95–97]. Both, diffusion and solubility coefficients have temperature dependencies. However, the temperature dependency of the diffusion coefficient is stronger [66]. Consequently, the temperature dependency is mainly characterized by the temperature dependency of the diffusion coefficient, which can be described by the Arrhenius approach [66]. Other indirect effects has the temperature on the partial gas pressure due to the temperature depending saturated vapor pressure and due to a stronger membrane swelling at higher temperatures [67].

The temperature effect on the hydrogen crossover flux can also be seen in Fig. 2.4. This effect becomes more important at higher pressures, since the product of the temperature dependent diffusion coefficient and the partial pressure gradient increase strongly when both parameters are increased.

Membrane Thickness The partial pressure gradient across the membrane also increases when the membrane thickness is reduced. The crossover flux is inversely proportional to the membrane thickness [10,13,96]. This effect can be seen in Fig. 2.5. The membrane thickness becomes more important at higher pressures, since the partial pressure gradient across the membrane strongly increases at higher pressure in combination with thin membranes. Additionally, Fig. 2.5 shows the directly proportional correlation to the hydrogen partial pressure (cf. Fig. 2.4).

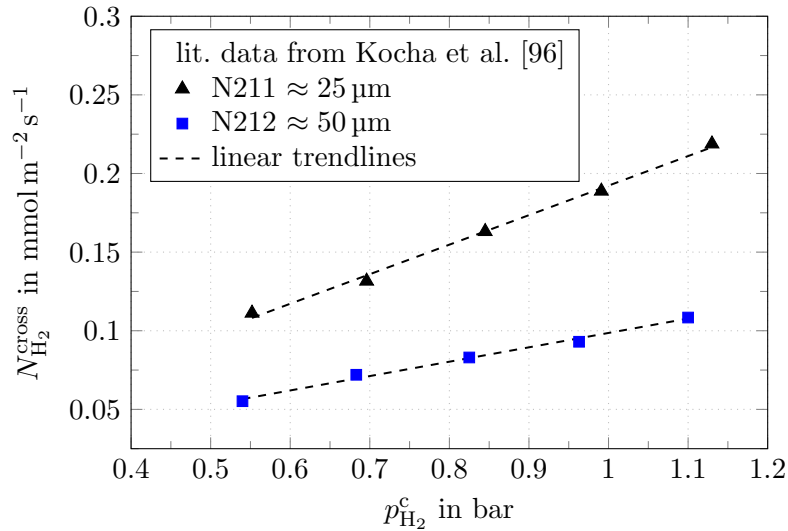


Figure 2.5: Hydrogen crossover flux as a function of the hydrogen partial pressure for two different membrane thicknesses (N211 and N212) at a temperature of 80 °C (data from Kocha et al. [96]).

Water Content The crossover is also depending on the membrane water content λ . The higher the water content, the higher the crossover due to increased effective diffusion coefficients [75, 77, 98, 99]. For PEM fuel cells this can be controlled by the relative humidity of the feed gases. Additionally, the membrane swelling can effect the crossover flux (cf. Eq. (2.19)).

However, as previously discussed the membrane is well humidified for PEM water electrolysis applications due to the liquid water feed. That means, in PEM water electrolysis the permeability coefficients are high due to the fully water saturated membranes [66].

2.3 Critical Discussions of recent Findings

Additionally to the previously discussed pure diffusive crossover effects, the crossover was indirectly observed during water electrolysis operation in form of the hydrogen in oxygen content of the dry anode product gas. In the following these hydrogen in oxygen content measurements and the resulting hydrogen crossover are critically discussed.

2.3.1 Hydrogen in Oxygen Content

The in-situ measurement of the hydrogen in oxygen content of the anode product gas during electrolysis operation has already been used, particularly to evaluate safety issues and efficiency losses, e. g. [11, 14, 100, 101]. In Fig. 2.6 literature results of the measured H_2 in O_2 content versus current densities are shown. These experimental data were measured with two different setups and at different operating conditions. The data show a hyperbolic trend, which can be explained by the increasing oxygen evolution $N_{O_2}^{evo}$ with

increasing current density (Faraday's law) that dilutes the permeated hydrogen content. Consequently, the hydrogen content within the anode is high at small current densities and decreases for higher current densities.

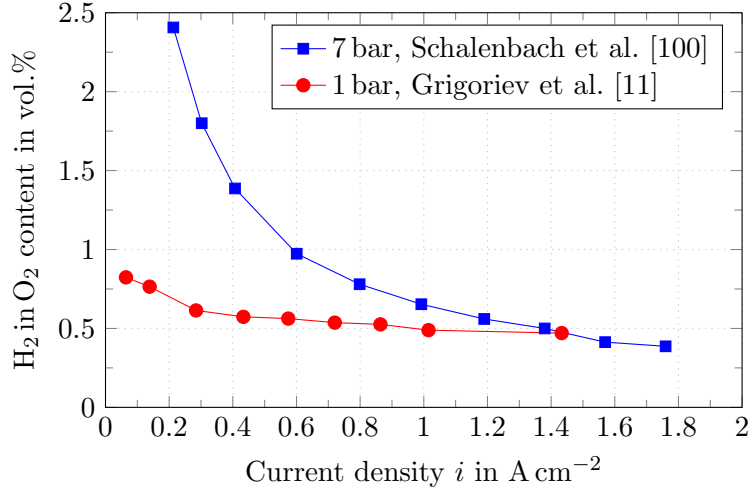


Figure 2.6: Comparison of literature data of the H₂ in O₂ content versus current density: Schalenbach et al. [100]: N117, $T = 80^\circ\text{C}$, $p^c = 7$ bar and Grigoriev et al. [11]: N117, $T = 85^\circ\text{C}$, $p^c = 1$ bar).

The experimental data of Schalenbach et al. [100] were measured at a higher cathode pressure of 7 bar in comparison to the results of Grigoriev et al. [11], which were measured at atmospheric pressure conditions. Consequently, the hydrogen in oxygen content from Schalenbach et al. [100] are higher due to increased crossover fluxes at higher cathode pressures. However, at a current density of 1.4 A cm^{-2} the experimental data intersect. This behavior can not be explained with the state-of-the-art information. Additionally, it is difficult to interpret the hyperbolic trend of the hydrogen volume fraction data regarding the hydrogen crossover flux. Therefore, in the next subsection it is shown how the hydrogen crossover flux can be calculated by the measured H₂ in O₂ content.

2.3.2 Calculation of the Hydrogen Crossover

Schalenbach et al. [100] showed that IrO₂ is inactive for the electrochemical oxidation of hydrogen, when operating at electrolysis conditions (cell voltage higher as the reversible cell voltage). It is also assumed that the permeated hydrogen does not react chemically at the inactive iridium oxide. Consequently, all of the permeating hydrogen can be measured within the anodic product gas by the gas analyzer.

For ideal gases and by neglecting the oxygen crossover that is found to be at least two times lower [75] the measured hydrogen in oxygen volume fraction $y_{\text{H}_2\text{inO}_2}^{\text{dry}}$ of the dry anode product gas can be calculated by as follows:

$$y_{\text{H}_2\text{inO}_2}^{\text{dry}} = \frac{N_{\text{H}_2}^{\text{cross}}}{N_{\text{H}_2}^{\text{cross}} + N_{\text{O}_2}^{\text{evo}}} \quad (2.20)$$

where $N_{\text{H}_2}^{\text{cross}}$ is the crossover flux of hydrogen and $N_{\text{O}_2}^{\text{evo}}$ the molar flux related to the oxygen evolution, which can be calculated with Faraday's laws of electrolysis Eq. (2.21).

$$N_{\text{O}_2}^{\text{evo}} = \frac{i}{4F} \quad (2.21)$$

By solving Eq. (2.20) for the hydrogen crossover $N_{\text{H}_2}^{\text{cross}}$ and inserting Eq. (2.21) the hydrogen crossover flux can be calculated via the measured hydrogen in oxygen content $y_{\text{H}_2\text{inO}_2}^{\text{dry}}$ and the applied current density i .

$$N_{\text{H}_2}^{\text{cross}} = \frac{i}{4F} \frac{y_{\text{H}_2\text{inO}_2}^{\text{dry}}}{(1 - y_{\text{H}_2\text{inO}_2}^{\text{dry}})} \quad (2.22)$$

Fig. 2.7 shows the hydrogen crossover fluxes that is calculated by Eq. (2.22) for the previously shown literature hydrogen in oxygen content measurements of Fig. 2.6. It can be seen that the hydrogen crossover linearly increases with current density. First, the crossover flux of the 7 bar measurement of Schalenbach et al. [100] is higher in comparison to the 1 bar data of Grigoriev et al. [11]. However, the slope of the crossover increase according to the data from Grigoriev et al. [11] is significantly higher. These differences of the slopes might be caused by the different operating conditions, applied materials, cell setups or sensors.

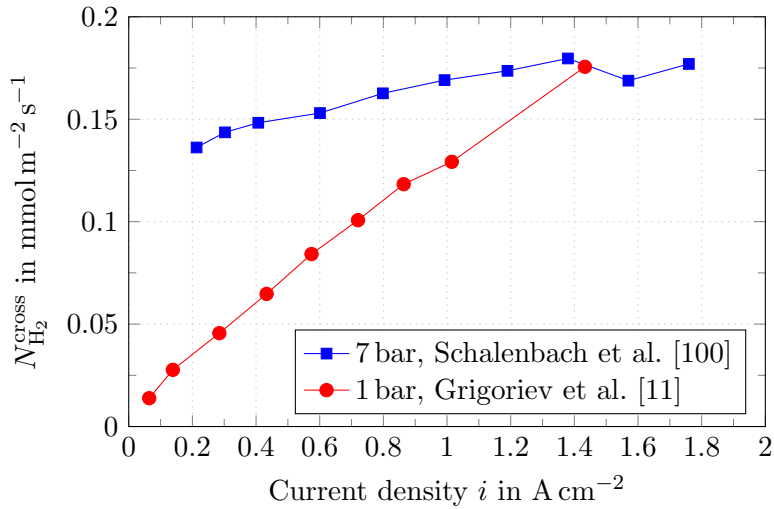


Figure 2.7: Hydrogen crossover versus current density that is calculated by Eq. (2.22) and the literature data of Schalenbach et al. [100] and Grigoriev et al. [11], which are shown in Fig. 2.6.

2.3.3 Initial Considerations: a Comparison of different possible Reasons for the Current Density Dependence of Hydrogen Crossover

The previously presented data show a strong increase of hydrogen crossover with current density. This phenomenon may be surprising, when considering the electro-osmotic drag and the resulting water flux induced with higher currents that could result in a convective transport of dissolved hydrogen back to the cathode, as discussed in the modelling study of Grigoriev et al. [90]. Consequently, an increase in current density should lead to a decrease of the hydrogen crossover. However, the opposite is the case and in the following, possible reasons for the hydrogen crossover increase with current density for PEM water electrolysis systems are discussed.

Local Pressure Enhancement The increasing crossover flux with increasing current density is explained in literature by the increase of local pressure in the catalyst layer due to gas transport [13, 75]. Schalenbach et al. [100] used an empirical pressure enhancement factor to consider this pressure increase in their crossover model. This factor was fitted with experimental results to 8 bar per A cm^{-2} . This enhancement factor was also used by Ito et al. [14] and was determined to 17–33 bar per A cm^{-2} depending on the operating conditions. Sakai et al. [75] stated that for a current density increase of 1 A cm^{-2} the local pressure increases by about 50 bar.

Consequently, these high pressure enhancements would lead to very large pressure differences across the cathode PTLs. Since cathode PTLs are typically quite thin, 100 – 400 μm , this would correspond to pressure gradients of several 100 bar cm^{-1} , which seems improbable for porous media with porosities of approximately 0.3 – 0.8.

In the following the pressure enhancement over the PTL is roughly estimated by use of a simple model in order to compare it with the statements of Sakai et al. [75] and Schalenbach et al. [13]. The pressure enhancement across the catalyst layer is neglected for this investigation, since it is very thin (approx. 10 μm [52]) compared to the PTL. The core assumption of the following estimation is that Darcy’s law (Eq. (2.23)) is valid to describe the local gas pressure enhancement over the liquid water filled PTL [102, 103]:

$$\Delta p = \frac{\mu_{\text{H}_2}}{K_{\text{hyd}}^{\text{eff}}} \delta^{\text{PTL}} v_{\text{H}_2} \quad (2.23)$$

Herein, Δp is the pressure enhancement, μ_{H_2} the dynamic viscosity of hydrogen, δ^{PTL} the thickness of the PTL, v_{H_2} the hydrogen velocity and $K_{\text{hyd}}^{\text{eff}}$ is the effective hydraulic permeability of the PTL, which is corrected by a common approach (Wyllie’s cubic power law Eq. (2.24)) to consider the influences of the liquid water saturation s [103, 104].

$$K_{\text{hyd}}^{\text{eff}} = K_{\text{hyd}} (1 - s)^3 \quad (2.24)$$

The velocity v_{H_2} of hydrogen can be estimated from the produced hydrogen flux (Faraday’s law) and the molar volume of hydrogen. For this simplistic approximation

hydrogen is assumed to behave as an ideal gas.

$$v_{\text{H}_2} = \frac{i}{2F} \frac{RT}{\bar{p}} \quad (2.25)$$

Within Eq. (2.25) \bar{p} is the mean pressure of the PTL. Hereby, the pressure profile across the PTL is assumed to be linear, so that the mean pressure \bar{p} can be estimated by Eq. (2.26).

$$\bar{p} = p^c + 1/2\Delta p \quad (2.26)$$

The theoretical pressure enhancement was calculated for a temperature of 60 °C and cathode pressures between 1 and 31 bar. The remaining parameters were chosen based on literature data such that a conservative estimation is guaranteed. The permeability data for carbon PTLs are reported in a vast range from $4 \cdot 10^{-14}$ to $7 \cdot 10^{-11} \text{m}^2$ [38, 105, 106]. Since the pressure enhancement increase with decreasing permeabilities the smallest value of $K_{\text{hyd}}^{\text{dry}} = 4 \cdot 10^{-14} \text{m}^2$ is chosen. The water saturation s is measured in a range from 0.1 to 0.8 [107–109], for a comparable system a value of 0.9 was reported in [102]. Since a high saturation hinder the gas transport and thus lead to an increasing pressure enhancement, the high value of 0.9 is selected for this conservative estimation. Here, the PTL is selected to be very thick, roughly three times thicker as common PTLs, $\delta^{\text{PTL}} = 1000 \mu\text{m}$, which lead to an even higher pressure enhancement.

Table 2.1: Parameters for the estimation of the local pressure enhancement at 60 °C.

Parameter	Value	Unit	Source
μ_{H_2}	$9.6 \cdot 10^{-6}$	Pa s	[110]
δ^{PTL}	1000	μm	chosen
K_{hyd}	$4 \cdot 10^{-14}$	m^2	[105]
s	0.9		[102]
p^c	1–31	bar	chosen

Fig. 2.8a) shows the local pressure enhancement Δp across such a PTL as a function of current density for different cathode pressures p^c . It can be seen that the pressure enhancement increases with increasing current density. However, the pressure enhancement is much lower than the published pressure enhancement of 8 [100]–50 [75] bar per A cm^{-2} , although the parameters were selected conservatively to suit as a maximum approximation.

Furthermore, Fig. 2.8a) shows that the pressure enhancement decreases with increasing cathode pressure. This is caused by the velocity decrease (s. Eq. (2.23)) with increasing pressure. The gas transport is improved at higher pressure conditions. Consequently, this would cause lower crossover increases at higher cathode pressures.

Fig. 2.8b) shows the comparison of the experimental crossover results at a cathode pressure of 1 bar and the corresponding crossover fluxes due to the pressure enhancement model, which are calculated by Eqs. (2.16) and (2.23). It can be seen that even the

overestimated pressure enhancement of the model can not explain the experimental data of Grigoriev et al. [11] in a quantitative manner.

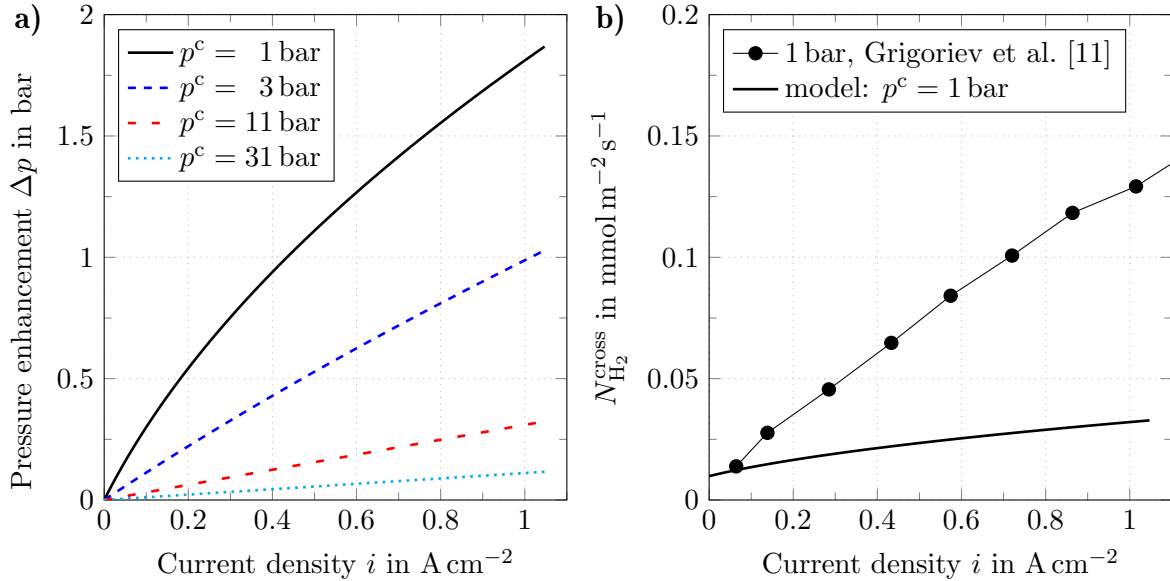


Figure 2.8: Simulation results of the pressure enhancement model for different cathode pressures: a) pressure enhancement over the PTL and b) comparison of the according crossover rate of the pressure enhancement model with calculated crossover fluxes from literature data Grigoriev et al. [11].

Nevertheless, it is possible that the local pressure enhancement across the porous layers can cause small increases in crossover. However, this effect is probably too small to explain the strong crossover increases with current density.

Local Temperature Increase A further explanation might be an increase of temperature with current density due to the increasing heat input. The temperature within the MEA should be certainly higher according to the observations from experiments with PEM fuel cells [111,112]. Consequently, this leads to increases in the diffusion coefficient and thus to an increase in crossover.

However, to explain the previously shown experimental crossover increases at low cathode pressures the temperature has to raise to more than 100 K per A cm^{-2} . Such temperature increases are impossible and consequently the temperature increase with current density is too low to explain the strong crossover increase with current density. Even so, the temperature within PEM water electrolysis cells increases with current density and as a consequence the hydrogen crossover as well, although in a smaller quantity.

Structural Changes It was already supposed that the applied current could lead to structural changes of the membrane [86]. For example widening of the water channels within the membrane or changing of cathodic membrane interface from a hydrophobic

membrane/vapor towards a hydrophilic membrane/liquid interface [113–115]. Consequently, these structural changes could influence the transport properties and may influence the gas crossover. However, there are no clear evidences that this leads to such high crossover fluxes. Especially, while other parameters, such as the membrane resistance (high frequency resistance) are almost constant for different current densities [23]. Consequently, it is also improbable that the structural changes in the ionomer are high enough to explain the observed crossover increases with current density.

2.4 Research Questions

Now that the state-of-the-art information according to gas crossover are discussed, especially with the previously considerations to the crossover increase with current density, the research questions (RQs) for the present work can be derived. Overall there are 5 RQs, which will be separately discussed in the following.

Research Question 1: *“What are the effects of different operating conditions on the increase of hydrogen crossover with current density?”*

Although literature measurements were carried out under different operating conditions (s. Fig. 2.7), they are not comparable due to the different cell setups. It is important to investigate the effect of different operating conditions (temperature and pressure) on the current density effect. This analysis might help to reveal temperature and pressure dependencies of the crossover increase that could lead to understand the underlying mechanisms.

Research Question 2: *“Which alternative theory can be formulated to explain the current density dependence?”*

The previous considerations to the crossover increase with current density shows that temperature raises, structural changes and even local pressure enhancements are rather unlikely to explain the experimental findings. Due to the measurements of RQ 1 it may be possible to find another explanation approach.

Research Question 3: *“Is the oxygen crossover also influenced by current density?”*

It is conceivable that the same effect also occurs for oxygen crossover. However, on the cathode side the state-of-the-art catalyst lead to a recombination of permeated oxygen with evolved hydrogen to water. Consequently, the oxygen in hydrogen content within the cathode product gas can not be used to calculate the whole oxygen crossover. That means it will be more difficult to investigate the effect of current density on oxygen crossover.

Research Question 4: *“What is the influence of the electrode structure on the current density effect on gas crossover”*

In RQ 1 the effect of the operating conditions on crossover is investigated. However, this effect can also be influenced by the applied materials or structures. Therefore, within the scope of RQ 4 the influence of the electrode structure on the crossover increase with current density is investigated.

Research Question 5: *“How can the current density influence on gas crossover be described adequately by a physically meaningful model? How can the developed model help to analyze the observed effects in more detail?”*

Due to the experimental results of the previous RQs 1, 3 and 4 in combination with the alternative theory of RQ 2, it might be possible to formulate a physically meaningful model to investigate the experimental findings in more detail. The model should be able to explain the experimental results. For the model formulation it is claimed to explain the experimental results exclusively with literature parameters without parameter fitting.

3 Experimental Setup

Within this chapter the experimental setup is described. First, the test bench is illustrated, at which the experiments were carried out. Then the sensors and instrumentation with the applied procedures and methods are presented. Subsequently, the used PEM water electrolysis cells and applied materials are described.

3.1 Test Bench

Greenlight Test Station All electrochemical experiments were carried out with a Greenlight type E100 test station. A flow sheet of the test station is shown in Fig. 3.1. This test bench enables deionized (DI) water feeds from 1 to 500 g min⁻¹ at the anode as well as on the cathode side. Additionally, both cycles can be flushed also by hydrogen, oxygen or nitrogen. The anode and cathode cycles can be controlled at differential and balanced pressure conditions up to 50 bar. The temperature can be controlled between 30 and 80 °C. On each side the gas-water mixture is separated by two gas separators and an intermediate cooling step of the gas after the outlet of the first separator. The water levels of the gas-water separators are automatically controlled. For safety reasons the anode and cathode product gases are analyzed by hydrogen in oxygen and oxygen in hydrogen sensors, respectively. These sensors are described later within the sensors and instrumentation section.

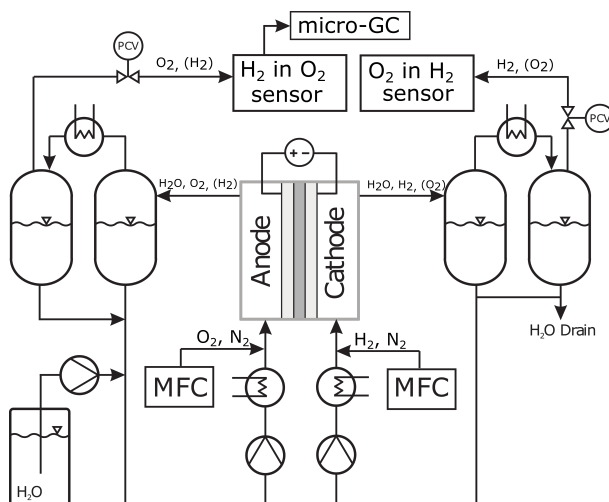


Figure 3.1: Flow sheet of the test bench.

The electrolysis cells can be operated galvanostatically from 0 to 220 A or potentiostatically from 0 to 6 V by an Ametek Sorensen XG 6-220 power supply, which is integrated within the test station. The cell voltage and current as well as temperatures, pressures,

DI water quality (resistance measurements), gas and water flow rates can be logged by the test station.

3.2 Sensors, Instrumentation and Methods

Within this section the measurements devices are described as well as the measurement procedures, which were applied by the author to determine the gas crossover and cell performance.

3.2.1 Measurement Devices

For the determination of the hydrogen and oxygen crossover the hydrogen content within the anodic oxygen product gas and the oxygen content within the cathodic hydrogen product gas was measured. Therefore different gas sensors were used, which are described in the following.

Hydrogen Sensor The measurement of the hydrogen volume fraction of the dried anodic product gas is directly included within the Greenlight test station due to safety reasons, since the lower explosion limit (LEL) of a hydrogen/oxygen atmosphere is quite low at about 4 vol.% H₂ in O₂ [17]. The H₂ in O₂ content was measured by a K1550 gas sensor (Hitech Instruments) based on a heat conductivity measurement. This sensor has a measurement range of 0–5 vol.% H₂ in O₂ with a measurement error of $\Delta y_{\text{H}_2\text{inO}_2}^{\text{dry}} = \pm 0.1 \text{ vol.}\%$.

Oxygen Sensor Oxygen in hydrogen on the cathode side was measured by an electrochemical cell analyser (G1010 cell type H, Hitech Instruments). The measurement range of the sensor is 10 ppm to 10 % O₂ in H₂. Unfortunately, no reliable information are available about the accuracy, since the intention of its installation is to control the compliance of the safety limits and therefore no precise calibration was done. However, the sensor showed reproducible results. It is therefore considered as suitable for a qualitative measurement.

Gas Chromatograph A micro-GC (Agilent 490) was additionally connected to the Greenlight test station for more accurate measurements. This micro-GC is equipped with a 10 m long 5 Å molecular sieve column and a thermal conductivity detector for permanent gas separation and detection. Test gas mixtures with hydrogen concentrations of 0.1, 1 and 2.5 vol.% in oxygen and 10 vol.% hydrogen in nitrogen (accuracy of reading $\pm 2\%$, Linde) were used for calibration of the micro-GC.

Electrochemical Test System The electrochemical performance was determined by polarization curves, electrochemical impedance spectroscopy (EIS) and high frequency resistance (R_{HFR}), which were measured by a ModuLab XM ECS (Solartron analytical).

The ModuLab was equipped with a XM FRA card, a XM PSTAT card and an external 100 A booster.

3.2.2 Measurement Procedures

The following paragraphs describe the measurement procedures of the gas crossover and electrochemical cell performance.

Gas Crossover Measurement Before the gas crossover measurements were started, the test cells and system were purged by nitrogen. Subsequently, the operating conditions (cell temperature, pressure, water flow and water temperature) were adjusted. After reaching the set points, the cells were operated galvanostatically, while the hydrogen in oxygen content was measured. Each galvanostatic step was held until stationary states of the hydrogen in oxygen and oxygen in hydrogen contents have been formed. The respective values of the steady states were taken for the determination of the hydrogen crossover (s. sec. 2.3.2). After each stationary state the current density was increased for the next measurement point.

Oxygen Crossover In comparison to the calculation of the hydrogen crossover (s. sec. 2.3.2) it is more advanced to determine the oxygen crossover, since on the cathode side the permeated oxygen recombines with evolved hydrogen to water at the state-of-the-art catalyst, platinum. The O₂ in H₂ volume fraction $y_{O_2inH_2}^{dry}$ of the cathode product gas could be calculated as follows:

$$y_{O_2inH_2}^{dry} = \frac{N_{O_2}^{cross} - N_{O_2}^{recomb}}{N_{H_2}^{evo} - N_{H_2}^{cross} + N_{O_2}^{cross} - N_{O_2}^{recomb} - N_{H_2}^{recomb}} \quad (3.1)$$

where the superscript recomb stands for the unknown fluxes of hydrogen and oxygen due to the recombination reaction of hydrogen and oxygen to water within the cathode catalyst layer. Consequently, without more information/assumptions it is impossible to calculate the oxygen crossover flux $N_{O_2}^{cross}$.

At least, it is possible to calculate the oxygen flux within the cathode outlet. For this purpose, the oxygen in hydrogen volume fraction $y_{O_2inH_2}^{dry}$ of the cathodic product gas is reduced to Eq. (3.2).

$$y_{O_2inH_2}^{dry} = \frac{N_{O_2}^{c,out}}{N_{tot}^{c,out}} \quad (3.2)$$

Herein, $N_{O_2}^{c,out}$ is the oxygen flux within the dried cathode product gas and $N_{tot}^{c,out}$ the total molar flux of the cathode, which can be assumed to be approximately equal to the amount of evolving hydrogen within the cathode Eq. (3.3). Therefore, hydrogen and oxygen crossover and the recombination fluxes are assumed to be negligible small compared to the amount of evolving hydrogen, i. e. at atmospheric pressure conditions

and 0.1 A cm^{-2} the error is already below 1 %.

$$N_{\text{tot}}^{\text{c,out}} \approx N_{\text{H}_2}^{\text{evo}} = \frac{i}{2F} \quad (3.3)$$

By solving Eq. (3.2) for the oxygen flux of the cathode outlet $N_{\text{O}_2}^{\text{c,out}}$ and inserting Eq. (3.3), the oxygen flux of the cathode outlet can be approximately calculated by the measured oxygen volume content $y_{\text{O}_2\text{inH}_2}^{\text{dry}}$ and the applied current density i :

$$N_{\text{O}_2}^{\text{c,out}} \approx y_{\text{O}_2\text{inH}_2}^{\text{dry}} \frac{i}{2F} \quad (3.4)$$

It has to be highlighted, that the determined oxygen flux within the cathode outlet $N_{\text{O}_2}^{\text{c,out}}$ is not equal to the complete oxygen crossover flux. It can be interpreted as a minimal oxygen permeation rate, since the applied cathodic catalyst materials are still active for the recombination of permeated oxygen. Consequently, the real oxygen crossover is higher than the determined cathodic oxygen flow $N_{\text{O}_2}^{\text{c,out}}$. Consequently, the oxygen crossover measurement via the oxygen in hydrogen content should only be qualitatively interpreted.

Electrochemical Cell Performance Polarization curves were measured galvanostatically with logarithmic steps from 0.01 to 1 A cm^{-2} and a constant step size of 0.1 A cm^{-2} between 1 and 2 A cm^{-2} . Each step was held for 10 s with a sample rate of 5 Hz . The last 5 measured values of each step were averaged for the polarization curves.

Between each galvanostatic step the R_{HFR} was measured. Therefore, short galvanostatic EIS measurements were implemented with sinusoidal current density signals with frequencies from 50 to 0.1 kHz and a root mean square of 10% of the applied DC current. The area-normalized R_{HFR} is determined as the impedance values at a phase angle of 0° multiplied by the active area. The R_{HFR} is used to calculate the iR -free cell voltage, which is mainly used for the Tafel analysis to determine kinetic parameters and the remaining losses.

Also full galvanostatic EIS measurements were conducted at several DC current densities from 0.05 to 2 A cm^{-2} . The frequencies of the sinusoidal signal were changed from 100 kHz to 0.1 Hz also with a root mean square of 10% of the DC current.

3.3 Test Cells

In context of this dissertation two different test cells were used, which are described in the following.

Sylatech Cell A commercially available high pressure electrolysis cell (Sylatech Analysetechnik GmbH, type ZE 200) was used for the high pressure experiments. This cell is called "sylatech cell" in the following. It has a circular design with an active area of 62 cm^2 without flow field structures. The flow field on the anode side is substituted by

a expanded titanium mesh. Between the mesh and the CCM a PTL is incorporated, which consists of sintered titanium fibres. In the cathodic half-cell a carbon paper is implemented. The sealing of this high pressure water electrolysis cell is realized by an O-ring only on the cathode side. The screws were tightened with a torque of 30 N m to provide the required gas tightness, which results in a clamping pressure on the active area of 2 MPa (measured by means of a pressure measurement film, Fujifilm prescale type LLW).

Baltic Cell A quickCONNECTfixture qCf FC25/100 (LC) frame (baltic FuelCells GmbH) was integrated within the worktop of the test station. The liquid cooling system of the frame was supplied by a circulation thermostat (Huber ministat 230) for isothermal operating conditions. The quickCONNECTfixture frame allows a separated sealing and clamping of the active are. The clamping pressure on the active area can be adjusted by the applied gas pressure on the piston.

For the quickCONNECTfixture qCf FC25/100 (LC) frame a quadratic electrolyzer cell ($A = 25 \text{ cm}^2$) was used, which was also fabricated by the baltic FuelCells GmbH. This cell is called "baltic cell" in the following. It has, on the anode side as well as on the cathode side, parallel flow fields with 1.87 mm wide lands and 2.5 mm deep and 2 mm wide channels. Within both half-cells O-rings are used for the sealing system. However, the baltic cell can only be operated at ambient pressure. In this work a pressure of 4.5 bar was applied on the piston, which results in a clamping pressure on the active area of 1.4 MPa.

3.4 Materials

In the context of this dissertation different materials were used, because of the different test cells and experimental studies. These materials are summarized in Tab. 3.1. In the brackets the respective chapters/sections are given, in which the material were used. Mainly commercial materials were used, except for the ionomer variation of chapter 5. Therefore, the preparation and physical characterization is described in section 5.1. The applied materials are described in more detail within the next paragraphs.

Table 3.1: List of the applied materials for both test cells. Within brackets the respective chapters/section are stated.

Anode PTLs	Cathode PTLs	Commercial CCMs	Labmade CCMs
Materials for the sylatech test cell:			
<ul style="list-style-type: none"> • Supplied Ti-fibres (sec. 4.1) 	<ul style="list-style-type: none"> • Supplied carbon paper (sec. 4.1) 	<ul style="list-style-type: none"> • Fumea[®] EF-40 (sec. 4.1) 	
Materials for the baltic test cell:			
<ul style="list-style-type: none"> • Bekaert Ti-fibres, 2GDL40-1.0 (sec. 4.3 and ch. 5) 	<ul style="list-style-type: none"> • Toray, TGP-H-090 (sec. 4.3) • Toray, TGP-H-120 (ch. 5) 	<ul style="list-style-type: none"> • HIAT N117 (sec. 4.3) • HIAT N117 Pt-free cathode catalyst (sec. 4.3) • HIAT N115 only w. anode catalyst layers (ch. 5) 	<ul style="list-style-type: none"> • Cathode ionomer variation (s. sec. 5.1)

3.4.1 Porous Transport Layers

For the circular sylatech cell sintered titanium PTLs and carbon PTLs are used, which were provided by the manufacturer. For the baltic cell also sintered titanium fibers PTLs with fibres diameters of 20 μm , a porosity of 0.56 and a thickness of 1 mm (2GDL40-1,00, Bekaert) were used on the anode side. On the cathode side carbon papers with a porosity of 0.78 and thicknesses of 270 and 370 μm (TGP-H-090 and TGP-H-120, Toray Industries) were used.

3.4.2 Catalyst Coated Membranes

To investigate the experimental based RQs commercial and lab-made CCMs were used. The commercial CCMs are listed in Tab. 3.1 and are described below. Additionally, commercial half-side coated CCMs were used to manufacture special lab-made CCMs for, which is described in more detail within section 5.1.

CCMs for the Sylatech Cell Within the sylatech cell a Fumea[®] EF-40 CCM (FuMa-Tech GmbH) with an active area of 62 cm^2 was used. Before usage the CCM was activated as it was recommended by the manufacturer. The membrane of the applied CCM is a reinforced PFSA membrane with a thickness of δ^{mem} of 230 – 250 μm , a water uptake of approximately 30 wt.% and an equivalent weight of 910 g mol^{-1} . The catalyst material on the anode and cathode are Ir- and Pt-based, respectively. This CCM was the supplied standard material of the sylatech cell. It is used for the detailed investigation of the current density effect on hydrogen crossover (RQ 1).

CCMs for the Baltic Cell All CCMs for the baltic cell have an active area of 5 cm x 5 cm ($A = 25 \text{ cm}^2$). For the investigation of the oxygen crossover (RQ 3) two different CCMs were used. Both CCMs were manufactured by HIAT gGmbH. These CCMs differ only in the cathode catalyst material. For this study a common CCM, which contains the state of the art material: Pt on advanced carbon with a loading of 1 mg cm^{-2} and a catalyst composite that is free of platinum were used. The detailed composition of the catalyst was not provided by the manufacturer. The remaining components of both CCMs are identical: Nafion[®] N117 membrane and Ir black as anode catalyst material with a loading of 2 mg cm^{-2} .

The Pt-free catalyst requires an activation phase of approximately 1 – 2 days. In this period the current density was progressively increased – till a current density of 2 A cm^{-2} could be reached at moderate cell voltages.

Furthermore half-side coated anode CCMs were manufactured by HIAT gGmbH. Standard anode catalyst layers of $2 \text{ mg}_{\text{Ir}} \text{ cm}^{-2}$ were coated by doctor blade on Nafion[®] N115. These half-side coated CCMs were modified by Forschungszentrum Jülich to investigate the effect of mass transfer losses on crossover and cell voltage, which is described in section 5.1.

4 Effect of Current Density on Gas Crossover

As described within chapter 2 the gas crossover is mainly a function of pressure, temperature and membrane properties, such as the permeability coefficient or membrane thickness. Generally, to characterize these effects and mainly to determine the permeability coefficients of different PEMs the gas crossover is determined by means of measurement methods without electrolysis operation or only at very small current densities [66,99,116]. However, as previously shown some research groups already measured the hydrogen in oxygen volume fraction within the anode during water electrolysis operation [11, 14, 100, 101].

These hydrogen in oxygen content measurements revealed that the hydrogen crossover is strongly influenced during water electrolysis operation, which was also observed by Sakai et al. [75]. However, this effect was not further characterized in detail. Sakai et al. [75] suggested that an increase in current density leads to an enhancement of the local pressure within the catalyst layer due to the gas evolution and that this result in local overpressures, which cause increases in gas crossover [75]. The same explanation was proposed by Schalenbach et al. [100]. They introduced in their electrolysis model an empirical pressure enhancement factor, which was parameterized with experimental data. Both research groups stated that the local pressure increases with current density about several bar per $A\text{ cm}^{-2}$.

The critical consideration to this approach revealed that the local pressure enhancement is rather unlikely to explain the crossover increase with current density (s. sec. 2.3). This chapter examines the following research questions:

Research Question 1: *“What are the effects of different operating conditions on the increase of hydrogen crossover with current density?”*

Research Question 2: *“Which alternative theory can be formulated to explain the current density dependence?”*

Research Question 3: *“Is the oxygen crossover also influenced by current density?”*

Therefore, within this chapter the effect of current density on hydrogen as well as oxygen crossover is investigated. For this purpose, the anodic hydrogen and the cathodic oxygen content were measured to determine the hydrogen and oxygen crossover. First in section 4.1, the experimental results are discussed and compared to available literature data. To investigate the effect of current density on the hydrogen crossover in more detail (RQ 1) the anodic hydrogen content was measured during PEM water electrolysis

operation at different temperatures between 30 and 80 °C and cathode pressures in the range of 1 to 31 bar.

Subsequently, an alternative explanation approach is formulated to describe the experimental findings (RQ 2). After the sections concerning the hydrogen crossover, in section 4.3 measurements of the oxygen in hydrogen content of the cathode product gas are shown to characterize the effect of current density on oxygen crossover (RQ 3). Finally, this chapter ends with concluding remarks.

4.1 Current Density Effect on Hydrogen Crossover

The following sections are based on the publication: P. Trinke, B. Bensmann and R. Hanke-Rauschenbach: Current density impact on hydrogen permeation during PEM water electrolysis (2017). *Int. J. Hydrogen Energ.* **42**, 14355-14366, doi.org/10.1016/j.ijhydene.2017.03.231. Focus of this section is to investigate the influence of different operating conditions on the current density effect on hydrogen crossover (RQ 1). The measurements were performed with the sylatech cell and the provided standard cell materials (CCM: fumea EF-40), which are described in chapter 3.

4.1.1 Comparison to Literature Results

In Fig. 4.1a) the measured hydrogen volume fractions of this work are plotted for different current densities at a temperature of $T = 80\text{ °C}$ and a pressure of $p = 1\text{ bar}$. The data show the characteristic trend of a hyperbola, which can be explained by the increasing oxygen evolution $N_{\text{O}_2}^{\text{evo}}$ with increasing current (Eq. (2.21)) that reduces the hydrogen in oxygen volume fraction (Eq. (2.20)). Consequently, the hydrogen content within the anode is very high at small current densities and decreases for higher current densities.

Nevertheless, it is difficult to interpret the hyperbola trend of the hydrogen volume fraction data regarding the hydrogen crossover flux. Therefore, in Fig. 4.1b) the related crossover flux $N_{\text{H}_2}^{\text{cross}}$ is shown, which was calculated by Eq. (2.22). On the second y-axis the crossover flux is converted into a corresponding crossover current density by Faraday's law Eq. (3.3).

In addition to this work, similar hydrogen volume measurements were presented in the literature [11, 100]. These literature results are also shown in Fig. 4.1a) in comparison to the results of this work. Unfortunately, the other experiments were realized with different membrane materials and at different temperatures and pressure conditions. Even so, the measurement results show qualitatively comparable curves, especially the measurement series of Schalenbach et al. [100] shows by comparison with the data of this work very similar results regarding the hydrogen volume fraction profiles (s. Fig. 4.1a)).

The literature hydrogen volume fraction data were also converted into the hydrogen crossover flux by Eq. (2.22), which is shown in Fig. 4.1b). Qualitatively the literature data and the results of this work show the same progression of the crossover flux that increases approximately linear with increasing current density. However, the slopes of this linear trend differ considerably. This differences could originate from the different

materials/composites or manufacturing techniques which are used for the CCMs, etc. Sakai et al. [75] showed for example a notable influence of the catalyst composites on the crossover flux. That means, different CCMs could cause different increases of permeation with current density.

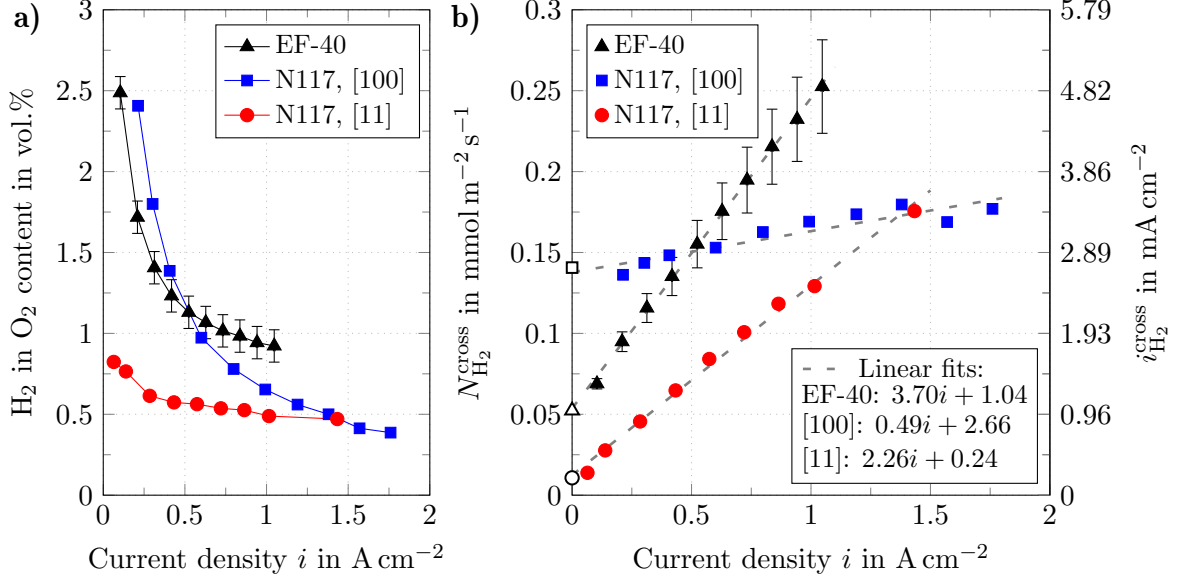


Figure 4.1: Comparison of the measured data of this work (EF-40, $T = 80^\circ\text{C}$, $p^c = 1$ bar) with literature data (Schalenbach et al. [100]: N117, $T = 80^\circ\text{C}$, $p^c = 7$ bar and Grigoriev et al. [11]: N117, $T = 85^\circ\text{C}$, $p^c = 1$ bar): a) hydrogen content and b) hydrogen crossover flux calculated by Eq. (2.22) and corresponding current density. The experimental data are described by linear trendlines $i_{\text{H}_2}^{\text{cross}} = m \cdot i + b$, with slope m in $(\text{mA}/\text{cm}^2)/(\text{A}/\text{cm}^2)$ and y-axis interception b in mA/cm^2 . The theoretical crossover flux (hollow symbols) were calculated by Eq. (4.1) and literature permeation parameters (Tab. 4.1).

In addition to the current dependent experimental results, permeation fluxes at approximately zero current (hollow symbols) with the given operating conditions are calculated according to [86] by Eq. (4.1) and literature values (Tab. 4.1).

$$N_{\text{H}_2}^{\text{cross}} = K_{\text{P,H}_2}^{T_{\text{ref}}} \exp \left[\frac{E_A}{R} \left(\frac{1}{T_{\text{ref}}} - \frac{1}{T} \right) \right] \frac{p_{\text{H}_2}^c}{\delta_{\text{mem}}} \quad (4.1)$$

Herein, $K_{\text{P}}^{T_{\text{ref}}}$ is the membrane permeability coefficient at the reference temperature T_{ref} , E_A the activation energy, R the universal gas constant, δ_{mem} the membrane thickness and $p_{\text{H}_2}^c$ the partial pressure of hydrogen in the cathode (Eq. (2.15)) that is assumed equal to the cathode pressure reduced by the water vapor pressure p_{vap}^c , which was calculated according to Stull [89].

Table 4.1: Literature permeation parameter of the N117 membrane and the membrane of the applied EF-40 CCM for Eq. (4.1).

Parameter	EF-40 [86]	N117 [78]
T_{ref} in K	333	353
$K_{\text{P,H}_2}^{T_{\text{ref}}}$ in $\text{mol Pa}^{-1} \text{m}^{-1} \text{s}^{-1}$	$2.95 \cdot 10^{-14}$	$5.32 \cdot 10^{-14}$
E_A in kJ mol^{-1}	27	20
δ^{mem} in μm	240 (dry)	209 (wet)

It can be seen that the additionally calculated, currentless permeation data (hollow symbols at the y-axis of Fig. 4.1b)) agree very well with the extrapolated current density depending permeation data (y-intersection) of this work (EF-40) as well as for the literature data (N117, [11, 100]). This emphasizes that the measurement of the anodic hydrogen fraction can be used to measure the hydrogen crossover. In the following paragraphs this crossover increase with current density is investigated in more detail by different temperatures and cathode pressures.

4.1.2 Temperature Variation

Effect of temperature on the hydrogen in oxygen volume fraction is shown in Fig. 4.2a) for four different temperatures. An increase in temperature causes moderately higher volume fractions of hydrogen in the anode product gas.

The corresponding hydrogen crossover fluxes are shown in Fig. 4.2b). It can be seen that increasing temperatures lead to higher crossover fluxes. This can be explained due to the higher diffusivity and solubility coefficients at higher temperatures [66, 87, 117]. For all measurement series the hydrogen crossover flux increases linearly with increasing current density (within the investigated current density range). The slopes of the crossover increases with current density indicate an slight increase with temperature (2.68 (30 °C) to 3.70 (80 °C) in $(\text{mA}/\text{cm}^2)/(\text{A}/\text{cm}^2)$).

In comparison to the increase of the crossover rate, caused by an increase in temperature, the effect of the current density is stronger. This is highlighted in Fig. 4.2b) with a gradient triangle. An increase in current density of about 0.12 A cm^{-2} causes for this specific case a similar increase of the crossover rate as a temperature increase of 20 K (originating from the 60 °C measurement series at a current density of 0.4 A cm^{-2}). This emphasizes the strong impact of current density on hydrogen crossover.

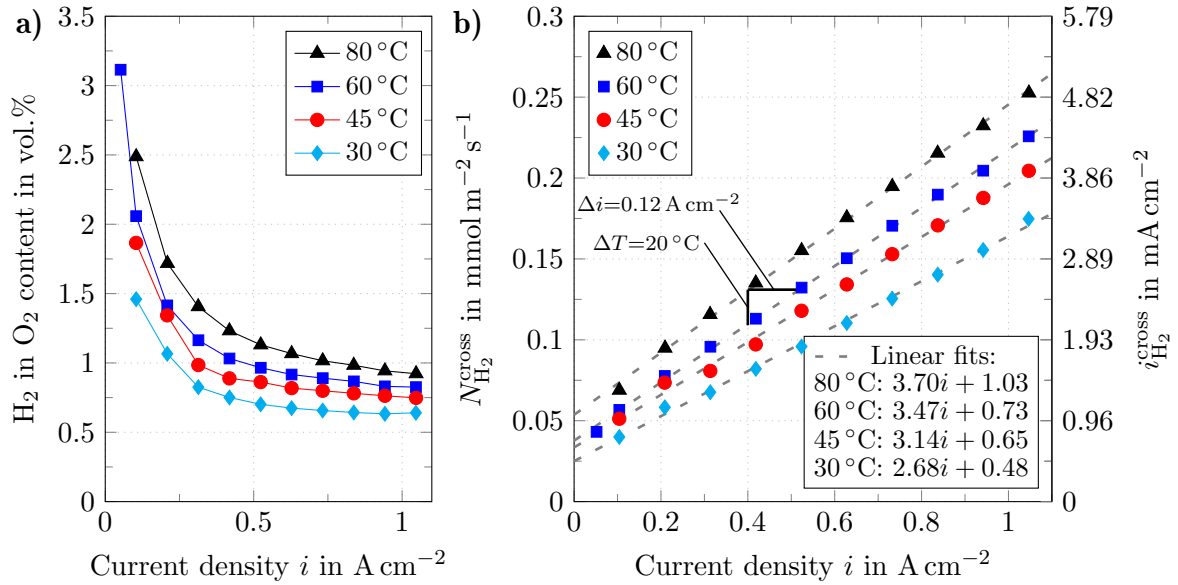


Figure 4.2: Temperature effect at $p^c = 1$ bar on: a) hydrogen in oxygen content and b) hydrogen crossover rate versus current density. The experimental data are described by linear trendlines $i_{\text{H}_2}^{\text{cross}} = m \cdot i + b$, with slope m in $(\text{mA/cm}^2)/(\text{A/cm}^2)$ and y-axis interception b in mA cm^{-2} .

4.1.3 Pressure Variation

Fig. 4.3a) shows the influence of cathode pressure on the hydrogen volume content profiles. Already at a cathode pressure of about 11 bar a current density greater than 0.5 A cm^{-2} has to be applied to satisfy a chosen safety limit of 2 vol.% H₂ in O₂, which is about half of the previously mentioned LEL of about 4 vol.% H₂ in O₂ [17]. The minimal current densities to fulfill this safety limit increase with elevated cathode pressure. At a cathode pressure of 31 bar the current density should already exceed 1.2 A cm^{-2} . This is a very high value despite the thick membrane. A circumstance that strongly reduces the operation range, which leads to the part load issue.

In Fig. 4.3b) the corresponding crossover fluxes for the four different cathode pressures can be seen. Again the crossover of all measurement series increase linear within the observed current density range. The slopes of the linear trendlines indicate to increase slightly with cathode pressure (3.47 (1 bar) to 4.34 (31 bar) in $(\text{mA/cm}^2)/(\text{A/cm}^2)$).

Also here a gradient triangle is used to compare the influence of current density with the influence of cathode pressure on hydrogen crossover (s. Fig. 4.3b)). Originating from the measurement series for 21 bar at a current density of 0.42 A cm^{-2} an increase in current density of about 0.55 A cm^{-2} causes for this specific case a similar increase of the crossover flux as a cathode pressure increase of 10 bar. This also emphasizes the strong impact of the current density on the crossover rate.

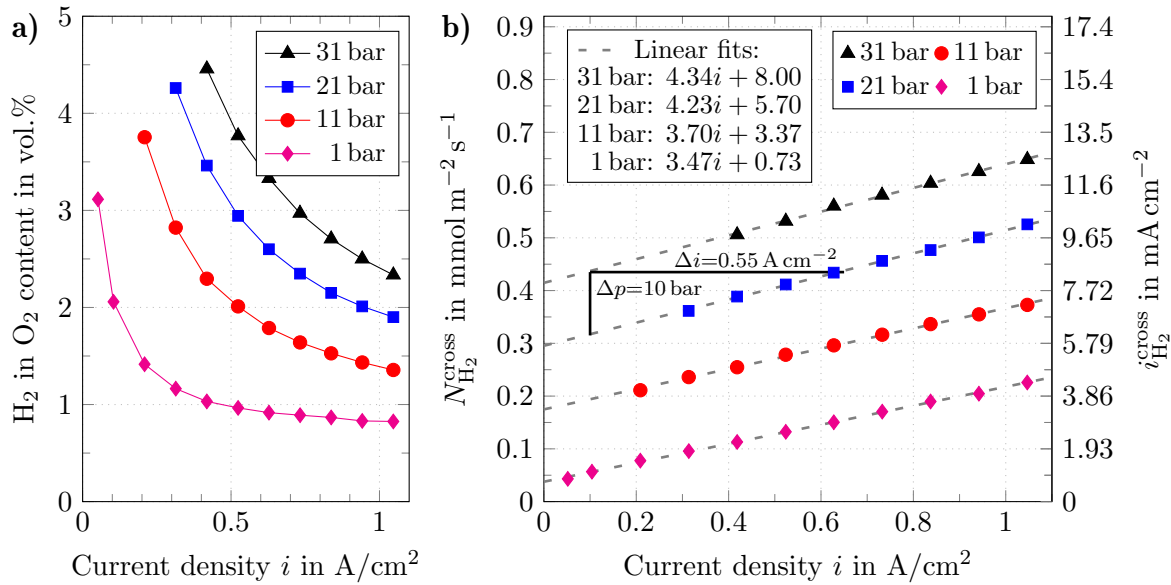


Figure 4.3: Cathode pressure effect at $T = 60^\circ\text{C}$ on: a) hydrogen in oxygen content and b) hydrogen crossover flux versus current density. The experimental data are described by linear trendlines $i_{\text{H}_2}^{\text{cross}} = m \cdot i + b$, with slope m in $(\text{mA}/\text{cm}^2)/(\text{A}/\text{cm}^2)$ and y-axis interception b in mA cm^{-2} .

Conclusions to Research Question 1 The experimental results confirm the literature data. The hydrogen crossover increases with current density. However, the comparison of experimental data with literature data revealed that the slopes of this crossover increase strongly differ (s. Fig. 4.1b)). There are a lot of possible reasons for this, such the usage of different materials (CCMs, PTLs), cell setups, sensors or operating conditions.

However, the previously discussed variations of temperature and cathode pressure show only slight changes of the crossover increase with current density. Especially, the crossover increase is approximately independent of pressure, which should be kept in mind for the following discussion of the theoretical explanation.

4.2 Theoretical Explanation – Supersaturation of dissolved Hydrogen

Neither the local pressure enhancement nor the raise in temperature with increasing current density can explain the experimental findings and there is no evidence for structural changes of the ionomer during PEM water electrolysis, which could explain the crossover increase with current density (s. sec. 2.3). Therefore, a fourth explanation approach is discussed in the following. The theory is based on a hydrogen supersaturation, more precisely a higher concentration of dissolved hydrogen within the ionomer film of the cathode catalyst layer as it would be expected by use of Henry's law. This was also recently suggested by Bessarabov et al. [101]. Additionally, such supersaturations of

dissolved gases were frequently measured [118–121].

The underlying situation is sketched in Fig. 4.4. To explain the hydrogen supersaturation it is assumed that molecular hydrogen is formed within the water of the ionomer film within the cathode catalyst layer as dissolved hydrogen. This dissolved hydrogen has to transfer into the gas state $H_2(g)$ (path A). However, this mass transfer process is limited. Consequently, the dissolved hydrogen concentration $c_{H_2}^*$ within the ionomer is higher than the theoretical concentration (Henry’s law). The higher the applied current density, the higher the dissolved hydrogen evolution, thus leading to a rising supersaturation of dissolved hydrogen. Consequently, this increased hydrogen concentration could lead to the increases in hydrogen crossover.

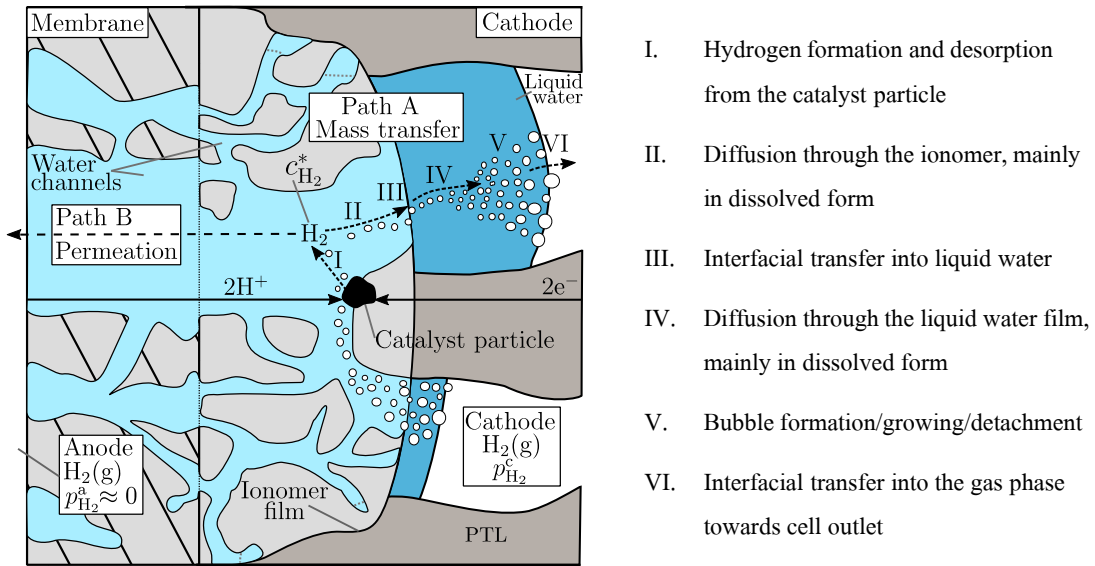


Figure 4.4: Sketch of possible mass transfer steps (Path A, steps: I–VI) of the produced hydrogen. Mass transfer resistances lead to the supersaturation of dissolved gas $c_{H_2}^*$. Path B represents the permeation of dissolved hydrogen across the membrane (crossover).

In the following, a simple model is developed to estimate the hydrogen supersaturation and its impact on hydrogen crossover. Fig. 4.4 shows that the evolving dissolved hydrogen has two possible path ways. Here, for this principal theoretical investigation, the recombination of hydrogen with permeated oxygen is neglected, because of the relatively small oxygen crossover [75,99]. Most of the hydrogen will leave the cathode catalyst layer over path A (mass transfer). This could include several transport mechanisms, which are described in Fig. 4.4 on the right hand side. Path B represents the hydrogen crossover through the membrane. As described in chapter 2, the crossover can be calculated by Fick’s first law of diffusion. The sum of both paths has to be equal to the amount of evolving hydrogen (Eq. (4.2)).

$$0 = \underbrace{\frac{i}{2F}}_{\text{H}_2\text{-Evolution}} - \underbrace{k_1^c (c_{\text{H}_2}^* - c_{\text{H}_2}^{c,\text{sat}})}_{\text{Mass transfer (Path A)}} - \underbrace{D_{\text{H}_2}^{\text{eff}} \frac{c_{\text{H}_2}^* - c_{\text{H}_2}^{\text{a}}}{\delta^{\text{mem}}}}_{\text{Crossover (Path B)}} \quad (4.2)$$

Herein, k_1^c is the integral mass transfer coefficient of the cathode that includes all mass transport resistances, such as desorption, diffusion and bubble formation/growth/detachment, $c_{\text{H}_2}^*$ is the supersaturated hydrogen concentration within the ionomer at the catalyst particles, $c_{\text{H}_2}^{c,\text{sat}}$ is the theoretical saturation concentration of dissolved hydrogen without any mass transport limitations that can be assumed by Henry's law, $D_{\text{H}_2}^{\text{eff}}$ is the effective hydrogen diffusion coefficient, $c_{\text{H}_2}^{\text{a}}$ is the dissolved hydrogen concentration at the anode side, which is assumed to be negligibly small and δ^{mem} is the thickness of the membrane. Hereby, the diffusion from the catalyst particles to the membrane within the catalyst layer ($\delta^{\text{CL}} \approx 10 - 20 \mu\text{m}$) is neglected, because of the considerably smaller distance in comparison to the membrane thickness ($\delta^{\text{mem}} \approx 240 \mu\text{m}$).

By rearranging the balance equation (4.2), the hydrogen concentration at the catalyst particles can be calculated by the following expression:

$$c_{\text{H}_2}^* = \frac{\frac{i}{2F} + k_1^c c_{\text{H}_2}^{c,\text{sat}}}{k_1^c + \frac{D_{\text{H}_2}^{\text{eff}}}{\delta^{\text{mem}}}} \quad (4.3)$$

This concentration of Eq. (4.3) can be inserted into Fick's first law of diffusion (Eq. (2.16)) to calculate the crossover flux. Therefore, the dissolved hydrogen concentration at the anode side $c_{\text{H}_2}^{\text{a}}$ is neglected.

$$N_{\text{H}_2}^{\text{cross}} = D_{\text{H}_2}^{\text{eff}} \frac{\frac{i}{2F} + k_1^c c_{\text{H}_2}^{c,\text{sat}}}{k_1^c \delta^{\text{mem}} + D_{\text{H}_2}^{\text{eff}}} \quad (4.4)$$

Within Eq. (4.4) the saturated dissolved hydrogen concentration of the gas/ionomer interface $c_{\text{H}_2}^{c,\text{sat}}$, the effective hydrogen diffusion coefficient $D_{\text{H}_2}^{\text{eff}}$ and the mass transfer coefficient k_1^c are unknown. The first two quantities can be estimated by Henry's law Eq. (2.14) and by Bruggeman's correction Eq. (2.12), respectively.

For the estimation of the mass transfer coefficient k_1^c several approaches are available [79], such as the penetration theory of Higbie [122] or the film theory of Whitman [123], which will be used in the modelling chapter 6. Ohishi et al. [124] measured indirectly the interface resistance for hydrogen crossover for a Nafion[®] membrane, which can be converted to a cathodic mass transfer coefficient k_1^c in a range of $4 \cdot 10^{-5}$ to $2 \cdot 10^{-4} \text{ m s}^{-1}$. Matsushima et al. [119] measured the hydrogen supersaturation with a current interrupt method and determined mass transfer coefficients in a range of about $5 \cdot 10^{-6} - 5 \cdot 10^{-4} \text{ m s}^{-1}$ depending on the applied current density. For this principal estimation mass transfer coefficients k_1^c in a wide range of $1 \cdot 10^{-5} - 1 \cdot 10^{-1} \text{ m s}^{-1}$ are chosen.

Table 4.2: Parameters for the hydrogen supersaturation model.

Parameter	Value at 60 °C	Unit	Source
S_{H_2}	$7.07 \cdot 10^{-6}$	$\text{mol m}^{-3} \text{Pa}^{-1}$	[87]
D_{H_2}	$1.26 \cdot 10^{-8}$	$\text{m}^2 \text{s}^{-1}$	[117]
$\varepsilon_{\text{H}_2\text{O}}$	0.37		[86]
τ_{ion}	1.5		[86]
p^c	1	bar	
$p_{\text{vap}}^{c,\text{sat}}$	0.2	bar	[89]
δ^{mem}	240	μm	
k_1^c	$1 \cdot 10^{-5} - 1 \cdot 10^{-1}$	m s^{-1}	chosen

After fixing $c_{\text{H}_2}^{c,\text{sat}}$, $D_{\text{H}_2}^{\text{eff}}$ and k_1^c the hydrogen crossover flux through the membrane can be calculated with Eq. (4.4) and the parameters of Tab. 4.2. The results of the supersaturation model are shown in Fig. 4.5. It can be seen that a mass transfer coefficient in the order of magnitude of about $1 \cdot 10^{-3} \text{ m s}^{-1}$ can explain the crossover increase. This value is even above the previously mentioned literature values that means the transport resistances of the investigated system are lower.

For the explanation of the experimental data of Grigoriev et al. [11] and Schalenbach et al. [78] the mass transfer coefficient can be determined even one order of magnitude higher. The corresponding lower mass transfer resistances could be caused by different applied materials, cell setups or manufacturing techniques.

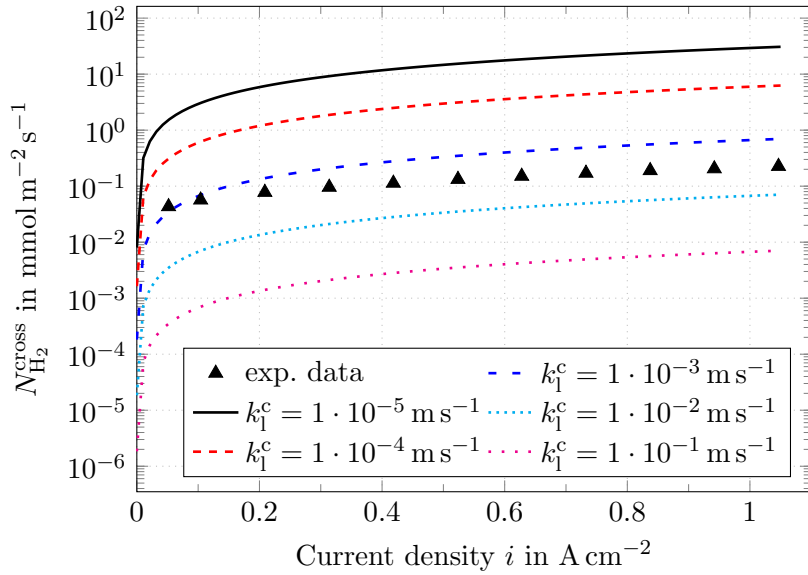


Figure 4.5: Calculated crossover fluxes (Eq. (4.4)) for different mass transfer coefficient k_1^c in comparison with the related experimental data at $p^c = 1 \text{ bar}$ and $T = 60 \text{ °C}$.

Conclusions to Research Question 2 A probable explanation of the crossover increase with current density is the supersaturation of dissolved hydrogen due to a limited hydrogen mass transfer from the cathode catalyst layer towards the cathode outlet. The experimental finding that the crossover increase with current density is nearly pressure independent lead to the assumption that the relevant mass transfer limitations are also pressure independent. Therefore, the diffusive transport of dissolved hydrogen from the catalyst particles through the ionomer/water films towards the pore space is the most evident transport step, since the diffusion coefficient of dissolved gas in water is also pressure independent [66]. This theory is further supported by literature measurements of supersaturated dissolved gas concentrations [118–121] and that the order of magnitude of the required mass transfer coefficient can also be supported by literature values.

4.3 Oxygen Crossover

In the previous sections of this chapter the effect of current density on hydrogen crossover are investigated experimentally and theoretically. It seems likely that this supersaturation effect also occurs on the anode side with the dissolved oxygen. Consequently, the oxygen crossover might also increase with current density (RQ 3). This section is based on the following publication: P. Trinke, B. Bensmann and R. Hanke-Rauschenbach: Experimental Evidence of Increasing Oxygen Crossover with Increasing Current Density during PEM Water Electrolysis (2017). *Electrochem. Commun.* **82**, 98–102, doi.org/10.1016/j.elecom.2017.07.018.

Unfortunately, the oxygen crossover can not be measured as simply as the hydrogen crossover, since the permeating oxygen recombines with evolved hydrogen to water at the cathodic state of the art catalyst, Pt. For this experimental study the baltic cell with identical anode PTLs, identical cathode PTLs and two commercial CCMs from HIAT were used. These CCMs were identical concerning the anode catalyst layers and membrane material, but the CCMs had different cathode catalysts. One CCM contained the state of the art catalyst platinum and the other CCM contained a Pt-free catalyst. As stated in chapter 2, platinum group metals (PGM) free catalyst are one important research field to reduce investment costs. However, this is not the point of interest of this section. The catalyst manufacturer stated that this Pt-free catalyst is very inactive towards the oxygen reduction reaction (ORR), which represents the fuel cell reactions of the cathode. That means, this Pt-free catalyst has a low activity toward the reduction of oxygen, whereas Pt is the state-of-the-art catalyst material for the ORR. Consequently, the Pt-free catalyst might lead to a lower recombination reaction of permeated oxygen. Hence, it could be possible to measure the permeated oxygen molecules within the cathode product gas.

Polarization Behavior For sake of completeness the polarization curves of both CCMs with the different cathodic catalyst materials are shown in Fig. 4.6. It can be seen, that the CCM with the Pt-free catalyst has as expected a higher cell voltage. This can be explained mainly by the lower activity towards the hydrogen evolution reaction, which

can be seen at low current densities. However, the main focus is on the oxygen crossover, which is discussed in the following.

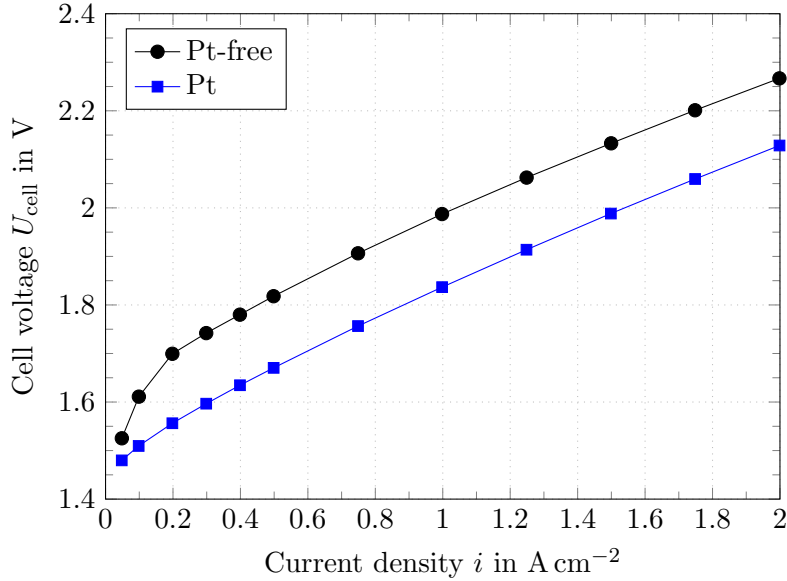


Figure 4.6: Polarisation curves for the Pt-free and Pt catalyst at $T = 70^\circ\text{C}$ and ambient pressure.

Oxygen Crossover In Fig. 4.7 the measured oxygen content within the cathode product gas is plotted versus the current density for both investigated cathode catalysts. Additionally, the theoretical oxygen content is shown due to pure diffusive oxygen crossover without supersaturation. This crossover flux was calculated by literature values of Schalenbach et al. [78] and Eq. (3.4).

It can be seen that the oxygen in hydrogen content is higher at small current densities, decreases with increasing current density and is almost constant at higher current densities. The trend of the experimental data is qualitatively close to the theoretically hyperbolic trend as it is also shown and expected, since the evolving hydrogen flux increases with current density and thus the oxygen in hydrogen content should decrease. Overall, the oxygen fraction in hydrogen is small in comparison to the previously shown anodic hydrogen in oxygen content. This can be explained by the low anode pressure (atmospheric), thick membrane (N117, 180 μm), smaller oxygen crossover in comparison to the hydrogen crossover due to a lower oxygen diffusion coefficient and due to the two times higher hydrogen evolution rate in comparison to the oxygen evolution and consequently a higher dilution of the permeated oxygen in produced hydrogen. However, this oxygen content (impurity) is for many hydrogen applications still higher than the required purities [125]. In this case, a further processing of the hydrogen product gas would be necessary.

At high current densities ($>0.5 \text{ A cm}^{-2}$) the measured oxygen in hydrogen content of both measurement series lies above the theoretical value, although a portion of the

permeated oxygen should be consumed within the cathode catalyst layer. Additionally, it can be seen that the oxygen volume fraction of the measurement series with the Pt-free catalyst is approximately 3–4 times higher than the oxygen content measured with Pt as catalyst material. This was expected, since the Pt-free catalyst has a lower activity regarding the oxygen reduction reaction in comparison to Pt (manufacture information). Hence, it is assumed that in case of the measurement series with the Pt-free catalyst less of the permeating oxygen will recombine, thus leading to a higher oxygen content within the cathode outlet. However, the Pt-free catalyst is still active for the oxygen recombination, since at the beginning of the activation phase higher oxygen contents were measured and during the activation phase the oxygen content decreased. Hence, at the beginning the Pt-free catalyst was less active regarding the oxygen recombination and after the activation phase the catalyst activity was increased. Consequently, the oxygen content at the cathodic membrane interface has to be even higher as it is measured within the cathode outlet.

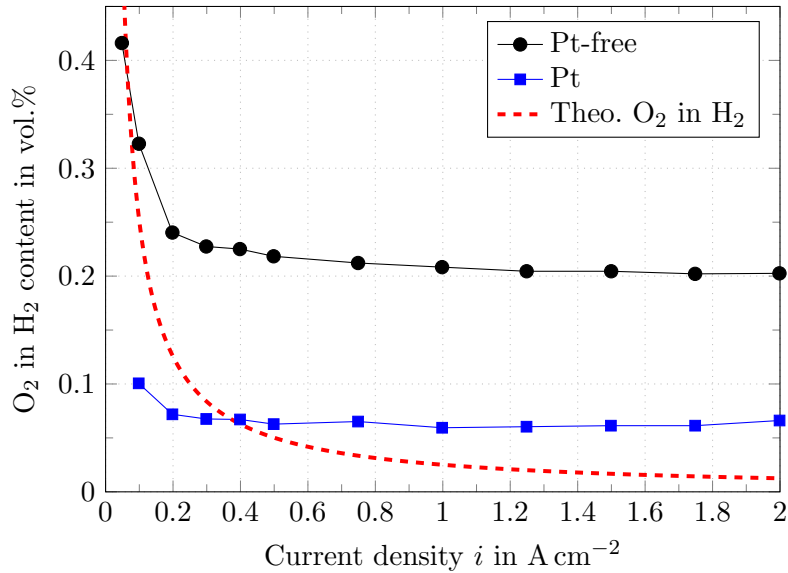


Figure 4.7: Oxygen volume fraction within the hydrogen product gas versus current density for the Pt-free and Pt catalyst. Operation conditions: $T = 70^\circ\text{C}$, ambient pressure.

In Fig. 4.8 the oxygen flux within the cathode outlet is plotted over the current density, which was calculated according to Eq. (3.4) by use of the data of Fig. 4.7 (cathodic oxygen content and current density). As can be seen for both measurement series, the cathodic oxygen outlet fluxes increase linearly with increasing current density, which is comparable to the observed hydrogen crossover increase with current density.

Additionally, the theoretical oxygen crossover according to the operating conditions and literature values [78], is plotted in Fig. 4.8. This value helps to evaluate the experimentally derived data. The theoretical oxygen crossover is calculated without supersaturation due to pure permeation measurements at saturation conditions.

Previously, it is discussed that a supersaturation of dissolved hydrogen can explain the hydrogen crossover increase with current density. Consequently, it is assumed that the same phenomenon occurs with oxygen in the anode catalyst layer. Particularly, as supersaturation of oxygen was also measured in literature [126, 127]. Due to the strong crossover increase with current density, the oxygen fluxes of both measurement series are several times higher than the calculated theoretical oxygen crossover rate, despite that the recombination of oxygen reduces the measured oxygen flux. For example at a high current density of 2 A cm^{-2} the cathodic oxygen flux of the Pt-free measurement series is approximately 15 times higher than expected. Consequently, the supersaturation of dissolved oxygen within the anode catalyst layer has to be at least 15 times higher than the saturation concentration according to Henry's law.

However, additional to the increased diffusive crossover due to the supersaturation of dissolved oxygen within the anode catalyst layer, the electro-osmotic drag could also lead to increased oxygen crossover fluxes. This is also considered in a model of Grigoriev et al. [90]. Therefore, the oxygen crossover due to the electro-osmotic drag can be roughly estimated by Eq. (4.5), which is discussed sec. 2.2.1.

$$N_{\text{O}_2, \text{conv, drag}}^{\text{cross}} \approx v_{1, \text{drag}} c_{\text{O}_2}^* \approx n_{\text{drag}} \frac{i}{F \frac{\rho_1}{M_{\text{H}_2\text{O}}}} c_{\text{O}_2}^* \quad (4.5)$$

Herein, $v_{1, \text{drag}}$ is the velocity of liquid dragged water that can be estimated by a drag coefficient n_{drag} (≈ 2 [91]), current density i in A m^{-2} , Faraday constant F , the density of liquid water ρ_1 and the molar mass of water $M_{\text{H}_2\text{O}}$. The supersaturated concentration of dissolved oxygen gas $c_{\text{O}_2}^*$ can be estimated as the product of the saturated concentration, that can be described as the product of the partial pressure of oxygen $p_{\text{O}_2}^{\text{a}}$ (here $0.79 \cdot 10^5 \text{ Pa}$) and the oxygen solubility in water S_{O_2} of $9.8 \cdot 10^{-6} \text{ mol Pa}^{-1} \text{ m}^{-3}$ [66] and a supersaturation factor of 15. For this supersaturation the oxygen crossover due to electro-osmotic drag can be calculated to $0.087 \text{ mmol m}^{-2} \text{ s}^{-1}$. This is nearly 40 % of the experimentally derived cathodic oxygen flux (s. Fig. 4.8), which represents a relatively high part. However, the real oxygen crossover flux is still higher as the observed cathodic oxygen flux, due to recombination. Consequently, the electro-osmotic drag might amplify the oxygen crossover to a certain extent. Because of the rough estimation this should be handled with care, but also it should be investigated in more detail, since the influence of the electro-osmotic drag was not investigated yet.

Furthermore, in Fig. 4.8 it can be seen, that at small current densities ($i < 0.3 \text{ A cm}^{-2}$) the determined cathodic oxygen flux is smaller than the calculated theoretical oxygen crossover rate. This is attributed to the recombination of permeated oxygen. At low current densities the oxygen crossover increases are small, so that due to the recombination of permeated oxygen the cathodic oxygen outlet flow can be smaller than the theoretical oxygen crossover. However, due to supersaturation and also probably due to the electro-osmotic drag the real oxygen crossover could be higher than the calculated theoretical crossover value even at low current densities.

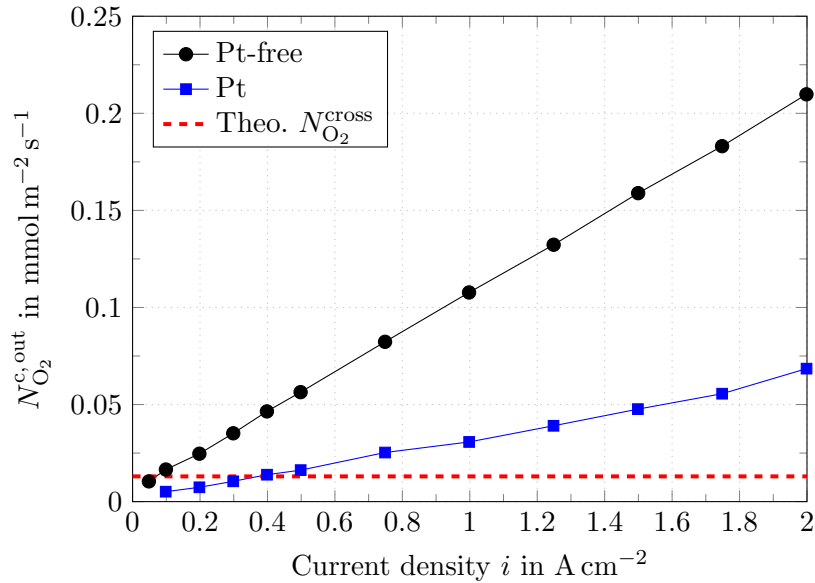


Figure 4.8: Oxygen flux within the cathode outlet versus current density for the Pt-free and Pt catalyst. Additionally, the theoretical oxygen crossover rate $N_{O_2}^{cross} = 0.013 \text{ mol m}^{-2} \text{ s}^{-1}$ is depicted. The electrolysis cell was operated at $T = 70^\circ \text{C}$ and ambient pressure conditions.

Conclusions to Research Question 3 The measured oxygen in hydrogen content of the cathodic product gas leads to the assumption that the oxygen crossover also increases quasi linearly with the current density. The experimental results with the special Pt-free catalyst highlight that the oxygen crossover can be far higher than stated in literature. The electro-osmotic drag of water molecules could cause a convective transport of dissolved oxygen, which also could enhance the oxygen crossover. However, the applied Pt-free catalyst material might still have an activity towards the recombination of permeating oxygen with hydrogen to water, hence the real oxygen crossover could be even higher. Because of this uncertainty the oxygen crossover is not further analyzed in this dissertation, since also the main focus lies on the investigation of the hydrogen crossover.

4.4 Concluding Remarks

In this chapter, measurements of the hydrogen in oxygen content of the anode side for different operating conditions and also measurements of the oxygen in hydrogen content by means of a special cathode catalyst are shown. The concentration measurements of the permeated hydrogen and oxygen can be used to calculate the hydrogen and oxygen crossover fluxes. The experimental data show that both the hydrogen and oxygen crossover fluxes increase with current density.

The extrapolated y-axis interception of the crossover fluxes ($i = 0$) agree very well with crossover data of the literature. Consequently, the measurement of the permeated

gas concentration cannot only be used for safety issues, but also for measurement and characterization of gas crossover. This can help by comprehensive investigations of PEM water electrolysis cells. Especially, the information of the gas crossover increase with current density can be used to determine mass transport parameters for different materials, cell setups and should be analyzed in more detail to understand the underlying mechanisms. This could help to reduce the crossover increases with current density.

The comparison to literature results shows that the crossover increase with current density strongly differs for different cell setups (cells, materials). Whereas, the effect of operating conditions as temperature and pressure are not so strong. The finding that the hydrogen crossover increase with current density is approximately constant for different cathode pressures indicates that the mass transfer limitations are pressure independent. Consequently, it is very unlikely that the gas transport within the pore volume has a significant impact on the mass transport limitations, since the gaseous mass transport is significantly improved at higher pressures.

The most suitable explanation approach is the theory of supersaturated dissolved gas concentrations within the catalyst layer. The transfer limitations might mainly be caused by the pressure independent transport of dissolved gas from the catalyst particles through the ionomer/water films towards the pore space. This is investigated in more detail within the next chapter.

5 Influence of Ionomer Content on Crossover and Cell Performance

Within the previous chapter the experimental findings showed that the hydrogen and oxygen crossover increase with current density. The most likely explanation is the supersaturation of dissolved gases within the water of the catalyst layer ionomer. Measurements at different cathode pressures indicated that the crossover increase is almost pressure independent. Consequently, the mass transfer resistances that cause the supersaturated dissolved gas concentrations are assumed to originate from the transport through the water of the ionomer or the mass transfer from the dissolved to the gaseous phase, but are not caused by the mass transport on the gas side. To confirm this, further experiments were performed. The results should also give an answer to the fourth research question:

Research Question 4: *“What is the influence of the electrode structure on the current density effect on gas crossover”*

For this purpose, the ionomer content of the cathode catalyst layer is changed between 10 and 40 wt.% to change the resistances of the mass transport through the ionomer within the cathode catalyst layer and consequently to change the crossover increase with current density. The ex-situ characterization of the cathode catalyst layers with the ionomer variation is shown in the first section. Subsequently to this, the main topic of this chapter is discussed in section 5.2: the effect of ionomer content on the hydrogen crossover. Furthermore, in section 5.3 it is shown that the ionomer content not only affects the crossover, but also the cell voltage. That means both crossover and mass transport losses can be correlated to each other. Finally, the effects of cathode ionomer content on crossover and cell voltage are summarized and discussed in section 5.4.

This chapter is based on the joint publication with the group of Dr. Marcelo Carmo at the Forschungszentrum Jülich GmbH, Institute of Energy and Climate Research, former IEK-3: Electrochemical Process Engineering: P. Trinke, G. P. Keeley, M. Carmo, B. Bensmann and R. Hanke-Rauschenbach: Elucidating the effect of mass transport resistances on hydrogen crossover and cell performance in PEM water electrolyzers by varying the cathode ionomer content (2019). *J. Electrochem. Soc.* **166** (8), F465-F471, doi.org/10.1149/2.0171908jes.

5.1 Ionomer Variation

For the variation of the mass transfer coefficient within the cathode catalyst layer the cathode ionomer content was varied. The preparation and imaging was done at the Forschungszentrum Jülich, which are described in the following.

Preparation of the CCMs with Ionomer Variation Fig. 5.1 shows the preparation process of the modified CCMs that were fabricated using a doctor-blade and decal method to transfer suitable cathode catalyst layers onto the plain membrane of the commercial half-side coated anodes (HIAT gGmbH).

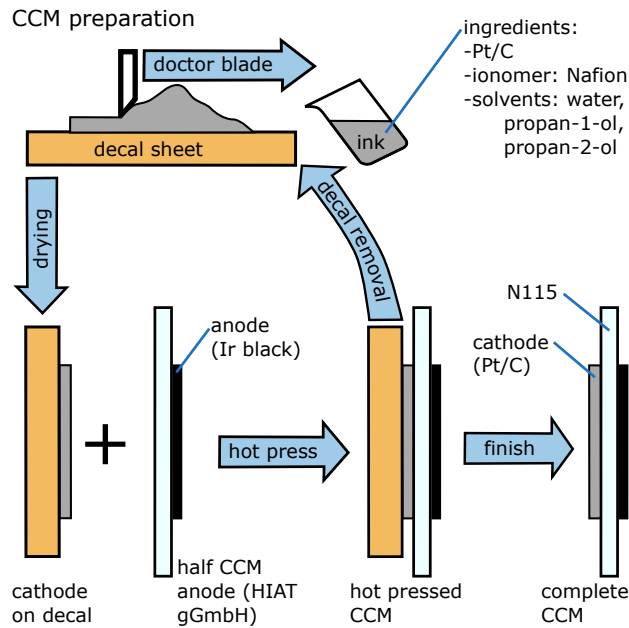


Figure 5.1: Scheme of the CCM preparation process of the variation of the cathode ionomer content via doctor blading in combination with a decal method on commercially available half-sided CCMs.

To prepare the transferable cathodes, 60% Pt/C (HiSPEC 9100, Johnson & Matthey) and various amounts of ionomer solution (LQ 1115 15 wt.% Nafion[®]) were dispersed in a mixture of water, organic solvent, as well as an organic additive in cylindrical glass containers. The mixtures were homogenized in an ultrasonic device (Bandelin HD3200) for 2-10 min and then deposited on inert decal substrates using automated bar coating (Coatmaster 509 MCI, Erichsen GmbH & Co. KG). The bare sides of the commercially available half-sided CCMs were cleaned, and the dried cathode layers were hot-pressed on at a temperature of 150 °C for around 10–15 min. The final cathode loadings were about $0.8 \text{ mg}_{\text{Pt}} \text{ cm}^{-2}$.

Imaging of the Ionomer Variation For cross-section imaging, strips of the dried CCMs were embedded in epoxy resin and polished. Images were recorded using a Carl Zeiss scanning electron microscope (SEM) Gemini Ultra Plus. To determine the elemental distribution across each cathode layer, energy-dispersive X-ray spectrometry (EDS) line-scans were performed across the layer thickness with a lithium-drifted silicon detector from Oxford Instrument Pentax FET.

For each CCM, approximately 10 EDS line-scans were taken inside of the cathode electrodes to investigate if there were inhomogeneities. The mean weight percentage of

fluorine of the different cathodes is simply the average of all EDS line-scans.

Fig. 5.2 shows SEM cross sections and element mapping of platinum and fluorine of the four different cathode catalyst layers with varied ionomer content. The SEM/EDS measurements were performed after the electrochemical characterization. The cathode catalyst layers are relatively thick (23 – 25 μm), but there are no significant differences in the electrode thickness. This was also shown by Bernt and Gasteiger [23] for electrolyzer anodes, when varying the ionomer content within the anode catalyst layer.

The element mapping of Pt and F lead to the assumptions that the catalyst and the fluorine containing ionomer are quite homogeneously distributed within the cathode catalyst layers. The average weight percentages of fluorine within the different cathode catalyst layers show that the ionomer content was successfully varied by the cathode catalyst manufacturing.

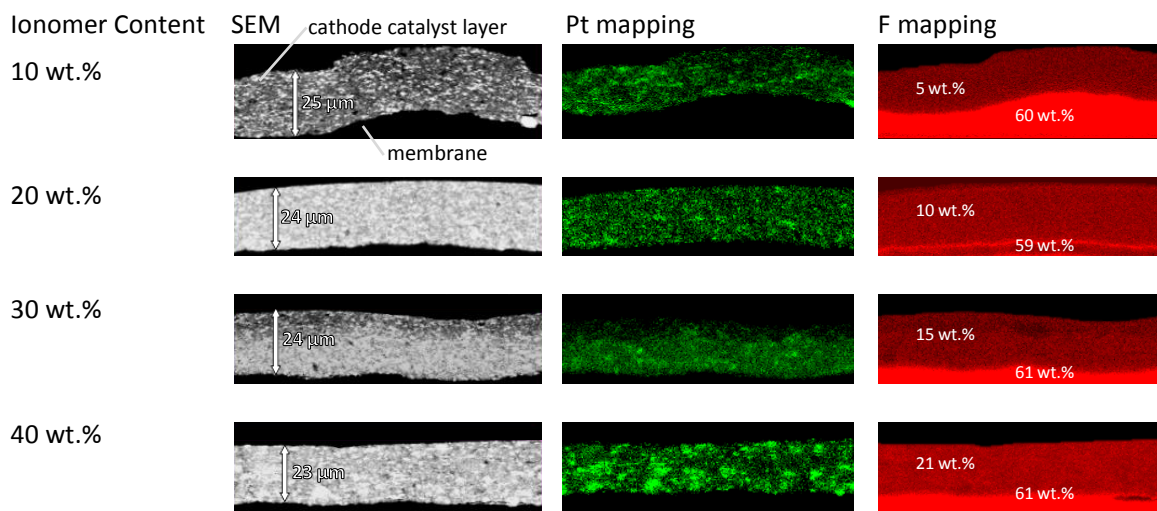


Figure 5.2: SEM cross sections of the cathode catalyst layers with varied ionomer content. Additionally the element mapping of platinum (green) and fluorine (red) are shown. The weight percentages for the fluorine content are averaged values for the catalyst layer and membrane.

5.2 Effect on Hydrogen Crossover

The CCMs were experimentally characterized within the baltic cell (s. sec. 3.3). Fig. 5.3 shows the results of the hydrogen crossover investigation. In Fig. 5.3a) the measured hydrogen in oxygen content is plotted against current density. It can be seen that the H_2 in O_2 content is larger for the CCMs with higher ionomer contents. Despite the fact that these measurements were performed at atmospheric pressure conditions and with relatively thick N115 membranes the hydrogen in oxygen contents are very high for the CCMs with 30 and 40 wt.% ionomer, around 1 and 2 vol.% at 2 A cm^{-2} , respectively.

That means, there is a clear strong influence of high cathode ionomer loadings on the hydrogen in oxygen content.

The corresponding hydrogen crossover fluxes are shown in Fig. 5.3b), which are calculated by Eq. (2.22) from the measured H_2 in O_2 contents of Fig. 5.3a). Fig. 5.3b) shows that the hydrogen crossover increases with increasing current density for all ionomer contents. However, the slopes are significantly higher for the CCMs with higher ionomer contents. Nevertheless, all four CCMs have similar y-axis intersections. This behavior is expected, since the y-axis intersection (zero applied current) should be equal to the hydrogen crossover at saturated conditions [18]. Hence, the intersection should be equal for all CCMs, since they all consist of N115 membranes and were characterized under the same operating conditions, e. g. temperature, pressure.

The dashed lines of Fig. 5.3b) represent the hydrogen crossover fluxes that are fitted to the experimental results by using Eq. (4.4). Parameter values are given in Tab. 5.1. The single fitting parameter is the integral cathodic mass transfer coefficient k_1^c that is determined for each of the specific cathode catalyst layers separately.

Table 5.1: The operating conditions and necessary parameter values for Eq. (4.4).

Parameter	values at $T = 80^\circ\text{C}$
Membrane thickness δ^{mem}	125 μm
Hydrogen solubility S_{H_2}	$7.6 \cdot 10^{-6} \frac{\text{mol}}{\text{Pa}\cdot\text{m}^3}$ [87]
Diffusion coefficient D_{H_2}	$6.9 \cdot 10^{-9} \text{m}^2 \text{s}^{-1}$ [66]
Membrane water fraction $\varepsilon_{\text{H}_2\text{O}}$	0.42 [128]
Effective diffusion coefficient $D_{\text{H}_2}^{\text{eff}} = \varepsilon_{\text{H}_2\text{O}} D_{\text{H}_2}$	$2.9 \cdot 10^{-9} \text{m}^2 \text{s}^{-1}$
Cathode pressure p^c	$1 \cdot 10^5 \text{Pa}$
Saturated vapor pressure $p_{\text{vap}}^{\text{sat}}$	$0.47 \cdot 10^5 \text{Pa}$ [89]
Partial hydrogen pressure $p_{\text{H}_2}^c = p^c - p_{\text{vap}}^{\text{sat}}$	$0.53 \cdot 10^5 \text{Pa}$
Saturated hydrogen conc. $c_{\text{H}_2}^{c,\text{sat}} = p_{\text{H}_2}^c S_{\text{H}_2}$	0.36mol m^{-3}

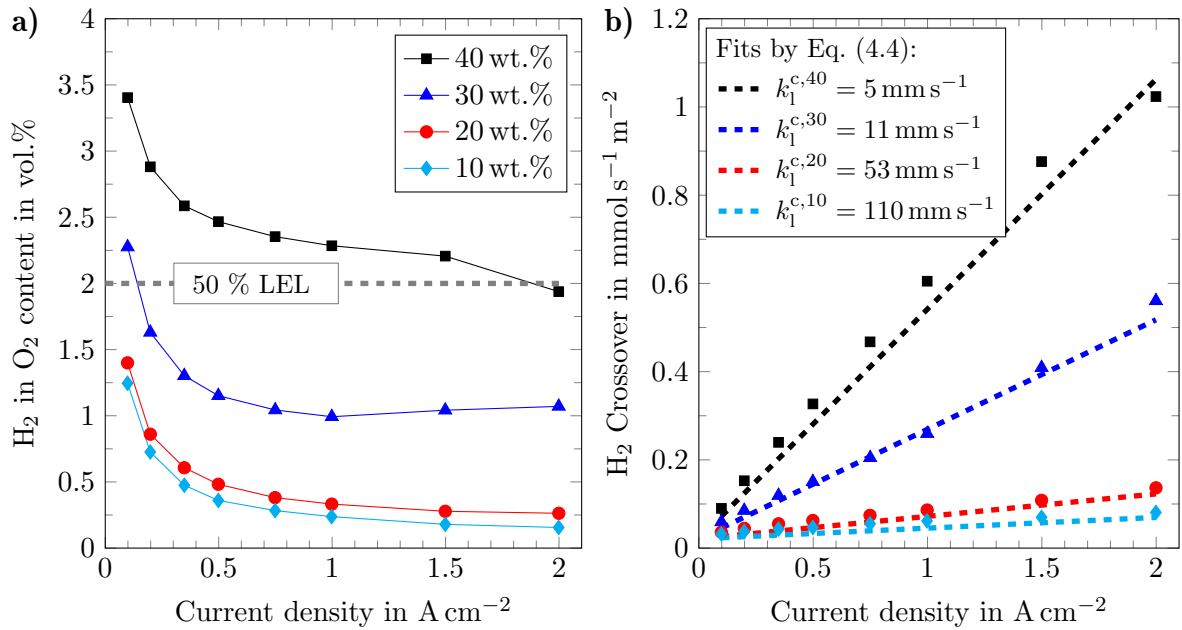


Figure 5.3: Subfigure a) shows the measured H₂ in O₂ content and b) shows the H₂ crossover vs. current density. The dashed lines of b) were fitted by Eq. (4.4) with the parameters of Tab. 5.1. The single fitting parameter is the cathode mass transfer coefficient k_1^c , which is stated for each cathode catalyst layer in the text box.

The fitted crossover data with the determined cathodic mass transfer coefficients k_1^c agree quite well to the experimental results. It was found to be between 5 mm s^{-1} and 110 mm s^{-1} for the 40 wt.% and 10 wt.% CCM, respectively. These results agree with the previously observed value of 3 mm s^{-1} for the fumea EF-40 CCM and with the calculated mass transfer coefficients by literature data, which can be also up to one order of magnitude higher (s. ch. 4). The cathode mass transfer coefficient determined in this work decreases with increasing cathodic ionomer content, which means that the mass transfer resistance increases with ionomer content. An explanation of this might result from structural changes within the catalyst layers. The following three properties are influenced if the ionomer content is increased:

- i) decrease in hydraulic permeability: influenced by the decreasing pore space and increasing tortuosity of the pore volume. This reduces the hydraulic gas transport within the pore space.
- ii) increase in ionomer film thickness: more ionomer results in longer pathways for the diffusive transport of produced dissolved hydrogen from the catalyst particles towards the pore space.
- iii) decrease in volume specific surface of the pores: this reduces the interface between ionomer and pore space, which reduces the transfer of dissolved gas towards the gas state.

In summary, the mass transfer resistance of produced dissolved hydrogen towards the pore space of the catalyst layer is increased with increasing ionomer content. This is attributed to the reduction in pore space, by filling with ionomer. The resulting decrease in pore space, longer ionomer pathways and less available interfaces hinders the transfer of dissolved gas out of the catalyst layer. These three points were recently shown by use of FIB-SEM tomography of a PEM water electrolyzer anode and modelling of various ionomer contents by Hegge et al. [129].

Dissolved Hydrogen Concentration The supersaturated dissolved hydrogen concentration $c_{\text{H}_2}^*$ of the cathode catalyst layers follows from Eq. (4.3) and is shown in Fig. 5.4. Additionally, the saturated dissolved hydrogen concentration is plotted, which is around 0.36 mol m^{-3} at atmospheric cathode pressure and 80°C . Fig. 5.4 shows that the calculated dissolved hydrogen concentration during PEM water electrolysis is several times higher than the saturated concentration. For the 40 wt.% CCM at 2 A cm^{-2} the concentration is more than 50 times higher than the saturation concentration, whereas for the 10 wt.% CCM it is only 5 times higher. However, each CCM shows supersaturated dissolved hydrogen concentrations that increase with current density.

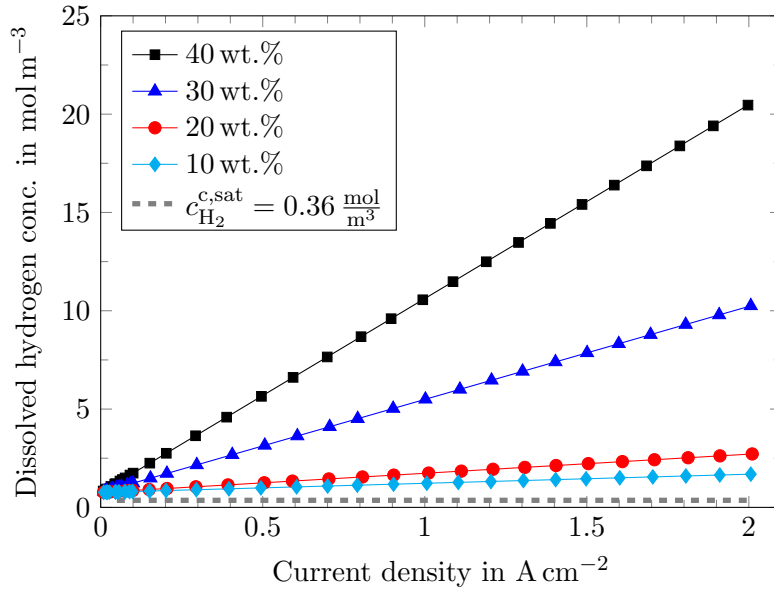


Figure 5.4: The supersaturated dissolved hydrogen concentration $c_{\text{H}_2}^*$ of the different CCMs, which is calculated by Eq. (4.3) and the determined mass transfer coefficients k_1^c of Fig. 5.3b). Additionally, the saturated hydrogen concentration $c_{\text{H}_2}^{c,\text{sat}}$ (grey, dashed line) is plotted, which correspond to operating conditions: 80°C and atmospheric pressure.

Conclusions to Research Question 4 The variation of the cathode ionomer content within the cathode catalyst layer shows a strong influence on the hydrogen crossover. Consequently, as assumed the structural design of the catalyst layers has a strong effect

on the mass transport and hence on gas crossover. It may be presumed that the different crossover increases with current density of the literature data are mainly caused by structural differences of the applied materials. Also other design parameter, such as catalyst loading, porosity or particle/pore diameter, might have also significant influences on the mass transfer and gas crossover.

5.3 Effect on Cell Performance

As previously shown, the cathode ionomer content has a strong effect on hydrogen crossover. For higher ionomer contents the mass transfer is limited more strongly, which leads to highly supersaturated dissolved gas concentrations. This has also an effect on the electrochemical cell performance that is investigated in this section.

5.3.1 Differences in Cell Voltage

Fig. 5.5 shows the electrochemical performance of the tested CCMs, namely the cell voltage as well as R_{HFR} and iR -free cell voltage, which are plotted against current density. In Fig. 5.5a) the polarization curves are shown. CCMs with high ionomer contents (30 and 40 wt.%) show higher cell voltages than the CCMs with lower ionomer contents (10 and 20 wt.%), for which the polarization curves are quite similar.

In Fig. 5.5b) the HFRs of all CCMs are shown. The differences between the CCMs are small ($<10 \text{ m}\Omega \text{ cm}^2$). The major part of the HFRs come from the used N115 membranes. The anode system is not changed and the resistances of the catalyst layers are not included within the HFR [130]. Therefore, only the different cathodic catalyst layer/PTL interfaces could lead to changes in HFR, but no trend can be seen. Consequently, the HFR is not significantly influenced by the variation of cathodic ionomer content.

The inset of Fig. 5.5b) shows Nyquist plots for each CCM at a current density of 0.1 A cm^{-2} . The Nyquist plot shows that the measured impedance data depicts no perfect semicircles, each of the semi arcs is flatter than wide. It can be seen that the HFR is very similar for each CCM, whereas the low frequency resistance (LFR) is higher for the CCMs with higher ionomer contents. This is in perfect agreement with the resistance values obtained from the slopes of the polarization curves (cf. Fig. 5.5a)).

The iR -free cell voltage profiles are shown in Fig. 5.5c), which can be calculated by subtracting the ohmic losses (iR_{HFR}) from the cell voltage. It can be seen that the voltage differences between the CCMs, which were observed in the cell voltage (s. Fig. 5.5a)), are still there. Also the iR -free cell voltage is higher for the CCMs with higher cathode ionomer contents (30 and 40 wt.%) than for the CCMs with lower ionomer contents (10 and 20 wt.%). Consequently, the voltage differences are not caused by ohmic losses (membrane or contact), but rather by losses, which have their origin directly within the cathode catalyst layer, e. g. mass and proton transport losses. The origin of these voltage differences are investigated in more detail in the following paragraphs.

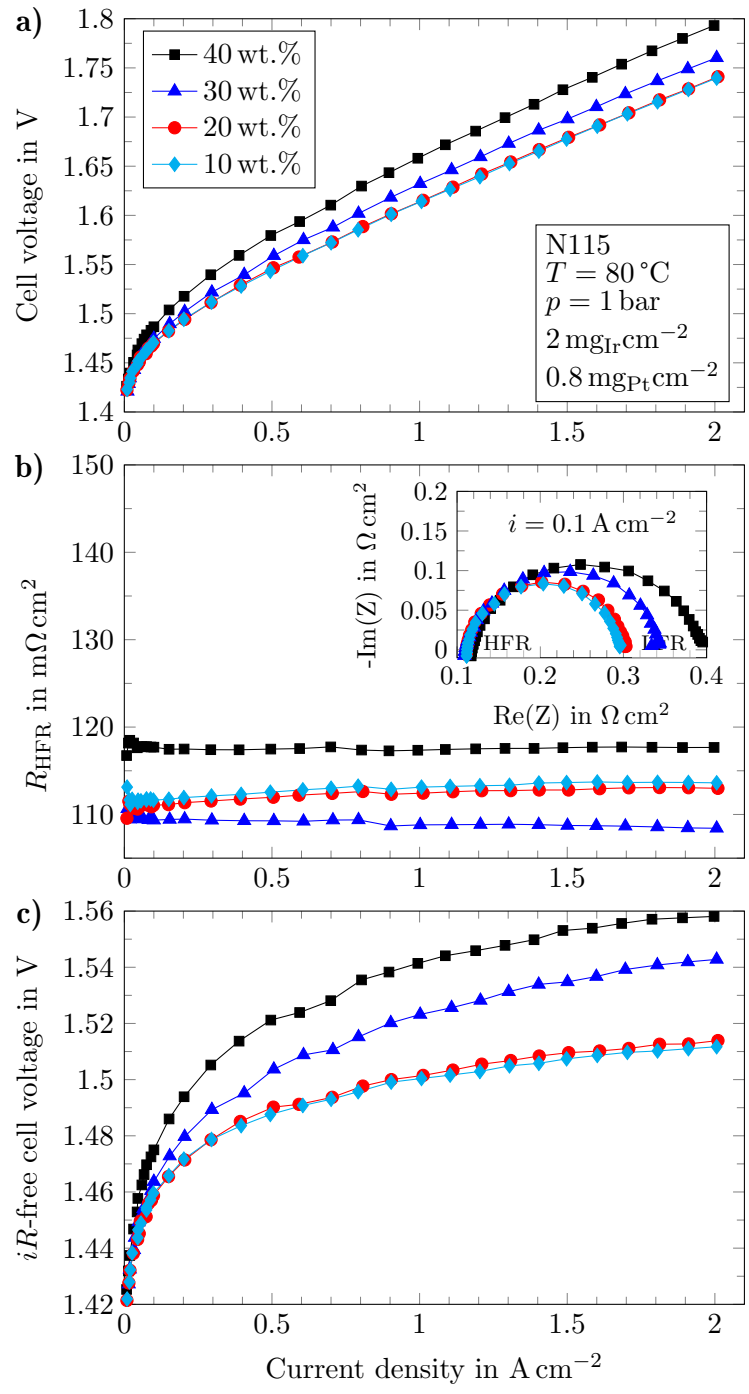


Figure 5.5: Performance comparison for the different CCMs: a) cell voltage, b) HFR and c) iR -free cell voltage plotted versus the applied current density. The inset in b) is a Nyquist plot at 0.1 A cm^{-2} . The high ionomer contents show significantly higher cell voltages, which also remain in the iR -free cell voltage.

5.3.2 Mass Transport Losses

Since the anode was kept constant, the differences of the iR -free cell voltage should be caused by losses on the cathode side, such as ohmic losses within the catalyst layers or mass transport losses. It is not trivial to analyze the remaining losses without further detailed experiments. However, due to the measured hydrogen in oxygen content and the calculated supersaturated concentration of dissolved hydrogen (s. Fig. 5.4) the losses due to cathodic mass transport can be estimated. Therefore, it is assumed that the mass transport losses can be calculated by the Nernst Eq. (5.1), without considering the effects on kinetic and affected proton transport. Consequently, the supersaturated hydrogen concentrations lead to increases in the cathodic half-cell potential ΔE^c that are considered by the concentration dependence of the Nernst Eq. (5.1) for the cathodic half-cell:

$$\Delta E^c = \frac{RT}{2F} \ln \left(\frac{c_{\text{H}_2}^*}{c_{\text{H}_2}^{\text{ref}}} \right) \quad (5.1)$$

where $c_{\text{H}_2}^{\text{ref}}$ is chosen to be equal to the saturation concentration $c_{\text{H}_2}^{\text{sat}}$ of 0.36 mol m^{-3} . Consequently, the increase of the cathodic half-cell potential ΔE^c can be calculated by Eq. (5.1) and the determined supersaturated hydrogen concentration of the crossover measurement (s. Fig. 5.4). Fig. 5.6a) shows the typical logarithmic Nernst correlation between the supersaturated hydrogen concentrations shown in Fig. 5.4 and the half-cell potential. Accordingly, the half-cell potentials are also higher for the CCMs with higher ionomer contents. For example at a current density of 2 A cm^{-2} cell voltage losses between 10 and 50 mV can be attributed to the increased dissolved hydrogen concentration due to mass transport losses.

Fig. 5.6b) shows the concentration corrected iR -free cell voltage, when subtracting the concentration increased cathodic half-cell potential ΔE^c Eq. (5.1) from the iR -free cell voltage. The resulting concentration corrected iR -free cell voltage curves agree quite well with each other. For the purpose of comparison, the not corrected iR -free cell voltage curves are also plotted with hollow marks and transparent. It can be seen that the curves get closer if corrected by the individual mass transport losses. It can be suggested that the voltage differences mainly come from the changes in cathodic half-cell potential that are caused by supersaturated hydrogen concentrations due to different mass transfer resistances of the CCMs with varied cathodic ionomer content.

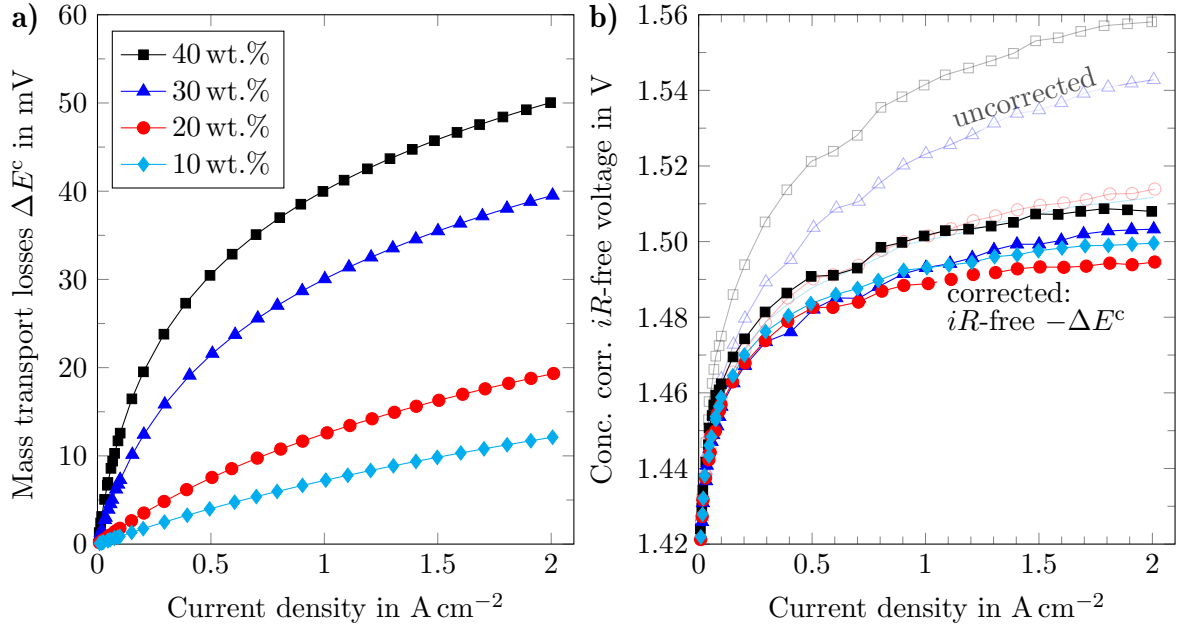


Figure 5.6: Subfigure a) shows the concentration overpotentials/mass transport losses calculated by Eq. (5.1) and b) shows the iR -free cell voltage corrected by the concentration overpotentials plotted against current density. The transparent curves with hollow marks of b) are the original/uncorrected iR -free curves of Fig. 5.5c).

5.3.3 Mass Transport free Tafel Analysis

The investigation of reaction kinetic parameters for the sluggish OER is an important investigation of PEM water electrolysis cells [23, 37, 73]. For this purpose, the Tafel equation (5.2) is fitted to the iR -free cell voltage at low current densities (in this work: 0.01 to 0.1 $A\ cm^{-2}$). For this low current density range it is assumed that all other losses i) mass transport losses, ii) ohmic losses within the catalyst layer and iii) the activation losses of the fast HER can be neglected. Consequently, the increase of the iR -free cell voltage at low current densities is only caused by the anodic activation overpotentials.

$$\eta_{act} = b \log \left(\frac{i}{i_0} \right) \quad (5.2)$$

The results of this Tafel analysis are shown in Fig. 5.7 as dashed lines for each CCM and the corresponding Tafel slopes are shown in the text boxes of Fig. 5.7. For the common iR -free cell voltage curves (not corrected by the shift in cathodic half-cell potential) the results are shown in Fig. 5.7a). The CCMs with low ionomer contents reveal Tafel slopes of 36 – 37 $mVdec^{-1}$, whereas the CCMs with 30 and 40 wt.% show significantly higher Tafel slopes of 43 and 47 $mVdec^{-1}$, respectively. Within literature both Tafel slopes are reported: Mazur et al. [72] measured Tafel slopes of 38.9 $mVdec^{-1}$ for IrO_2 and 34.6 – 49.5 $mVdec^{-1}$ for IrO_2 supported by TiO_2 by using the thin-film method on a

glassy carbon rotating disk electrode in 0.5 M H₂SO₄ at room temperature and Bernt and Gasteiger [23] measured Tafel slopes within an electrolysis cell of 45 – 47 mVdec⁻¹ also for a TiO₂ supported IrO₂ anode catalyst.

Beside the different cathode catalyst layers with varied ionomer contents, identical anode catalyst layers, porous transport layers as well as membranes are used. Consequently, the different Tafel slopes can only be caused by the different cathodic catalyst layers. Since the Pt loading was also identical, the difference has to come from the concentration overpotentials. Consequently, the previously mentioned assumptions (negligible other losses in the low current density range) are not fulfilled for the Tafel analysis. Hence, the different cathodic ionomer contents affect also the cell performance at low current densities, which could be erroneously mapped with the Tafel analyses on the sluggish OER. Therefore, the Tafel analysis is also performed for the concentration corrected *iR*-free cell voltage. This analysis is shown in Fig. 5.7b). The Tafel slopes of each CCM are reduced to values around 36 mVdec⁻¹ and agree now very well to each. Consequently, the mass transport losses due to hydrogen supersaturation can also affect the low current density range of 0.01 till 0.1 A cm⁻² and hence affect the Tafel analysis.

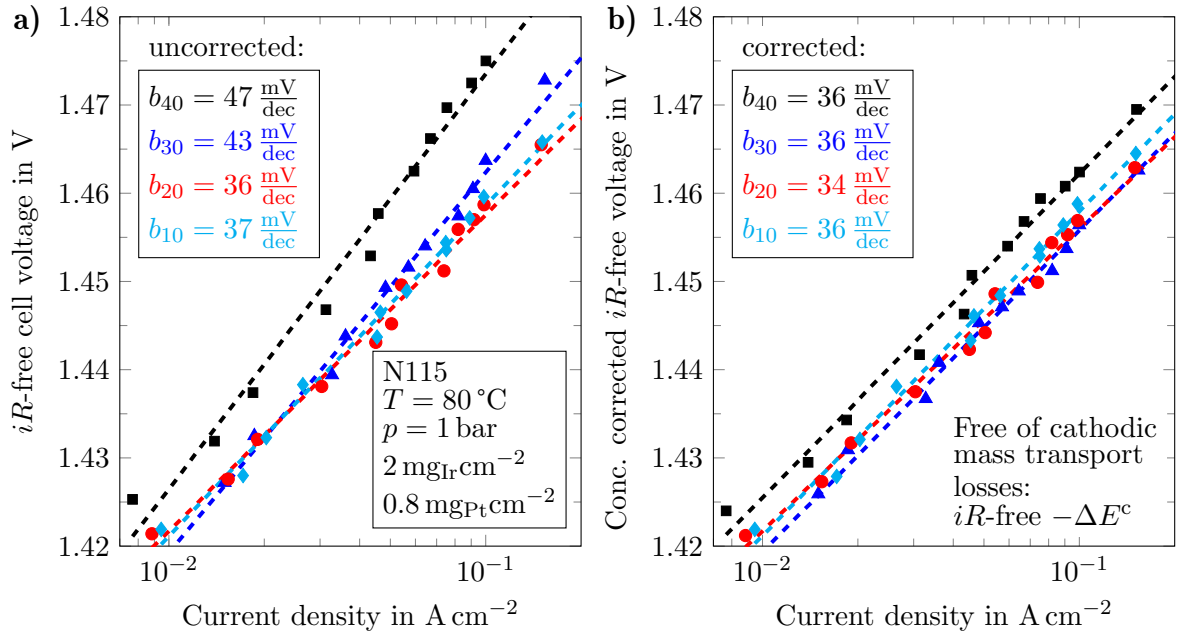


Figure 5.7: Comparison of the Tafel analysis with a) common *iR*-free cell voltage curves (uncorrected) and b) concentration corrected *iR*-free cell voltage curves. The dashed lines are the fitted results of the Tafel analysis, the corresponding Tafel slopes are given in the text boxes. The Tafel analysis is more homogeneous when the *iR*-free cell voltage is also reduced by the cathode mass transport losses.

5.4 Concluding Remarks

The previously shown effects of the cathode ionomer content on hydrogen crossover and cell voltage are summarized in Fig. 5.8. Therefore, all important values are plotted versus the cathode ionomer content for 3 different current densities. Fig. 5.8a) shows the reduction of the determined mass transfer coefficient with increasing ionomer content. This was mainly explained by i) increases in the average ionomer path way from catalyst towards pore space and ii) reduction in volume specific surface of the ionomer. A reduction of the mass transfer coefficient means an increase in mass transfer resistances. Consequently, the dissolved hydrogen concentration increases with ionomer content (Fig. 5.8b)). These supersaturated dissolved hydrogen concentrations negatively affect the hydrogen crossover (Fig. 5.8c)) and cell voltage (Fig. 5.8d)). The crossover increases due to higher concentration gradients (Fick's law) and the cell voltage increases because of the higher cathode half-cell potential (Nernst equation, increased mass transport losses).

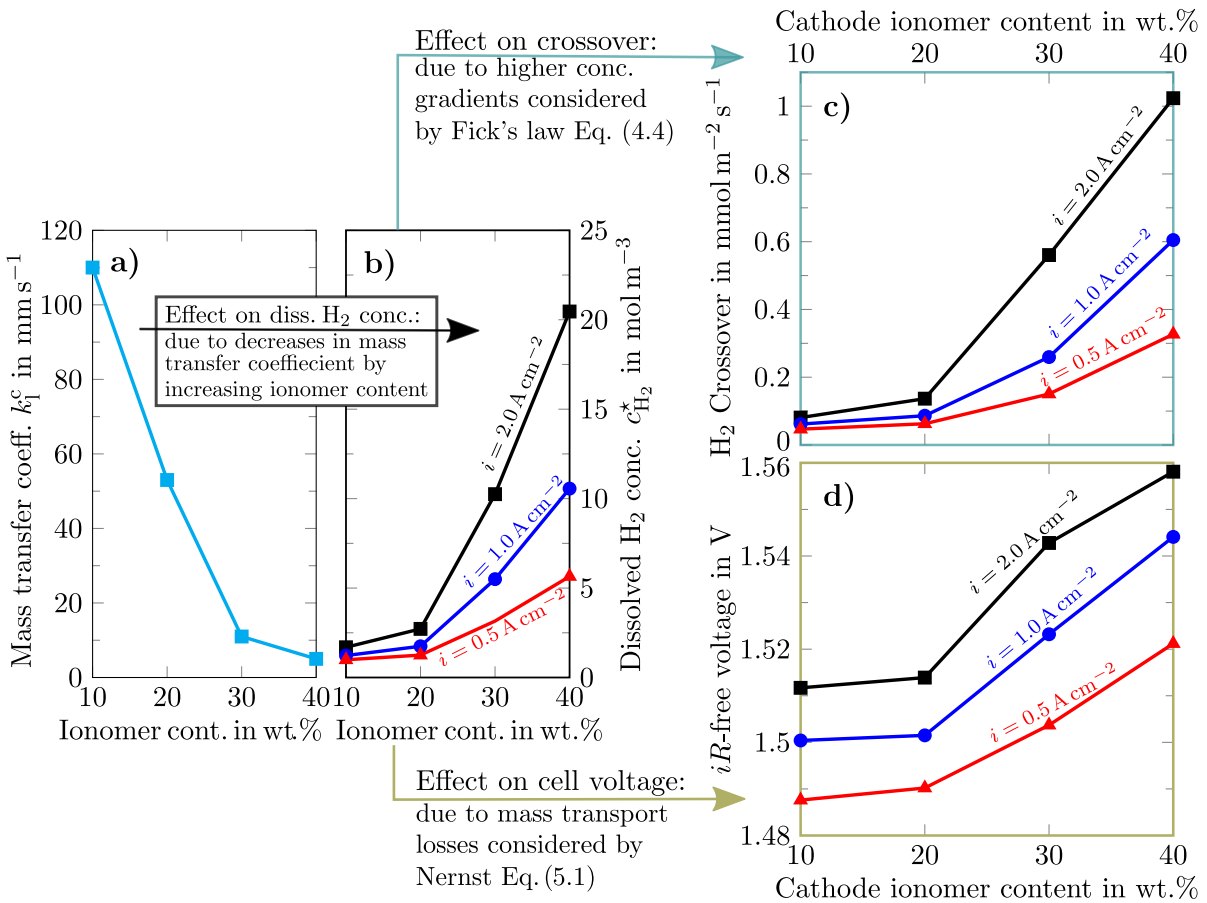


Figure 5.8: Effect of mass transfer resistances on hydrogen crossover and cell voltage by variation of the cathode ionomer content. A reduced mass transfer coef. a) leads to supersaturated dissolved hydrogen concentrations b) that cause increases in hydrogen crossover fluxes c) and cell voltages d).

For the observed range of the cathode ionomer content (10 to 40 wt.%), the crossover and cell voltage increase with increasing ionomer content. Bernt and Gasteiger [23] varied the ionomer content of the PEM water electrolyzer anode. With regard to cell voltage, they show similar results in comparison to this work. The iR -free cell voltage increases with increasing anode ionomer contents in the range of 11.6 to 28 wt.%. Considering the above presented findings this might be due to the increased supersaturation of dissolved oxygen, because of higher mass transfer resistances and thus increased anode half-cell potential. However, on the anode side also the transport of water could be hindered by increased ionomer contents. Consequently, the experimental findings of Bernt and Gasteiger [23] can be supported by the presented data. However, the authors also show that the iR -free cell voltage increases again at very low ionomer contents. They explained this by higher proton resistances within the catalyst layer with less ionomer and consequently higher voltage losses at very low ionomer contents. The optimal ionomer content for their anode catalyst layers was at 11.6 wt.% ionomer. This agrees very good with the trend of this work, in which the optimal ionomer might be close to 10 wt.%. However, the presented findings should be understood as qualitative results that show the correlation between mass transport resistances and crossover as well as cell voltage.

The fact that the cell voltage increases again at low ionomer contents, because of increased proton transport resistances [23], might originate from a shift of the reaction front towards the membrane. This could lead to higher supersaturation concentrations directly at the membrane/catalyst layer interface. Consequently, it can be assumed that also the gas crossover could increase again with decreasing ionomer contents.

These findings highlight the importance of the catalyst layer structure. Not only in the context of electrochemical activity, but also related to a reduction of mass transfer resistances, which reduce the supersaturation and thus improve the cell performance as well as decrease the crossover. The ionomer content is one key parameter, but there are several others, e. g. catalyst loading, which could also be changed to reduce the electrode mass transfer resistance of catalyst layers. It is important to investigate the different mass transport/transfer steps in more detail for systematic development of improved catalyst layers.

Additionally, the iR -free cell voltage is often used to obtain kinetic parameters of the anode (Tafel analysis). However, these obtained kinetic parameters might be still affected by mass transport losses, which can be caused due to supersaturated dissolved gas concentrations. Even if the Tafel analysis is carried out at low current densities, there are small changes in the half-cell potentials, which should be subtracted. Otherwise, the determined kinetic parameters are not free of mass transport effects. These mass transport voltage losses can be obtained by the measurement of gas crossover. Consequently, this can be used to determine mass transport losses and contribute to a comprehensive overview of overpotential sources.

6 Model Formulation and Validation

Within the previous chapters experimental data are shown and discussed concerning the effect of operating conditions (ch. 4) and ionomer content (ch. 5) on the current density dependent gas crossover. The most promising explanation of the experimental finding is the theory of supersaturated dissolved gas concentrations due to mass transfer limitations within the aqueous phase of the ionomer. Additionally, this theory can also explain the relation between gas crossover and mass transport losses (s. ch. 5). However, in section 4.2 a simple model is used to discuss the crossover increase with current density, but not the connection of gas crossover and mass transport losses. In context of the fifth research question a comprehensive, one-dimensional model is formulated and validated within this chapter to investigate and explain the experimental findings in more detail.

Research Question 5: *“How can the current density influence on gas crossover be described adequately by a physically meaningful model? How can the developed model help to analyze the observed effects in more detail?”*

For the one-dimensional model in through plane direction, a common five layer PEM water electrolysis cell setup of anode porous transport layer (aPTL), anode catalyst layer (aCL), membrane (mem), cathode catalyst layer (cCL) and cathode porous transport layer (cPTL) is considered. A sketch of these 5 layers is shown in Fig. 6.1. For the discretization of the ordinary differential equations the finite volume method is used. The resulting steady state model is implemented in *MATLAB* (The MathWorks) and numerically solved with the nonlinear algebraic equation solver: *fsolve*.

The model is described within the following sections. In the first three sections the model formulation for the description of the potential, concentration and temperature fields is introduced. These sections include the description of all balance equations, transport kinetics with its phenomenological coefficients, important supporting equations and boundary conditions. Less important equations, e.g. temperature and pressure dependencies are listed within the appendix. Within the fourth section the base case parameter set with the applied literature values is given. Subsequently, the integral model results according to the base case parameter set are validated by experimental data in section 6.5. Additionally, the most important local profiles are shown and discussed. Finally, this chapter ends with concluding remarks on the model and the model results.

6.1 Potential Fields

Fig. 6.1 schematically shows local profiles of the electric potential in the electron conducting phase and the proton potential in the proton conducting phase. The electric potential is calculated for all five layers, whereas the proton potential is only considered

for the membrane and both catalyst layers, since only these layers contain the proton conducting ionomer. Consequently, there is no proton potential within both PTLs.

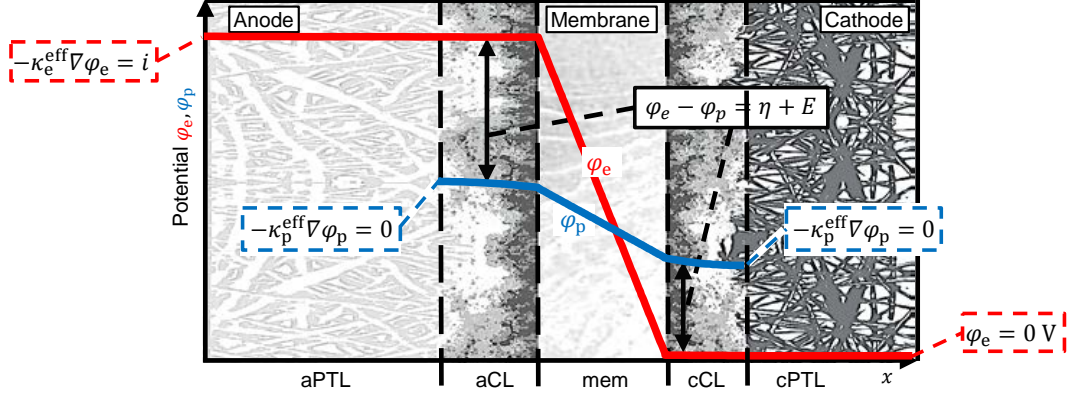


Figure 6.1: Sketch of a common 5 layer PEM water electrolysis cell with local profiles of the electron and proton potential. The boundary conditions are given within the dashed boxes.

Balance Equations Charge balances for electrons and protons are given in Eqs. (6.1) and (6.2). The transport of electrons and protons is described by Ohm's law.

$$0 = \nabla \left(-\kappa_e^{\text{eff}} \nabla \varphi_e \right) + \sigma_{\text{BV}} \quad (6.1)$$

$$0 = \nabla \left(-\kappa_p^{\text{eff}} \nabla \varphi_p \right) + \sigma_{\text{BV}} \quad (6.2)$$

Herein κ_e^{eff} is the effective electric conductivity, φ_e the electron potential, φ_p the proton potential and κ_p^{eff} the effective proton conductivity. The latter is considered to be a function of temperature T and water content λ of the ionomer. These dependencies are accounted for by use of the correlation of Springer et al. [131] (s. Eq. (A.1)) for the proton conductivity κ_p . This is corrected by the Bruggeman approach [84, 132] to obtain the effective proton conductivity κ_p^{eff} :

$$\kappa_p^{\text{eff}} = \frac{\varepsilon_{\text{ion}}}{\tau_{\text{ion}}} \kappa_p(T, \lambda) \quad (6.3)$$

where ε_{ion} is the volume fraction of the ionomer and τ_{ion} its tortuosity.

Source Term Protons and electrons are only produced/consumed in the catalyst layers. The corresponding source term σ_{BV} is described by a Butler-Volmer approach:

$$\sigma_{\text{BV}} = i_0(T) a_{\text{cat}} \left[\exp \left(\frac{\alpha_{\text{ox}} F}{RT} \eta_{\text{act}} \right) - \exp \left(-\frac{\alpha_{\text{red}} F}{RT} \eta_{\text{act}} \right) \right] \quad (6.4)$$

The temperature dependence of the exchange current density i_0 is considered by the Arrhenius equation (Eq. (A.2)). The volume specific surface of the catalyst layer a_{cat} is a structure dependent parameter (Eq. (A.3)). Furthermore, α_{ox} and α_{red} are the

charge transfer coefficients for the oxidation and reduction reactions of each half-cell. The activation overpotential η_{act} of each half-cell reaction is defined via Eq. (6.5) as the electric potential φ_e subtracted by the proton potential φ_p and the half-cell potential E .

$$\eta_{\text{act}} = \varphi_e - \varphi_p - E \quad (6.5)$$

The half-cell potentials $E^{a/c}$ of the anode and cathode catalyst layers are calculated by the Nernst equation (6.6) and (6.7). The anode half-cell potential is a function of the water concentration within the ionomer and the dissolved oxygen concentration within the water of the ionomer, whereas the cathode half-cell potential is a function of the dissolved hydrogen concentration within the water of the ionomer. These concentrations are described in the following section 6.2. The corresponding concentrations according to standard conditions are calculated by Eqs. (A.6) and (A.11). The temperature dependence of the reversible cell potential at standard conditions is set on the anode (Eq. (A.4)), since the cathodic standard half-cell potential is per definition 0 V [133].

$$E^a = E^0(T) + \frac{RT}{2F} \ln \left(\frac{c_{\text{dsw}}^0}{c_{\text{dsw}}} \sqrt{\frac{c_{\text{dsg},\text{O}_2}}{c_{\text{dsg},\text{O}_2}^0}} \right) \quad (6.6)$$

$$E^c = 0 \text{ V} + \frac{RT}{2F} \ln \left(\frac{c_{\text{dsg},\text{H}_2}}{c_{\text{dsg},\text{H}_2}^0} \right) \quad (6.7)$$

Boundary Conditions Boundary conditions of the charge balances are given in the dashed boxes of Fig. 6.1. At the anodic channel/PTL interface the electric current density is set to the applied current density i and at the cathodic PTL/channel interface the electric potential is grounded to 0 V.

For the proton charge balance homogeneous Neumann boundary conditions are used. The proton current density at both PTL/CL interfaces is 0, since no ionomer is within the PTLs. This is depicted by the flattening of the proton potential profile towards these boundaries.

6.2 Concentration Fields

Mass balances are considered for the three species: hydrogen, oxygen and water. These species exist in dissolved, liquid and gaseous phases. In section 6.2.1 the dissolved hydrogen and oxygen within water of the ionomer is described. The water uptake of the ionomer is depicted in section 6.2.2. Liquid water and gaseous hydrogen, oxygen as well as water vapor are considered in the pore space, which is discussed in section 6.2.3.

6.2.1 Dissolved Gases

The local concentration profiles of dissolved gases (hydrogen and oxygen) are shown in Fig. 6.2. The concentration of dissolved gases c_{dsg} are stated by the indices dsg to

highlight the differences to the gas concentration of the pore space. This dissolved gas concentrations within the water of the ionomer are calculated for the membrane and both catalyst layers, since no ionomer is within both PTLs. Additionally, the saturated concentrations are shown in Fig. 6.2 as dotted lines. It can be seen that the actual dissolved gas concentrations of hydrogen and oxygen are higher than the saturation concentrations. This supersaturation is the driving force for the transfer of dissolved gas into the gas phase. Furthermore, the hydrogen and oxygen crossover, that are driven by the dissolved gas concentration gradients across the membrane, are implied in Fig. 6.2. The spatially resolved modeling of dissolved gases in PEM water electrolyzers is very rare [134], but it is one of the key features of this model. Consequently, the parameters of the source terms are described in more detail in comparison to the other balance equations.

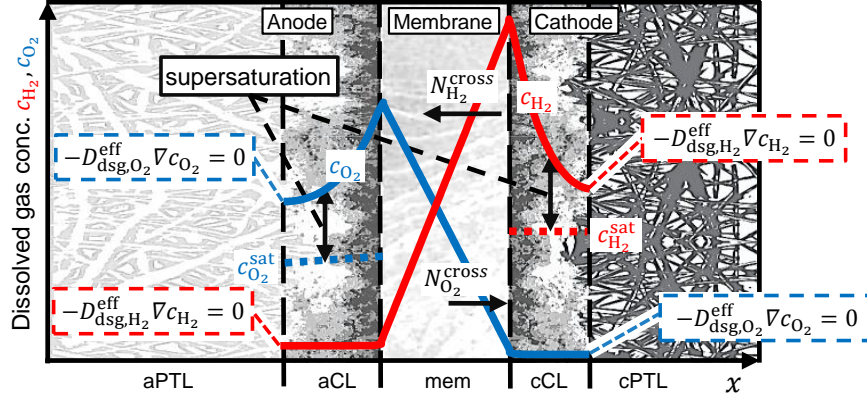


Figure 6.2: Schematic local dissolved gas concentration profiles. The boundary conditions of each balance equation are given within the dashed boxes.

Balance Equations The transport of dissolved hydrogen and oxygen is considered by Fick's first law [13, 66, 86]. The mass balances of dissolved gases (6.8) in concentration form can be seen below:

$$0 = \nabla \left(-D_{dsg,j}^{eff} \nabla c_{dsg,j} \right) + \sigma_{dsg,j} \quad j: \text{H}_2 \text{ and } \text{O}_2 \quad (6.8)$$

where $D_{dsg,j}^{eff}$ is the effective diffusion coefficient of dissolved gas. The index j stands for hydrogen and oxygen, respectively. The effective diffusion coefficient is calculated by accounting the Bruggeman approach [86]:

$$D_{dsg,j}^{eff} = \frac{\varepsilon_{ion} \varepsilon_{H_2O}}{\tau_{ion}} D_{dsg,j}(T) \quad (6.9)$$

where ε_{ion} is the ionomer content of the respective layers, ε_{H_2O} the water fraction within the ionomer, τ_{H_2O} the tortuosity of the water channels and $D_{dsg,j}$ the diffusion coefficient of the respective dissolved gas within pure water. The temperature dependencies of these diffusion coefficients are considered by the Arrhenius equation (s. Eq. (A.5)).

Source Term The source terms of the dissolved gas mass balances $\sigma_{\text{dsg},j}$ are given in Eq. (6.10).

$$\sigma_{\text{dsg},j} = \sigma_{\text{dsg},j}^{\text{evo}} - \sigma_{\text{dsg},j}^{\text{mtf}} + \sigma_{\text{dsg},j}^{\text{recomb}} \quad (6.10)$$

The first term stands for the evolution of dissolved gas $\sigma_{\text{dsg},j}^{\text{evo}}$ that can be calculated by Faraday's laws of electrolysis, which is given in Eq. (6.11). Within this equation z_j is the number of transferred electrons per evolved gas molecule. On the anode side z_{O_2} is 4 and on the cathode side z_{H_2} is equal to 2.

$$\sigma_{\text{dsg},j}^{\text{evo}} = \frac{|\sigma_{\text{BV}}|}{z_j F} \quad (6.11)$$

It is assumed that the gases evolve in dissolved form and have to be transferred from the dissolved state into the gas phase, which is expressed by the second source term $\sigma_{\text{dsg},j}^{\text{mtf}}$ of Eq. (6.10).

$$\sigma_{\text{dsg},j}^{\text{mtf}} = k_{1,j} a_{\text{ion}} (c_{\text{dsg},j} - c_{\text{dsg},j}^{\text{sat}}) \quad (6.12)$$

Where $c_{\text{dsg},j}$ is the actual dissolved gas concentration and $c_{\text{dsg}}^{\text{sat}}$ the saturated dissolved gas concentration, which is calculated by Henry's law (Eq. (A.6)) as a function of partial gas pressure and solubility coefficient of the respective gas in water (Eq. (A.2)). The volume specific surface of the ionomer a_{ion} is estimated by Eq. (6.13).

$$a_{\text{ion}} \approx \frac{6\varepsilon_{\text{ion}}}{d_{\text{pore}}} \quad (6.13)$$

For the mass transfer coefficients $k_{1,j}$ of hydrogen and oxygen the film model is applied (Eq. (6.14)) [123]. By means of this approach the diffusion process of dissolved gas from the catalyst particles through the ionomer towards the ionomer/pore interface is considered by:

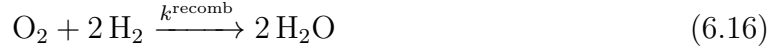
$$k_{1,j} = \frac{D_{\text{dsg},j}^{\text{eff}}}{\bar{\delta}_{\text{ion}}} \quad (6.14)$$

The mean ionomer path length $\bar{\delta}_{\text{ion}}$ from each catalyst particle towards the ionomer/pore interface was determined by Hegge et al. [129]. They analyzed the structure of a PEM water electrolysis anode catalyst layer by using focused ion beam (FIB) SEM tomography and aimed to investigate the effect of ionomer content on transport parameters. Therefore, different ionomer contents were modeled into the obtained catalyst structure. By filling the catalyst layer with ionomer the porosity of the pore space was reduced, while keeping the catalyst fraction constant. Additionally, Hegge et al. [129] observed that the mean ionomer path length $\bar{\delta}_{\text{ion}}$ increases with increasing ionomer content. This correlation is considered by Eq. (6.15), which was fitted to the data of Hegge et al. [129].

$$\bar{\delta}_{\text{ion}} = 5 \cdot 10^{-6} \text{ m} \exp \left[4.23 \left(\frac{\varepsilon_{\text{ion}}}{1 - \varepsilon_{\text{cat}}} - 1 \right) \right] \quad (6.15)$$

Finally, the last term in Eq. (6.10) represents the source term of recombination $\sigma_{\text{dsg},j}^{\text{recomb}}$.

It considers the recombination of oxygen and hydrogen to dissolved water within the ionomer:



For $\sigma_{\text{dsg},j}^{\text{recomb}}$ it follows:

$$\sigma_{\text{dsg},j}^{\text{recomb}} = \nu_{\text{dsg},j} k^{\text{recomb}} c_{\text{dsg},\text{O}_2} c_{\text{dsg},\text{H}_2}^2 \quad (6.17)$$

where $\nu_{\text{dsg},j}$ is the stoichiometric number and k^{recomb} the reaction rate constant of the recombination reaction, which is set to a very high value to satisfy the observation that the most part of permeated oxygen recombines at the Pt catalyst within the cathode catalyst layer.

Boundary Conditions Fig. 6.2 shows the boundary conditions for the mass balances of dissolved gases and the corresponding concentration profiles. For all boundaries homogeneous Neumann conditions are used. Thus, it is assumed that no diffusive fluxes of dissolved hydrogen and oxygen flow through the PTL/CL interfaces. This assumption is justified, since the diffusion coefficient of dissolved gas is much lower (4 orders of magnitude) than the diffusion coefficient of gases within the pore space. Consequently, the flux of dissolved gas can be neglected compared to the dissolved flux of gas within the pore space of the porous transport layers.

6.2.2 Dissolved Water Content

The concentration field of dissolved water (dsw) within the ionomer is given in the form of water content λ . The water content λ was chosen instead of the dissolved water concentration, since most literature correlations are formulated in that way, e. g. Springer equation for the proton conductivity [131].

A local profile is shown schematically in Fig. 6.3. The balance equation for the water content are only defined for the membrane and both catalyst layers, since only these layers contain ionomer. Within the anodic catalyst layer the dissolved water concentration in the ionomer can be below the saturation concentration, because of the consumption of water and the electro-osmotic drag. Whereas, in the cathode catalyst layer the water content can be higher as the saturation content.

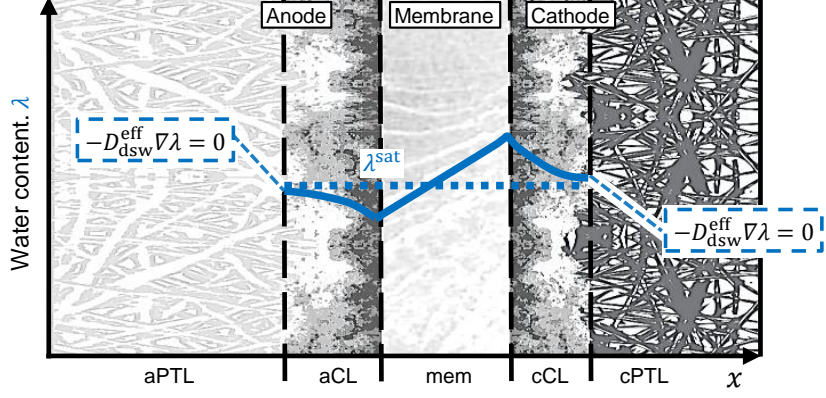


Figure 6.3: Schematic local concentration profiles of the dissolved water content. The boundary conditions of each balance equation are given within the dashed boxes.

Balance Equation Transport of dissolved water is considered by diffusion and electro-osmotic drag [13,91]. The mass balance equation is stated below:

$$0 = \nabla \left(-D_{\text{dsw}}^{\text{eff}} \nabla \lambda - \frac{n_{\text{drag}}}{F c_{\text{dsw}}} \kappa_{\text{p}}^{\text{eff}} \nabla \varphi_{\text{p}} \right) + \sigma_{\text{dsw}} \quad (6.18)$$

where $D_{\text{dsw}}^{\text{eff}}$ is the diffusion coefficient of dissolved water and n_{drag} is the electro-osmotic drag coefficient. Both are dependent on temperature and water content (s. Eq. (A.9) and (A.10)). The concentration of dissolved water c_{dsw} can be calculated by Eq. (A.11).

Source Term The source term σ_{dsw} of the dissolved water mass balance is given in Eq. (6.19). It considers three different processes: i) the electrochemical consumption (cons) of water (only for the anodic catalyst layer), ii) the sorption (sorp) of liquid water/desorption of dissolved water and iii) the dissolved water formation due to recombination within the cathode catalyst layer.

$$\sigma_{\text{dsw}} = -\sigma_{\text{dsw}}^{\text{cons}} + \sigma_{\text{dsw}}^{\text{sorp}} + \sigma_{\text{dsw}}^{\text{recomb}} \quad (6.19)$$

The consumption of water by the OER can be calculated by Faraday's law Eq. (6.11). Therefore, the source term of the charge balances σ_{BV} is used to calculate the local consumption rate of water $\sigma_{\text{dsw}}^{\text{cons}}$ within the anode catalyst layer:

$$\sigma_{\text{dsw}}^{\text{cons}} = \frac{\sigma_{\text{BV}}}{2F c_{\text{dsw}}} \quad (6.20)$$

The sorption of water/desorption of dissolved water is considered by Eq. (6.21):

$$\sigma_{\text{dsw}}^{\text{sorp}} = k^{\text{sorp}} a_{\text{ion}} (\lambda^{\text{sat}} - \lambda) \quad (6.21)$$

where λ^{sat} is the saturated water content of Nafion membranes, which are immersed in

liquid water [64], a_{ion} the volume specific ionomer surface (s. Eq. (6.13)) and k^{sorp} the sorption/desorption mass transfer coefficient [135], which are assumed to be equal in a first approximation [136].

The recombination source term of dissolved water $\sigma_{\text{dsw}}^{\text{recomb}}$ can be comparatively calculated to the dissolved gas recombination source terms (cf. Eq. (6.17)):

$$\sigma_{\text{dsw}}^{\text{recomb}} = k^{\text{recomb}} c_{\text{dsg},\text{O}_2} c_{\text{dsg},\text{H}_2}^2 \quad (6.22)$$

Boundary Conditions Fig. 6.3 shows schematically the profile of the ionomer water content. At the PTL/CL interfaces also homogeneous Neumann boundary conditions are set, since no ionomer exist within the PTLs. Consequently, there are no diffusive fluxes of dissolved water at these interfaces and no electro-osmotic drag is possible.

6.2.3 Gases and Liquid Water

The concentration fields of the three gaseous components hydrogen, oxygen and water vapor (vap) as well as liquid water are given in the pressure form. The total gas pressure p_g is the sum of all partial pressures $p_{g,j}$:

$$p_g = \sum p_{g,j} = p_{g,\text{H}_2} + p_{g,\text{O}_2} + p_{g,\text{vap}} \quad (6.23)$$

In Fig. 6.4 the profiles of total gas pressure and liquid pressure within all five layers are shown schematically.

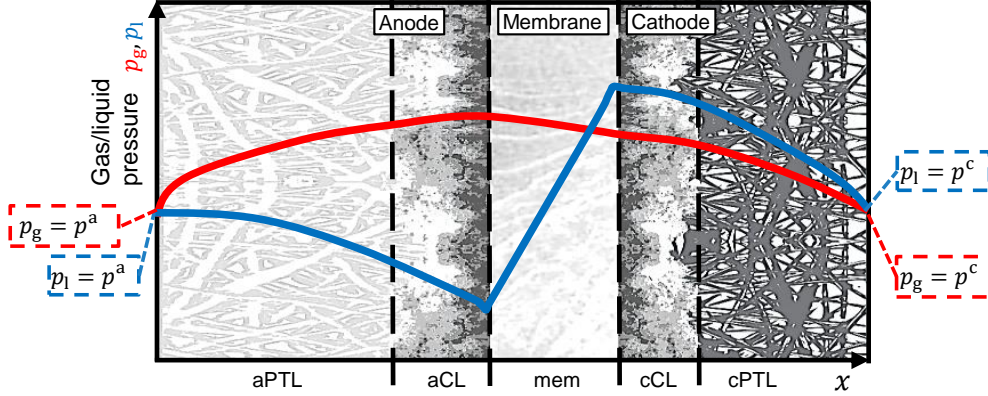


Figure 6.4: Schematic local concentration profiles of the total gas pressure as well as the liquid pressure. The boundary conditions of each balance equation are given within the dashed boxes.

Balance Equations In this work the two-phase flow is described by Darcy's law [137, 138]. Certainly, for the gas phase Darcy's law is expanded by Fickian diffusion [139]. The mass balances of the three gaseous components and liquid water are given in the following equations:

$$0 = \nabla \left(-D_{g,j}^{\text{eff}} \nabla c_{g,j} + c_{g,j} \frac{K_{\text{hyd}} k_g^{\text{rel}}}{\mu_g} \nabla p_g \right) + \sigma_{g,j} \quad j: \text{H}_2, \text{O}_2 \text{ and vap} \quad (6.24)$$

$$0 = \nabla \left(\phantom{-D_{g,j}^{\text{eff}} \nabla c_{g,j}} + c_1 \frac{K_{\text{hyd}} k_1^{\text{rel}}}{\mu_1} \nabla p_1 \right) + \sigma_1 \quad (6.25)$$

where $c_{g,j}$, c_1 stand for the gas and liquid concentrations and μ_g , μ_1 are the gaseous and liquid dynamic viscosities (Eqs. (A.12) – (A.17)).

Gas diffusion in porous media is considered by free diffusion (interactions only between gas molecules) and Knudsen diffusion (interactions with the solid structure) [139]. The diffusion coefficients for the free diffusion $D_{g,j}^{\text{free}}$ are calculated by the Chapman-Enskog theory and further correction equations (Eqs. (A.18) – (A.19)). The Knudsen diffusion coefficients $D_{g,j}^{\text{Kn}}$ are calculated by Eq. (A.20).

The effective diffusion coefficient for gas transport is calculated by the Bosanquet formula:

$$D_{g,j}^{\text{eff}} = \left(\frac{1}{D_{g,j}^{\text{free}}} + \frac{1}{D_{g,j}^{\text{Kn}}} \right)^{-1} \quad (6.26)$$

Darcy's law describes the hydraulic transport of gases and liquid water through porous media. The phenomenological coefficient of this pressure driven transport is the hydraulic permeability K_{hyd} that is a structure depending parameter, which can be calculated by the Hagen–Poiseuille equation [92]:

$$K_{\text{hyd}} = \frac{\varepsilon_{\text{pore}} d_{\text{pore}}^2}{32\tau_{\text{pore}}} \quad (6.27)$$

where $\varepsilon_{\text{pore}}$ is the porosity, d_{pore} the pore diameter of the pore space and τ_{pore} the tortuosity. The relative gas and liquid permeabilities k_g^{rel} and k_1^{rel} are dependent on the saturation level. Therefore, Willey's cubic law [103, 104] is used (Eq. (A.21) and (A.22)).

The relation between gas pressure p_g and liquid pressure p_1 within porous media is given by the definition of capillary pressure p_c :

$$p_c = p_g - p_1 \quad (6.28)$$

where this capillary pressure is calculated by Eq. (A.23). The correlation of the pore saturation and capillary pressure is considered by the Leverett function J (Eq. (A.24)) [140]. In this work the mixed wettability approach from Grötsch et al. [137] was adopted.

Source Term The gas source terms $\sigma_{g,j}$ represent the amount of gas molecules that enters the gaseous phase. For oxygen and hydrogen it is equal to the mass transfer source term $\sigma_{\text{dsg}}^{\text{mtf}}$ (formulated in Eq. (6.12)):

$$\sigma_{g,j} = \sigma_{\text{dsg},j}^{\text{mtf}}, \quad j: \text{H}_2, \text{O}_2 \quad (6.29)$$

and the source term for water vapor considers vaporization of liquid water:

$$\sigma_{g,vap} = \frac{k_{vap} a_{pore}}{RT} (p_{vap}^{sat} - p_{vap}) \quad (6.30)$$

herein k_{vap} is the vaporization/condensation transfer coefficient, which is calculated by the dimensionless Sherwood number Eq. (A.27) and p_{vap}^{sat} is the saturated vapor pressure, which is considered by the Antoine equation Eq. (A.26).

The source term σ_1 of the liquid water mass balance can be calculated by Eq. (6.31) and is equal to the amount of water, which vaporizes/condensates, and absorbs/desorbs by the ionomer.

$$\sigma_1 = -\sigma_{g,vap} - \sigma_{dsw}^{sorp} \quad (6.31)$$

Boundary Conditions In Fig. 6.4 the boundary conditions of the gas and liquid mass balances are indicated. At the channel/PTL interfaces only Dirichlet boundary conditions are set. In sum the total gas pressure and liquid pressure are equal to the predefined anode and cathode operating pressures $p^{a/c}$. However, since the gas phase consists of three components, for each component separate boundary conditions are required. For the anode channel/PTL boundary interface the following three boundary conditions are set:

$$p_{g,vap}^a = p_{vap}^{sat}(T_{cell}) \quad (6.32)$$

$$p_{g,H_2}^a = y_{H_2}^{a,dry} (p^a - p_{vap}^a) \quad (6.33)$$

$$p_{g,O_2}^a = p^a - p_{g,vap}^a - p_{g,H_2}^a \quad (6.34)$$

Water vapor pressure at the boundary is set to the saturation vapor pressure, which is calculated by Eq. (A.26) depending on the predefined cell temperature. Consequently, it is assumed that the gases are saturated at the channel boundaries. The hydrogen partial pressure at the anode channel/PTL interface is the product of the dry gas pressure and the dry hydrogen content $y_{H_2}^{a,dry}$. The latter is calculated via the balance equation of the anode:

$$y_{H_2}^{a,dry} = \frac{N_{H_2}^{cross}}{N_{H_2}^{cross} + N_{O_2}^{evo} - N_{O_2}^{cross}} \quad (6.35)$$

where, $N_{H_2}^{cross}$ and $N_{O_2}^{cross}$ are the crossover fluxes of hydrogen and oxygen and $N_{O_2}^{evo}$ the evolution flux of oxygen. The remaining partial pressure of oxygen at the anode boundary can be calculated by subtracting the hydrogen and water vapor pressure from the anode pressure p^a .

The boundary conditions of the cathode PTL/channel interface are set to:

$$p_{g,vap}^c = p_{vap}^{sat}(T_{cell}) \quad (6.36)$$

$$p_{g,O_2}^c = 0 \text{ bar} \quad (6.37)$$

$$p_{g,H_2}^c = p^c - p_{g,vap}^c - p_{g,O_2}^c \quad (6.38)$$

herein, the vapor pressure is assumed to be equal to the saturation vapor pressure. The oxygen partial pressure of the cathode is set to 0, since it is assumed that all permeating oxygen recombines with hydrogen within the cathode catalyst layer. The hydrogen partial pressure at the cathode boundary can be calculated by subtracting the oxygen and vapor pressure from the cathode pressure p^c .

6.3 Temperature Field

Fig. 6.5 shows schematically the local temperature profile for all five layers.

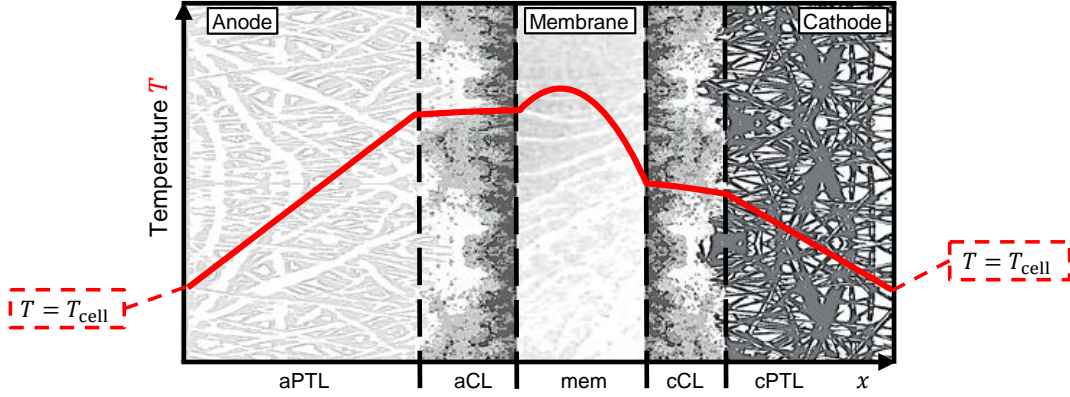


Figure 6.5: Schematic local temperature profile. The boundary conditions are stated within the dashed boxes.

Balance Equation Within the heat balance Eq. (6.39) heat transport is described by Fourier's law:

$$0 = \nabla \cdot (-\lambda_T^{\text{eff}} \nabla T) + \sigma_T \quad (6.39)$$

where λ_T^{eff} is the effective thermal conductivity in each of the specific layer.

Source Term For the source term σ_T the following five different effects are considered:

$$\sigma_T = \sigma_T^{\text{joule}} + \sigma_T^{\text{vap}} + \sigma_T^{\text{act}} + \sigma_T^{\text{entr}} + \sigma_T^{\text{recomb}} \quad (6.40)$$

where these source/sink terms are stated in equations (6.41) – (6.45) and correspond to the following five different processes: i) Joules heating by electric (all layers) and protonic current (within membrane and catalyst layers), ii) the heat for vaporization and condensation (all layers except for the membrane), iii) the reversible heat due to entropy changes (only anode catalyst layer), iv) irreversible heating due to the activation losses (only catalyst layers) and v) the heat of the recombination reaction of permeated oxygen with hydrogen to water within the cathode catalyst layer.

$$\sigma_T^{\text{joule}} = \kappa_e^{\text{eff}} \nabla^2 \varphi_e + \kappa_p^{\text{eff}} \nabla^2 \varphi_p \quad (6.41)$$

$$\sigma_T^{\text{vap}} = \sigma_{g,\text{vap}} \Delta H^{\text{vap}} \quad (6.42)$$

$$\sigma_T^{\text{act}} = \sigma_{\text{BV}} \eta_{\text{act}} \quad (6.43)$$

$$\sigma_T^{\text{entr}} = \frac{\sigma_{\text{BV}}}{4F} T \Delta S \quad (6.44)$$

$$\sigma_T^{\text{recomb}} = \sigma_{\text{dsw}}^{\text{recomb}} \Delta H^{\text{recomb}} \quad (6.45)$$

Within the previous equations ΔH^{vap} is the enthalpy of vaporization, ΔS the entropy change and ΔH^{recomb} the enthalpy of the recombination reaction (Eqs. (A.28) – (A.30)).

Boundary Conditions The boundary conditions of the energy balance and the local temperature profile are shown in Fig. 6.5. The temperature at the channel/PTL interfaces is set to the specified operating temperature. This Dirichlet boundary conditions correspond to cell setups, in which the temperature of the end plates/flow fields are controlled isothermally, e. g. with a liquid cooling/heating system [18, 141], or peltier elements [24].

6.4 Base Case Parameter Set

For the previously formulated model it is necessary to specify the operating conditions, which are used as boundary conditions in the model. The following operating conditions were defined for the base case:

- cell temperature of 80 °C
- anode pressure of 1 bar
- cathode pressure of 1 bar
- current density in a range of 0.01 – 3 A cm⁻²

In addition to the operating conditions, the model requires a high number of different parameters. In Tab. 6.1 all base case parameters are given. The parameters were listed in 4 different categories, namely: a) structural and geometrical parameters, b) physical parameters, c) reaction kinetic parameters and d) transport kinetic parameters. Most parameters are dependent of temperature, pressure, membrane water content or structure. For these dependencies the corresponding equations are indicated, which are mainly given within the appendix A.

Table 6.1: Base case parameter set of the formulated model.

a) Structural and geometrical parameters:					
Parameter / Symbol / Units	aPTL	aCL	mem	cCL	cPTL
Material / - / -	Ti	IrO ₂	Nafion	Pt/C	Carbon
Layer thickness / δ / μm	1000	δ^{aCL} ^a	127 ^b (N115)	δ^{cCL} ^a	370 [142]
Catalyst loading / L_{cat} / mg cm^{-2}	-	2 ^c	-	1 ^c	-
Cat. particle diameter / d_{cat} / nm	-	8 [143]	-	5 [144]	-
Catalyst density / ρ_{cat} / kg m^{-3}	-	$1 \cdot 10^4$ [22]	-	$9.2 \cdot 10^3$ [22]	-
Catalyst fraction / ε_{cat} / -	-	0.45 [129]	-	0.45 ^d	-
Ionomer fraction / ε_{ion} / -	-	0.2 ^c	1	0.2 ^c	-
Ion. tortuosity / τ_{ion} / -	-	$\varepsilon_{\text{ion}}^{-0.5}$ [144]	1.5 [84]	$\varepsilon_{\text{ion}}^{-0.5}$ [144]	-
Pore fraction / $\varepsilon_{\text{pore}}$ / -	0.3 [37]	$\varepsilon_{\text{pore}}^{\text{CL}}$ ^e	0.39 [145]	$\varepsilon_{\text{pore}}^{\text{CL}}$ ^e	0.62 [38]
Pore diameter / d_{pore} / μm	57 [37]	0.1 [144]	$2.8 \cdot 10^{-3}$ [145]	0.1 [144]	17.2 [38]
Pore tortuosity / τ_{pore} / -	1.8 [37]	$\varepsilon_{\text{pore}}^{-0.5}$ [144]	2 [145]	$\varepsilon_{\text{pore}}^{-0.5}$ [144]	2.5 [38]
Hydrophilic fraction / f_1 / -	1 ^c	0.3 [146]	1 ^c	0.3 [146]	0.6 [146]
b) Physical parameters:					
Solub. coef. / $S_{g,j}$ / $\text{mol Pa}^{-1} \text{m}^{-3}$	Eq. (A.2)	Eq. (A.2)	Eq. (A.2)	Eq. (A.2)	Eq. (A.2)
Sat. water content / λ^{sat} / -	-	20 [64]	20 [64]	20 [64]	-
Water frac. within ion. / $\varepsilon_{\text{H}_2\text{O}}$ / -	-	Eq. (A.8)	Eq. (A.8)	Eq. (A.8)	-
Dyn. gas viscosity / μ_g / Pa s	Eq. (A.16)	Eq. (A.16)	Eq. (A.16)	Eq. (A.16)	Eq. (A.16)
Dyn. liquid viscosity / μ_l / Pa s	Eq. (A.17)	Eq. (A.17)	Eq. (A.17)	Eq. (A.17)	Eq. (A.17)
Contact angle / θ_1 / $^\circ$	70 [90]	80 [146]	65 [147]	80 [146]	45 [146]
Contact angle / θ_2 / $^\circ$	-	100 [146]	-	100 [146]	110 [146]
Capillary pressure / p_c / Pa	Eq. (A.23)	Eq. (A.23)	Eq. (A.23)	Eq. (A.23)	Eq. (A.23)
Surface tension / γ / N m^{-1}	Eq. (A.25)	Eq. (A.25)	Eq. (A.25)	Eq. (A.25)	Eq. (A.25)
Sat. vapor pressure / $p_{\text{vap}}^{\text{sat}}$ / Pa	Eq. (A.26)	Eq. (A.26)	Eq. (A.26)	Eq. (A.26)	Eq. (A.26)
Heat of vap. / ΔH_{vap} / J mol^{-1}	Eq. (A.29)	Eq. (A.29)	Eq. (A.29)	Eq. (A.29)	Eq. (A.29)
Entropy change / ΔS / $\text{J mol}^{-1} \text{K}^{-1}$	-	Eq. (A.28)	-	-	-
c) Reaction kinetic parameters:					
Ref. exch. cur. dens. / i_0^{ref} / A m^{-2}	-	$3 \cdot 10^{-7}$ ^f	-	$7 \cdot 10^{-2}$ ^f	-
Activation energy / E_a / J mol^{-1}	-	$1.9 \cdot 10^4$ [148]	-	$1.9 \cdot 10^4$ [148]	-
Ox. charge transf. coef. / α_{ox} / -	-	1.5 ^c	-	2 ^c	-
Red. charge transf. coef. / α_{red} / -	-	1.5 ^c	-	2 ^c	-
Half-cell std. pot. / E^0 / V	-	Eq. (A.4)	-	0 [133]	-
Recomb. const. / k^{recomb} / $\text{m}^9 \text{s}^{-1} \text{mol}^{-3}$	-	-	-	$1 \cdot 10^7$ ^g	-
d) Transport kinetic parameters:					
Eff. electric cond. / κ_e^{eff} / S m^{-1}	$1 \cdot 10^6$ [37]	22.2 [22]	$2 \cdot 10^{-4}$ ^h	25 [22]	$1.3 \cdot 10^4$ [142]
Protonic cond. / κ_p / S m^{-1}	-	Eq. (A.1)	Eq. (A.1)	Eq. (A.1)	-
Dsg diff. coef. / $D_{\text{dsg},j}$ / $\text{m}^2 \text{s}^{-1}$	-	Eq. (A.5)	Eq. (A.5)	Eq. (A.5)	-
Mass transfer coef. / k_1 / m s^{-1}	-	Eq. (6.14)	-	Eq. (6.14)	-
Drag coef. / n_{drag} / -	-	Eq. (A.9)	Eq. (A.9)	Eq. (A.9)	-
Eff. dsw diff. coef. / $D_{\text{dsw}}^{\text{eff}}$ / $\text{m}^2 \text{s}^{-1}$	-	Eq. (A.10)	Eq. (A.10)	Eq. (A.10)	-
Sorp. trans. coef. / k^{sorp} / m s^{-1}	-	$2.6 \cdot 10^{-6}$ ⁱ	$2.6 \cdot 10^{-6}$ ⁱ	$2.6 \cdot 10^{-6}$ ⁱ	-
Free diff. coef. / $D_{g,j}^{\text{free}}$ / $\text{m}^2 \text{s}^{-1}$	Eq. (A.19)	Eq. (A.19)	Eq. (A.19)	Eq. (A.19)	Eq. (A.19)
Knudsen diff. coef. / $D_{g,j}^{\text{Kn}}$ / $\text{m}^2 \text{s}^{-1}$	Eq. (A.20)	Eq. (A.20)	Eq. (A.20)	Eq. (A.20)	Eq. (A.20)
Hyd. permeability / K_{hyd} / m^2	Eq. (6.27)	Eq. (6.27)	Eq. (6.27)	Eq. (6.27)	Eq. (6.27)
Rel. gas perm. coef. / k_g^{rel} / -	Eq. (A.21)	Eq. (A.21)	Eq. (A.21)	Eq. (A.21)	Eq. (A.21)
Rel. liquid perm. coef. / k_l^{rel} / -	Eq. (A.22)	Eq. (A.22)	Eq. (A.22)	Eq. (A.22)	Eq. (A.22)
Vap. transf. coef. / k^{sorp} / m s^{-1}	Eq. (A.27)	Eq. (A.27)	Eq. (A.27)	Eq. (A.27)	Eq. (A.27)
Thermal cond. λ_T^{eff} in $\text{W m}^{-1} \text{K}^{-1}$	10 [37]	0.87 [149]	0.45 [149]	0.87 [149]	1.7 [142]

^a $\delta^{\text{CL}} = L_{\text{cat}} \rho_{\text{cat}}^{-1} \varepsilon_{\text{cat}}^{-1}$, ^b dry thickness, ^c chosen, ^d according [129], ^e $\varepsilon_{\text{pore}}^{\text{CL}} = 1 - \varepsilon_{\text{ion}} - \varepsilon_{\text{cat}}$, ^f chosen according to [8],

^g estimated for a full recombination of permeated oxygen, ^h calculated by linear sweep voltammetry [96],

ⁱ for a N115 membrane at $T = 80^\circ \text{C}$ [135]

6.5 Model Base Case Results

In this section the results of the previously formulated model with the base case parameter set are described and compared to experimental results. The model results are divided into the subsection of integral cell behavior and local profiles.

6.5.1 Integral Cell Behavior

To evaluate the integral cell behavior the polarization curve, the hydrogen in oxygen content of the anode product gas and the hydrogen crossover are shown in Fig. 6.6. The experimental results of chapter 5 are additionally depicted to validate the model.

The comparison of the polarization behavior is shown in Fig. 6.6a). It can be seen that the simulation results obtained with the base case parameter set match the experimental data quite well without any optimizing or fitting of e. g. reaction kinetic or mass transport parameters. However compared to these experimental results, the literature based kinetic parameters are too good and the proton conductivity is too low.

Fig. 6.6b) shows the content of permeated hydrogen in oxygen within the anode outlet. The qualitative trend of the model results agrees very well with the experimental data. At very low current densities the H_2 in O_2 content is high, since the produced amount of oxygen is small. With increasing current density the evolved oxygen dilutes the amount of permeated hydrogen, consequently the hydrogen in oxygen content decreases with current density.

The corresponding hydrogen crossover is shown in Fig. 6.6c). It can be seen that the model results with the base parameter set is too low at small current densities, which is mainly influenced by the hydrogen diffusion and solubility coefficient. However, the literature based parameter set allows a comparable increase of the crossover with current density.

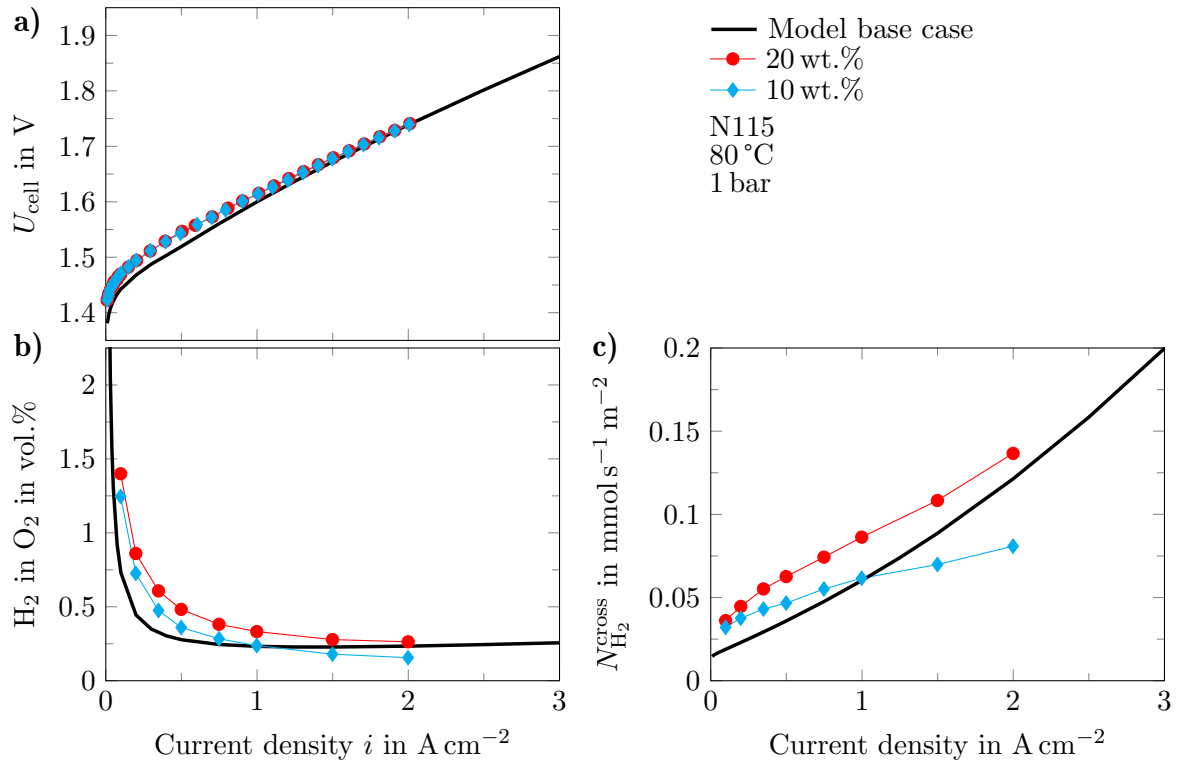


Figure 6.6: Comparison of integral model results and experimental data from the ionomer variation of chapter 5. Subfigure a) shows the polarization behavior, b) shows the H_2 in O_2 content and c) the hydrogen crossover versus current density. The simulations were carried out with the base case parameter set.

6.5.2 Local Profiles

One advantage of the 1D model is to get an insight of the local profiles besides the integral behavior. The local profiles of the most important state values are shown in Fig. 6.7 for the following current densities: i) low current density: $i = 0.1 \text{ A cm}^{-2}$, ii) moderate current density: $i = 1.5 \text{ A cm}^{-2}$ and iii) high current density: $i = 3.0 \text{ A cm}^{-2}$.

The electron and proton potential profiles are shown in Fig. 6.7a). Both potential profiles increase with current density and towards the anode. The differences between electron and proton potentials of both sides are caused by the respective activation overpotentials $\eta_{\text{act}}^{\text{a/c}}$ and half-cell potentials $E^{\text{a/c}}$.

Fig. 6.7b) shows temperature profiles across the cell. The temperature profile is quite comparable to the model results of Siemer et al. [150], who modeled the temperature profile of a PEM fuel cell. The temperature maximum is located within the membrane because of the heat input due to Joule heating of the proton current in combination with the low thermal conductivity of the membrane material. Also within the catalyst layers Joule heating due to electron and proton currents and the heat input due to kinetic losses lead to temperature increases. Whereas, vaporization of liquid water and the heat consumption due to entropy changes reduce the temperature increases. For the base

case parameter set the temperature increases are quite small, e. g. at 3.0 A cm^{-2} the maximal temperature within the membrane is around $0.8 \text{ }^\circ\text{C}$ higher than the boundary conditions. These small temperature increases are a consequence of the quite good cell performance. In cases with higher voltage losses, e. g. cells with thicker membranes, the temperature increases can be significantly higher. Especially, at very high current densities the temperature increases can be up to several degrees Celsius, since the temperature raises exponentially with current density.

However, in certain cases the temperature of the cathode side can be below the boundary temperature, as it can be seen in Fig. 6.7b) for a current density of 1.5 A cm^{-2} . This can be explained by the high vaporization heat in comparison to low heat sources, because of low overpotentials within the cathode.

In Fig. 6.7c) profiles of the gas pressure can be seen. The gas pressure increases towards the membrane on the anode and cathode side, because of the two-phase flow through the porous media. The higher the current density, the higher the local pressure enhancement. However, with the base case parameter set the gas pressure is enhanced by only several mbar.

The dissolved hydrogen and oxygen concentration profiles are shown in Fig. 6.7d). On both sides the dissolved gas concentrations are higher than the saturation concentrations according to Henry's law of roughly 0.4 mol m^{-3} . Since the supersaturation is small at low current densities, the concentration profiles of a current density of 0.1 A cm^{-2} are very close to the saturated concentrations according to Henry's law. The maxima of the dissolved gas concentrations are located at the CL/mem interfaces. These concentration peaks directly at the membrane lead to higher concentration gradients across the membrane, hence this causes higher crossover fluxes.

In Fig. 7.1c)–e) the local temperature, gas pressure and dissolved hydrogen profiles are shown at a current density of 3 A cm^{-2} . The *Charge bal. only* case, where the three mentioned phenomenological coefficients are multiplied by a factor of $1 \cdot 10^8$, accordingly shows no increased temperature, pressure and concentration profiles. Whereas, the *Full model* case shows for all observed state values increases. The remaining three cases: *Temperature*, *Pressure* and *Supersaturation* show only influences on the corresponding profiles. Consequently, this case study enables the possibility to investigate the effect of local temperature, pressure and dissolved gas concentration increases on crossover and cell voltage separately.

The hydrogen crossover fluxes of each case in Fig. 7.1a) show that only the *Supersaturation* and *Full model* cases have distinct increases in crossover, which are comparable to the experimental findings of the chapters 4 and 5 (cf. Fig. 4.1b) and 5.3b)). This is caused by the high dissolved hydrogen concentrations at the cathode-membrane interface (s. Fig. 7.1d)), which lead to higher crossover fluxes. This means that the literature-based mass transfer parameters of dissolved gas towards the gas phase are in the right order of magnitude to explain the experimental findings. In contrast, the *Temperature* and *Pressure* cases show only small enhances in crossover compared to the *Charge bal. only* case, which can be seen within the zoomed inset of Fig. 7.1a). The increases in gas pressure and temperature of the *Temperature* and *Pressure* cases are too small to affect the gas crossover to a significant amount.

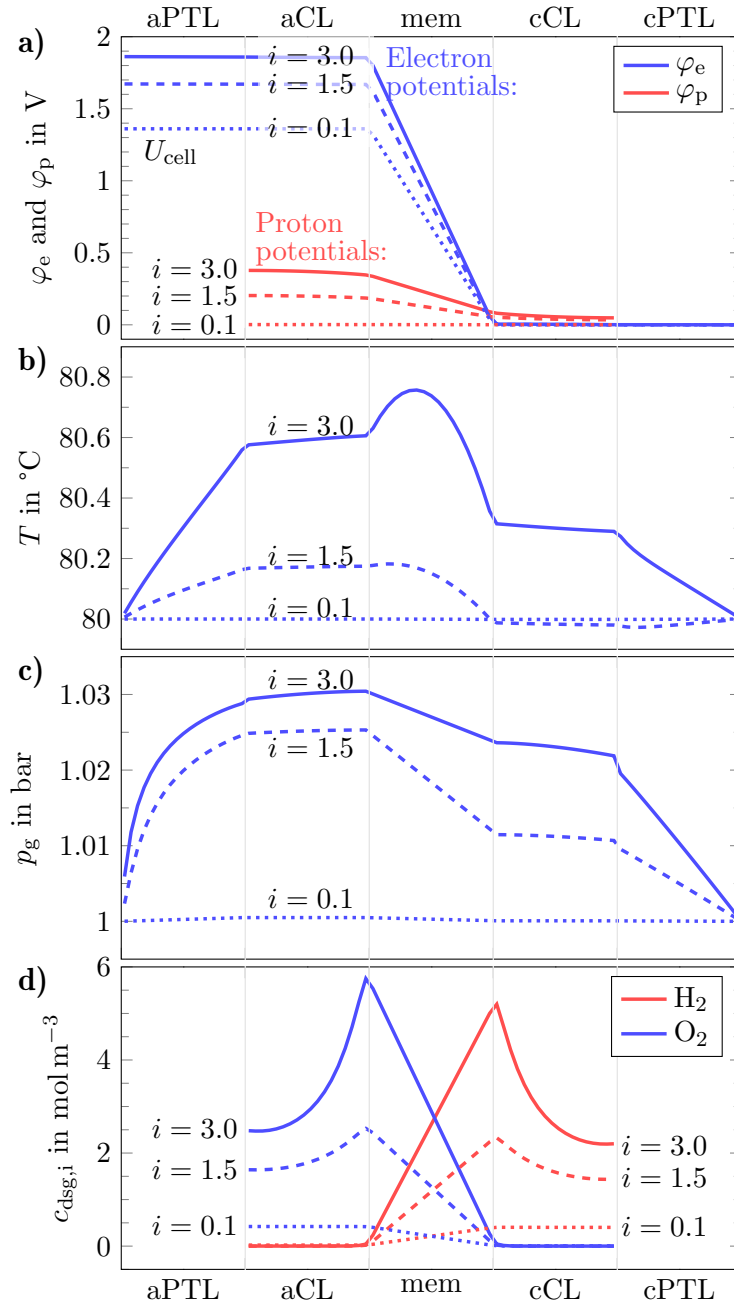


Figure 6.7: Local profiles of important state values as a) electron and proton potentials, b) temperature, c) gas pressure and d) dissolved hydrogen and oxygen concentrations. The local profiles are shown through the cell for three current densities (0.1, 1.5 and 3.0 A cm^{-2}).

In Fig. 6.8 other important local profiles are depicted, as the gas evolution rates, half-cell potentials and activation overpotentials. These profiles appear only within the catalyst layers. The profiles of the production rate are shown in Fig. 6.8a). For higher current densities the major part of the gas evolution of hydrogen and oxygen is

located very close towards the membrane. This is caused by the low proton conductivity compared to the electron conductivity, which is comparable to the reaction fronts in PEM fuel cells [151, 152].

The profile of the production rate is the reason of the dissolved gas concentration peaks at the CL/mem interfaces (cf. Fig. 6.7d)). Due to the high gas evolution rates the dissolved gas concentrations are also maximal directly at the membrane interfaces. Because of the concentration dependence of the half-cell potentials (Nernst equation), the concentration profiles also affect the half-cell potentials, which is shown in Fig. 6.8b). Consequently, its maxima are also located at the membrane interfaces.

The local reaction profiles can also be seen by the kinetic overpotentials in Fig. 6.8c). The activation overpotentials are maximal at the membrane interfaces, because of the low proton conductivity. However, the local profiles of the overpotentials are not significantly pronounced, due to the logarithmic correlation between the activation overpotentials η_{act} and production rates σ_{BV} (s. Butler-Volmer Eq. (6.4)).

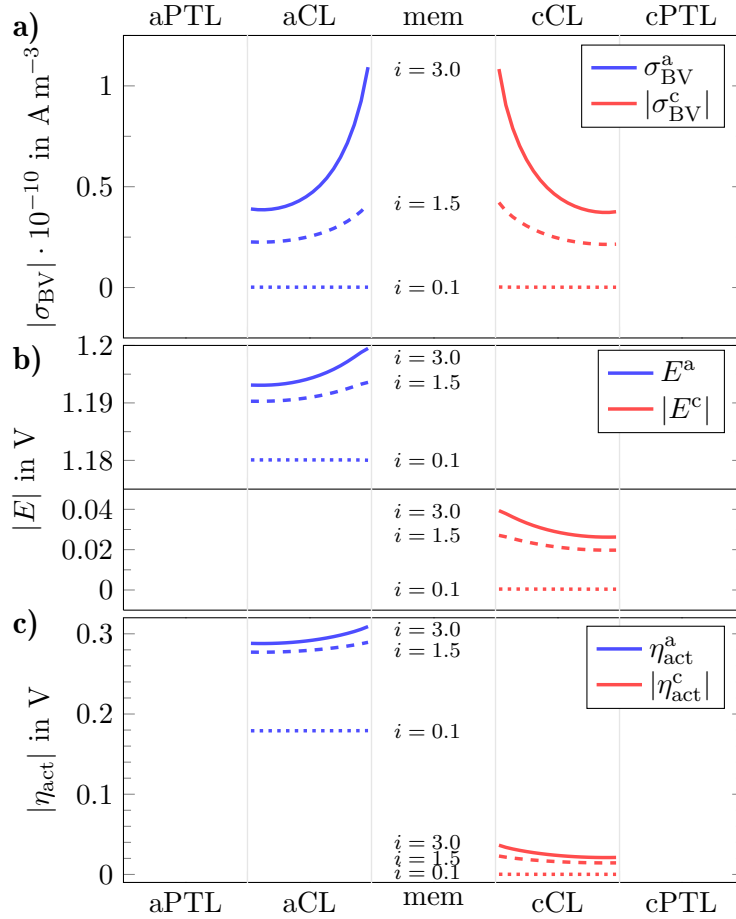


Figure 6.8: Local profiles within the catalyst layers of a) the production rates, b) half-cell potentials and c) activation overpotentials. The local profiles are shown through the cell for three current densities (0.1, 1.5 and 3.0 A cm⁻²).

6.6 Concluding Remarks

To answer the 5th research question a physically meaningful, one-dimensional model in through plane direction of a common five layer PEM water electrolysis cell setup is formulated. This comprehensive model includes the description of the electron and proton potentials, the dissolved gas (hydrogen and oxygen) and dissolved water concentrations, the two-phase flow of liquid water and gases (hydrogen, oxygen, water vapor) and temperature. Special focus is on the transport of dissolved gases within the catalyst layers and membrane to implement the supersaturation theory of section 4.2.

The integral model results agree quite well with the previous experimental data. An instance that could be obtained without any optimizing or fitting of e. g. kinetic parameters or phenomenological coefficients as proton conductivity or diffusion coefficients.

The ability to investigate the local profiles allows a detailed view of different effects. Particularly important is the profile of the production rate (s. Fig. 6.8a)). Because of the low proton conductivity within the CL, the gas production rate is very high close to the membrane interfaces. This leads to increased dissolved gas concentrations, half-cell potentials and activation overpotentials directly at the membrane interface.

7 Model-based Investigations

Subsequently to the model results according to the base case parameter set, the model is now used to investigate and explain certain experimental findings (RQ 5). The following listing gives an overview of the investigated aspects and how they are explained/investigated by means of the model. The listing number is chronological and equal to the section number.

- 7.1 Examination of the effects of the different transport mechanisms on gas crossover and cell voltage. Therefore, successively different transport mechanisms are turned off to investigate the single effects of the concerning transport mechanisms, which were turned on.
- 7.2 Investigation of a complete cell voltage loss breakdown with focus on the proton losses within the catalyst layers.
- 7.3 Analysis of the effect of cathode pressure on hydrogen crossover and cell voltage, particularly the mass transport losses. Therefore, the cathode pressure is changed.
- 7.4 Investigation of the effect of ionomer content on gas crossover and cell voltage.
- 7.5 Consideration of system relevant issues as the overall cell efficiency and operating window.

Finally, at the end of this chapter, the results are summarized briefly in addition to concluding remarks.

7.1 Influences of the different Transport Mechanisms on Gas Crossover and Cell Voltage

Within this work different possible reasons of the observed crossover increase with current density are discussed. In this section the comprehensive model is used to investigate the single effects of local temperature, gas pressure and dissolved gas concentration profiles on crossover and polarization behavior.

Therefore, the underlying transport mechanisms are step by step eliminated. This can be obtained by setting the related phenomenological coefficients: hydraulic permeability K_{hyd} , thermal conductivity λ_T and mass transfer coefficient k_1 successively towards very high values. Overall there are five different cases distinguished, namely:

- *Full model*: with the base case parameter set according to section 6.4.

- *Supersaturation*: herein the effect of the mass transfer coefficient k_1 is investigated in the absence of heat balance and two-phase flow. For this purpose, the hydraulic permeability of the porous layers K_{hyd} and the thermal conductivity λ_T are multiplied by a factor of 10^8 . Consequently, this case is isobaric and isothermal.
- *Temperature*: herein the effect of the temperature increase is investigated in the absence of mass transport limitations. Therefore, the hydraulic permeability of the porous layers K_{hyd} and the mass transfer coefficient k_1 are multiplied by a factor of 10^8 . Consequently, this case is isobaric and saturated conditions are obtained.
- *Pressure*: this case observes only the effect of pressure increases in the absence of mass transfer limitations and temperature increases. For this purpose, the thermal conductivity λ_T and mass transfer coefficients k_1 are multiplied by a factor of 10^8 . Consequently, this case is isothermal and the dissolved gas concentrations do not increase above their saturation limit.
- *Charge balances only*: herein all mass transport limitations and the temperature increase are turned off. Therefore, the hydraulic permeability of the porous layers K_{hyd} , the thermal conductivity λ_T and the mass transfer coefficient k_1 are multiplied by a factor of 10^8 . Consequently, this case is isothermal, isobaric and the dissolved gas concentrations are saturated.

Fig. 7.1a) shows the hydrogen crossover, important local profiles are depicted in Fig. 7.1b)–d) and on the right side the polarization curves of all 5 cases are shown (Fig. 7.1e)).

In Fig. 7.1b)–d) the local temperature, gas pressure and dissolved hydrogen profiles are shown at a current density of 3 A cm^{-2} . The *Charge bal. only* case, where the three mentioned phenomenological coefficients are multiplied by a factor of $1 \cdot 10^8$, accordingly shows no increased temperature, pressure and concentration profiles. Whereas, the *Full model* case shows for all observed state values increases. The remaining three cases: *Temperature*, *Pressure* and *Supersaturation* show only influences on the corresponding profiles. Consequently, this case study enables the possibility to investigate the effect of local temperature, pressure and dissolved gas concentration increases on crossover and cell voltage separately.

The hydrogen crossover fluxes of each case in Fig. 7.1a) show that only the *Supersaturation* and *Full model* cases have distinct increases in crossover, which are comparable to the experimental findings of the chapters 4 and 5 (cf. Fig. 4.1b) and 5.3b)). This is caused by the high dissolved hydrogen concentrations at the cathode-membrane interface (s. Fig. 7.1d)), which lead to higher crossover fluxes. This means that the literature-based mass transfer parameters of dissolved gas towards the gas phase are in the right order of magnitude to explain the experimental findings. In contrast, the *Temperature* and *Pressure* cases show only small enhances in crossover compared to the *Charge bal. only* case, which can be seen within the zoomed inset of Fig. 7.1a). The increases in gas pressure and temperature of the *Temperature* and *Pressure* cases are too small to affect the gas crossover to a significant amount.

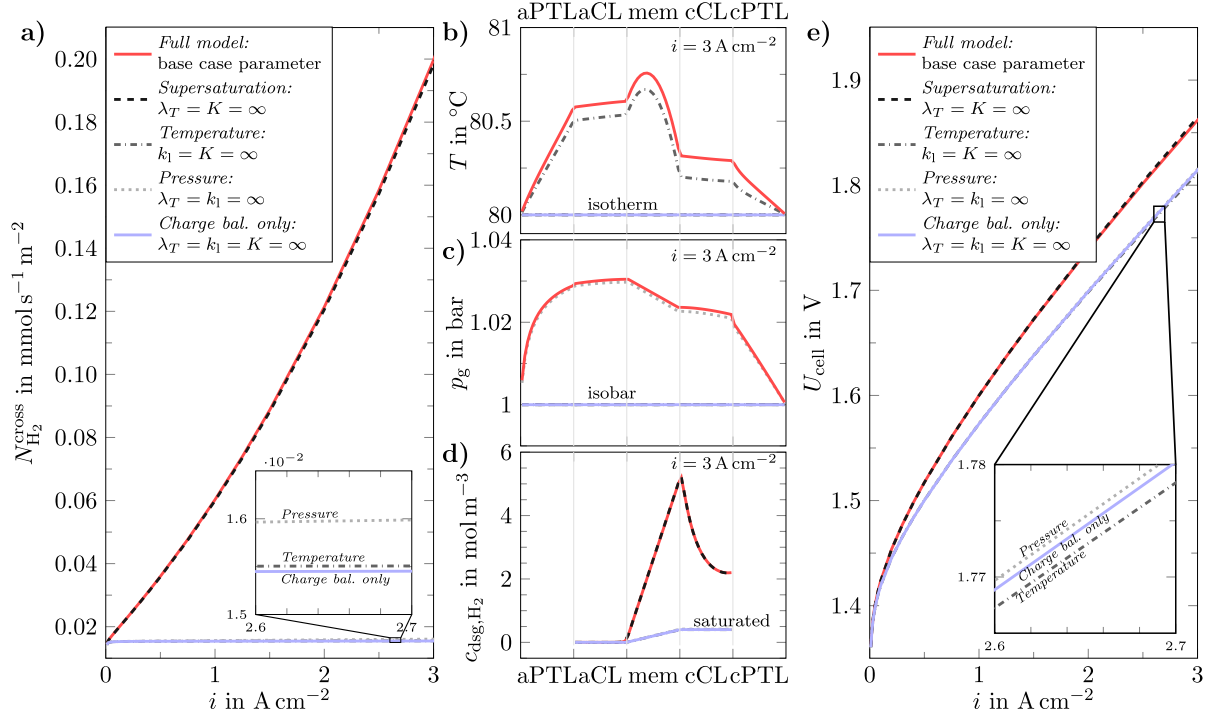


Figure 7.1: Case study to investigate the single effects of b) temperature, c) gas pressure and d) dissolved gas concentration profiles on a) hydrogen crossover and e) cell voltage. Therefore, the phenomenological coefficients: hydraulic permeability K_{hyd} , thermal conductivity λ_T and mass transfer coefficient k_1 are successively set to high values to eliminate the corresponding current density dependencies. The local profile of subfigure b)–d) are depicted for a current density of 3.0 A cm^{-2} .

Also for the polarization curves in Fig. 7.1e) the *Supersaturation* and *Full model* cases show also distinct differences in comparison to the other 3 cases. This is caused by the increased half-cell potentials due to supersaturated dissolved gas concentrations within both catalyst layers, which is considered by the Nernst equations. These mass transport losses have a significant share.

Whereas, the remaining *Temperature* and *Pressure* case show only small deviations in comparison to the *Charge bal. only* case. The zoomed inset of Fig. 7.1e) shows that temperature increases induced by increasing current density have only small beneficial effects on the performance. These beneficial effects are caused by increases in proton conductivity (s. Eq. (A.1)), exchange current density (s. Eq. (A.2)) and decrease in reversible cell potential (s. Eq. (A.4)) with increasing temperature. This temperature increase is also the reason why the voltage curve of the *Full model* case is slightly better than that of the *Supersaturation* case.

7.2 Voltage Loss Breakdown

The previously shown polarization curves in Fig. 7.1e) of the *Full model* and *Supersaturation* cases show significant differences in comparison to the other three cases without supersaturated dissolved gas concentrations. These are caused by increases in half-cell potentials due to the higher dissolved gas concentrations, which are caused by mass transfer resistances. These mass transport losses and the other voltage losses are shown in a complete voltage loss breakdown in Fig. 7.2a). The voltage losses are divided into three separately colored groups: at the top the previously mentioned mass transport losses (cyan), in the middle ohmic losses (red) and at the bottom kinetic losses (blue). In addition to the voltage loss breakdown, corresponding local profiles of the half-cell potentials, proton potential and activation overpotentials are shown in Fig. 7.2b)–d) at 3 A cm^{-2} . Within these local profiles all voltage losses are included.

In the following the losses are described step by step. The mass transport losses $\Delta E^{a/c}$ reflect in differences between the actual half-cell potentials $E^{a/c}$ and the reversible half-cell potentials $E_{\text{rev}}^{a/c}$ (dashed lines) for the anode and cathode side (s. Fig. 7.2b)). The actual half-cell potentials are higher due to supersaturated dissolved gas concentrations, which are caused by mass transfer resistances.

Ohmic losses due to proton transport are depicted below the mass transport losses. The proton transport losses ΔU_{H^+} are split up to membrane and both catalyst layers, which is illustrated in Fig. 7.2c). Due to the distinctly thicker membrane compared to both catalyst layers, the membrane is responsible for the major part of these ohmic losses. Nevertheless, both catalyst layers show significant losses in the proton potential.

Last but not least, the voltage loss breakdown shows the kinetic losses, with its local profiles given in Fig. 7.2d). The losses of the OER are much higher in comparison to the overpotentials of the HER.

The base line of the voltage loss breakdown is the reversible cell potential E_{rev} , which is calculated for the applied operating conditions (cell temperature and gas pressure on each side).

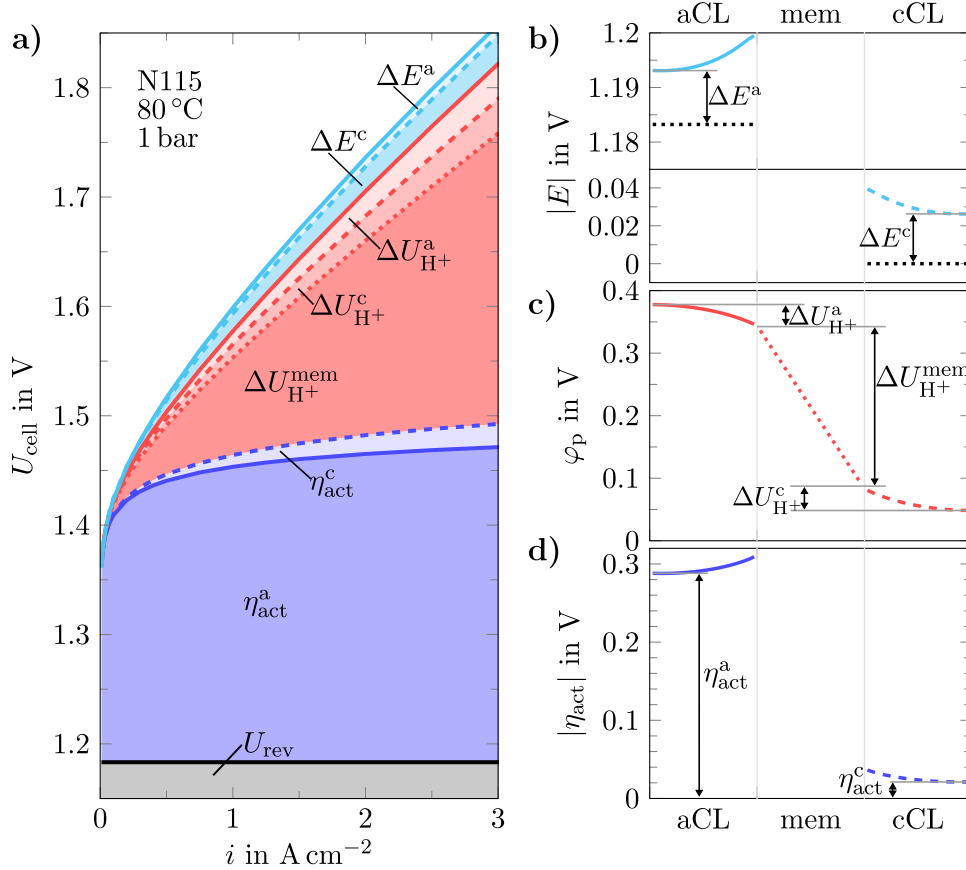


Figure 7.2: Subfigure a) shows a full voltage loss breakdown separated into mass transport losses, ohmic losses and kinetic losses. These losses are depicted by the underlying local profiles at 3 A cm^{-2} , which are shown in b) the local half-cell potentials, c) the proton potential and d) the activation overpotentials.

The ohmic losses due to proton transport $\Delta U_{\text{H}^+}^{\text{a/c}}$ within both catalyst layers are investigated in more detail in Fig. 7.3a). It can be seen that the ohmic losses increase with current density. However, the voltage losses increase is less strong than a linear correlation suggests. Consequently, the effective proton resistances $R_{\text{H}^+}^{\text{eff}}$ are not constant, but rather have to decrease with increasing current density, as shown in Fig. 7.3b).

This decrease in effective proton resistance can be explained by the shift of the local reaction profile towards the membrane at higher current densities (s. Fig. 6.8a)). Consequently, the mean proton transport path within the catalyst layer is reduced and the effective proton resistances decrease with increasing current density.

The decrease of the effective proton resistances in catalyst layers is also known for PEM fuel cells [152]. Neyerlin et al. [152] shows an analytical solution of the effective proton resistance within the cathode catalyst layer of a PEM fuel cell. The results of Neyerlin et al. [152] are also shown in Fig. 7.3b). It can be seen that the qualitative trend agrees very well with the trend of this work. However, the effective resistances of the analytical solution of Neyerlin et al. [152] are smaller. The quantitative differences can be explained by the mass transport losses, which are not considered within the

analytical solution of Neyerlin et al. [152]. However, the mass transfer resistances induce that the concentrations at the membrane are higher (s. Fig. 6.7d)). This, in turn, raises the half-cell potentials (s. Fig. 6.8b)), which leads to reduced production rates at the CL/membrane interfaces. Consequently, the mean proton path length and thus the effective proton resistance increase with mass transfer resistances.

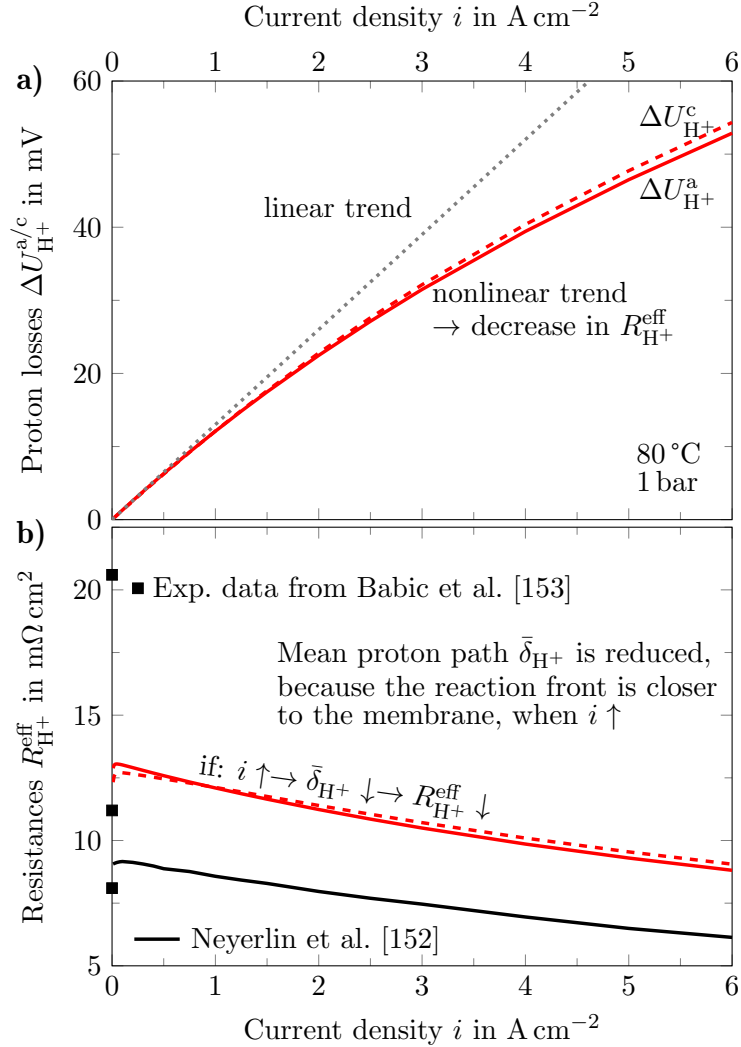


Figure 7.3: Subfigure a) shows the ohmic losses due to proton transport and b) the effective proton resistances for both catalyst layers. The effective proton resistances decrease with increasing current density, because of the increases of the production rate directly at the membrane, thus leading to a reduction of the mean proton transport path length.

Furthermore, experimental measurements of Babic et al. [153] are also depicted in Fig. 7.3b). These three data points represent the effective proton resistances for an anode catalyst layer for three different PTLs. This comparison intends to confirm that the order of magnitude of the model results are plausible.

7.3 Cathode Pressure Variation

A very important system relevant operating condition of an electrolyzer is the cathode pressure [125,154], the pressure level at which hydrogen is produced. At higher cathode pressure the Faraday efficiency decreases [11] and also safety is getting an issue [11,18,155]. In chapter 4 the effect of different cathode pressures on the hydrogen crossover, especially on the crossover increase with current density is observed (s. Fig. 4.3). At higher pressures, the H_2 in O_2 content increases due to higher hydrogen crossover fluxes. The slopes of the hydrogen crossover increases with current density slightly increase with pressure. This aspect should be further investigated by means of the model.

The simulation results for different cathode pressures are shown in Fig. 7.4. The left hand side of Fig. 7.4 shows polarization and iR -free cell voltage curves. In the middle of Fig. 7.4 important local profiles are depicted, which help to explain the integral results. On the right hand side of Fig. 7.4 the hydrogen in oxygen content and hydrogen crossover can be seen.

The model results correspond well to the experimental findings (cf. Fig. 4.3). The higher the cathode pressure, the higher the hydrogen in oxygen content, which is shown in Fig. 7.4f). At 30 bar the hydrogen in oxygen content only drops below 2 vol.% at current densities above 2 A cm^{-2} . Whereas, at atmospheric pressure this safety limit is satisfied at few mA cm^{-2} . This is caused by the increased hydrogen crossover for higher cathode pressures, which can be seen in Fig. 7.4g).

The current density dependence of the hydrogen crossover is quite identical for the investigated pressures. The almost similar slopes can be explained by similar increases in dissolved hydrogen concentrations at the cathode/membrane interface, which are shown in Fig. 7.4c). The grey lines correspond to the saturation concentrations according to the corresponding cathode pressures, which are calculated by Henry's law (Eq. (A.6)). The differences between the supersaturated and the saturated dissolved hydrogen concentrations are quite similar for all pressures. That is because the considered mass transfer resistances include the diffusive transport of dissolved hydrogen through the ionomer (from the catalyst particles towards the pore space) and the diffusion coefficients of dissolved gases within the ionomer water are pressure independent.

However, as previously mentioned, the crossover increases are not completely identical, which can be seen in Fig. 4.3b) and from the model results in Fig. 7.4g). The crossover increases between 1 and 2 A cm^{-2} are slightly steeper at higher pressures. This is caused by the local temperature increase with current density, which leads to increases of the diffusion coefficient of dissolved gases through the membrane. This enhances the crossover flux, as it was shown in subsection 7.1. However, this temperature effect on crossover is even stronger at higher pressures (s. sec. 2.2.2). Additionally, at higher pressures the catalyst and membrane temperature is also higher, since less heat is needed for vaporization.

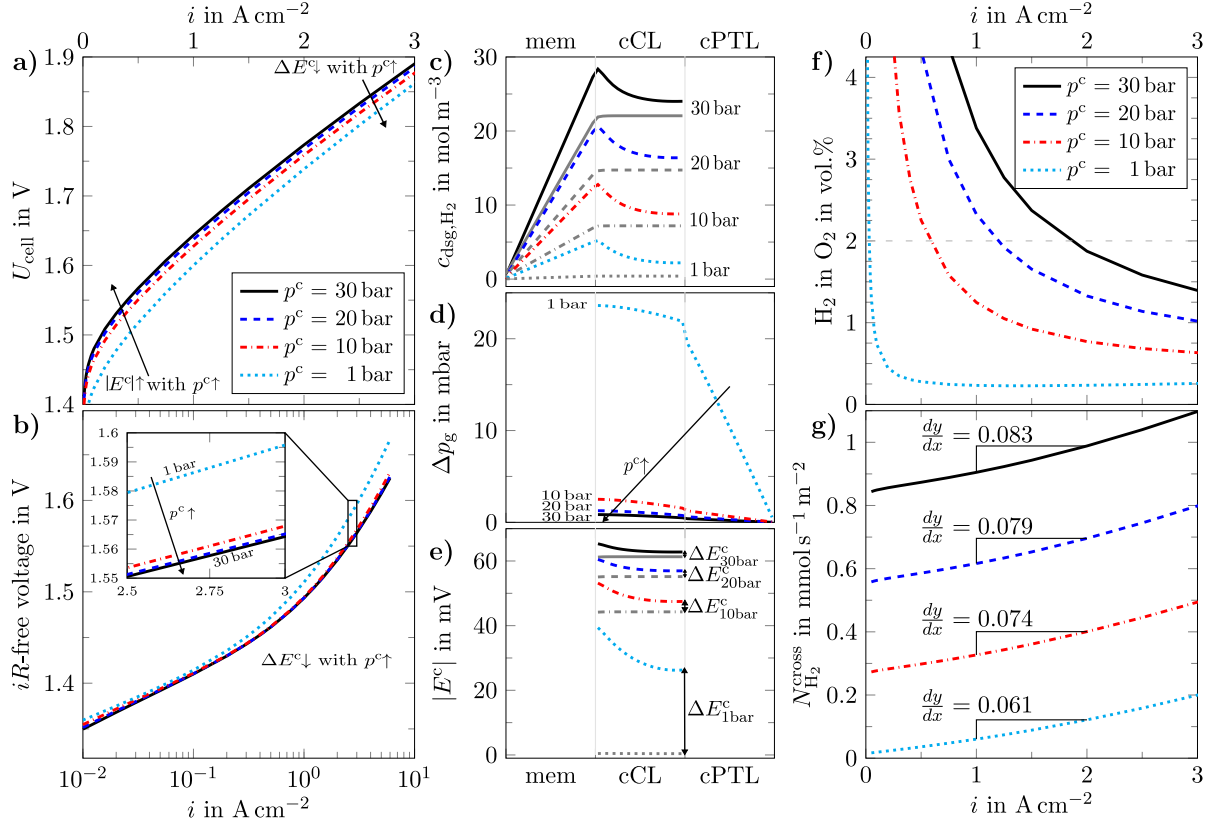


Figure 7.4: Effect of cathode pressure on cell performance a),b) and hydrogen crossover f),g). The local profiles at a current density of 3 A cm^{-2} show the dissolved hydrogen concentration c), cathode pressure enhancement over porous media d) and cathode half-cell potential e). The grey curves within the local profiles are the values corresponding to operating conditions without mass transport losses.

Fig. 7.4d) shows the gas pressure increases across the cathode. The gas pressure enhancement in the porous layers is strongly reduced for higher cathode pressures. This can be explained by the enhanced mass transport at higher pressures (Darcy's law, Eq. (6.24)), which was also shown by the simple model results in section 4.2. The higher the pressure, the better the gaseous mass transport and consequently lower pressure drops arise across the porous layers. From these results it must be concluded that next to the quantitative discussion of the case study in subsection 7.1, now also the local pressure enhancement even qualitatively does not explain the increase of crossover with current density. Whereas, the crossover increases with current density also at higher pressures, the pressure enhancement over the porous layers is significantly reduced. Consequently, local pressure increases can not explain the crossover increase with current density, neither qualitatively nor quantitatively.

Fig. 7.4a) shows the polarization curves for 4 different cathode pressures. Because of the increase in half-cell potential with increasing pressure (Nernst), the cell voltage is higher for higher pressures. However, at higher current densities and higher cathode

pressures the polarization curves converge again. This is caused by the reduction of the cathodic mass transport losses ΔE^c , which can be seen in Fig. 7.4e). It shows the local profiles of the cathodic half-cell potentials. The grey lines represent the pressure and temperature dependent reversible cathodic half-cell potentials, corresponding to the operating conditions. The differences between the actual and reversible half-cell potentials decrease, because of the logarithmic concentration dependence of the half-cell potential (s. Nernst Eq. (6.7)).

Fig. 7.4b) shows that the iR -free cell voltage decreases with cathode pressures, because of the previously discussed reduction of cathodic mass transport losses ΔE^c . This effect of decreasing iR -free cell voltage or η_{mtx} with pressure was recently observed experimentally by Suermann et al. [37].

All losses at the cathode side, activation overpotentials, ohmic losses within the cathode catalyst layer and mass transport losses are summarized in Fig. 7.5 for a current density of 3 A cm^{-2} and plotted versus cathode pressure. It can be seen directly that the overall losses decrease with cathode pressure. This is mainly caused by the previously discussed reduction of the cathodic mass transport losses. But also the cathode kinetic losses and ohmic losses decrease slightly, since the production profile (reaction front) moves closer to the membrane interface and therefore the mean proton pathway is reduced.

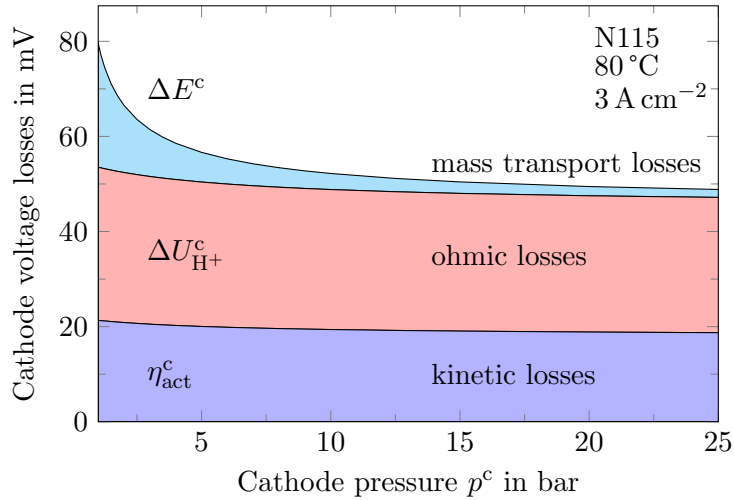


Figure 7.5: Cathode loss breakdown plotted versus cathode pressure. Strong decrease in cathode mass transport losses ΔE^c can be observed, because of the logarithmic correlation between half-cell potential and concentration (Nernst equation).

7.4 Ionomer Variation

Beside the variation of operating conditions, as previously shown, the model allows also to analyze the effects of structural changes, such as the cathode ionomer variation, which is experimentally investigated in chapter 5. The experimental investigation reveals a strong influence of the ionomer content on the cell voltage and gas crossover, both increase

with increasing ionomer content between 10 and 40 wt.%. In this section the model is used to explain and investigate the experimental findings in more detail. For the model based analysis the ionomer fraction within the cathode catalyst layer $\varepsilon^{\text{cCLion}}$ is changed between 10 and 40 vol.% (base case parameter is 20 vol.%). Unfortunately, the conversion of the experimental ionomer wt.% in model vol.% is not possible¹. Consequently, the simulation results cannot be directly compared with the experimental results from chapter 5. However, a qualitative comparison and a more detailed investigation of the different effects is possible.

First, the effect of the ionomer variation on the transport parameters of the model is shown in Fig. 7.6. Particularly, the mass transfer of dissolved gases and the proton transport within the catalyst layers are affected by the ionomer fraction. On the left y-axis the product of mass transfer coefficient k_1 and volume specific area of the ionomer a_{ion} are shown, which represents the quality of the mass transfer. This product decreases with increasing ionomer content, since the thickness of the mean ionomer path increases and the volume specific area decreases (s. Eq. (6.13) and (6.14)). At very low ionomer contents the mass transfer also decrease due to a reduction of the volume specific area of the ionomer (Eq. (6.13)). Consequently, this leads to increased mass transfer resistances for higher ionomer contents.

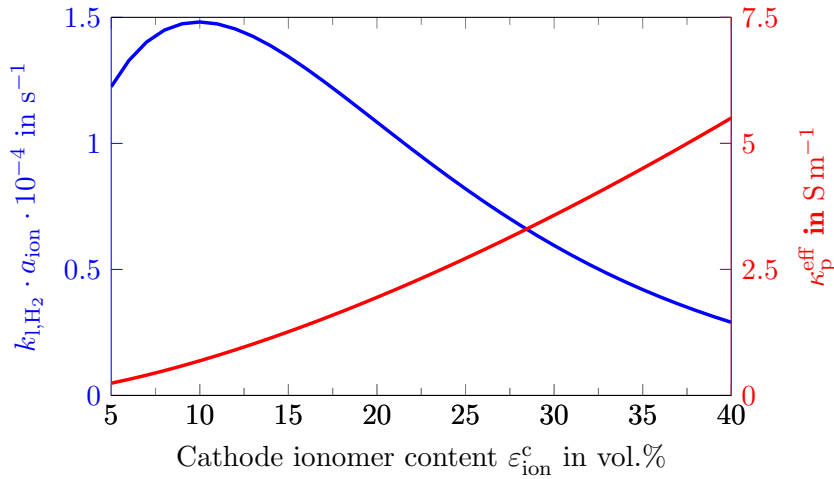


Figure 7.6: Mass transfer and proton conductivity trade-off versus ionomer content. The proton conductivity increases, while the mass transfer decreases with ionomer content.

On the right y-axis of Fig. 7.6 the effective proton conductivity $\kappa_{\text{p}}^{\text{eff}}$ is depicted. The proton conductivity increases with increasing ionomer content, due to the higher ionomer content itself and the reduction of ionomer tortuosity (s. Eq. (2.12)). Consequently, the ohmic losses of the catalyst layers decrease with increasing ionomer content.

The previously shown parameters affect the cell behavior, which is shown in Fig. 7.7. The effect of the four different cathodic ionomer contents (10, 20, 30 and 40 vol.%) on

¹At the time of this work physical data from the prepared cathodes for conversion were missing.

cell performance is shown in Fig. 7.7a), b) and the effect on hydrogen crossover is shown in Fig. 7.7f), g). Local profiles for a detailed investigation are shown in Fig. 7.7c) – e) at a current density of 3 A cm^{-2} .

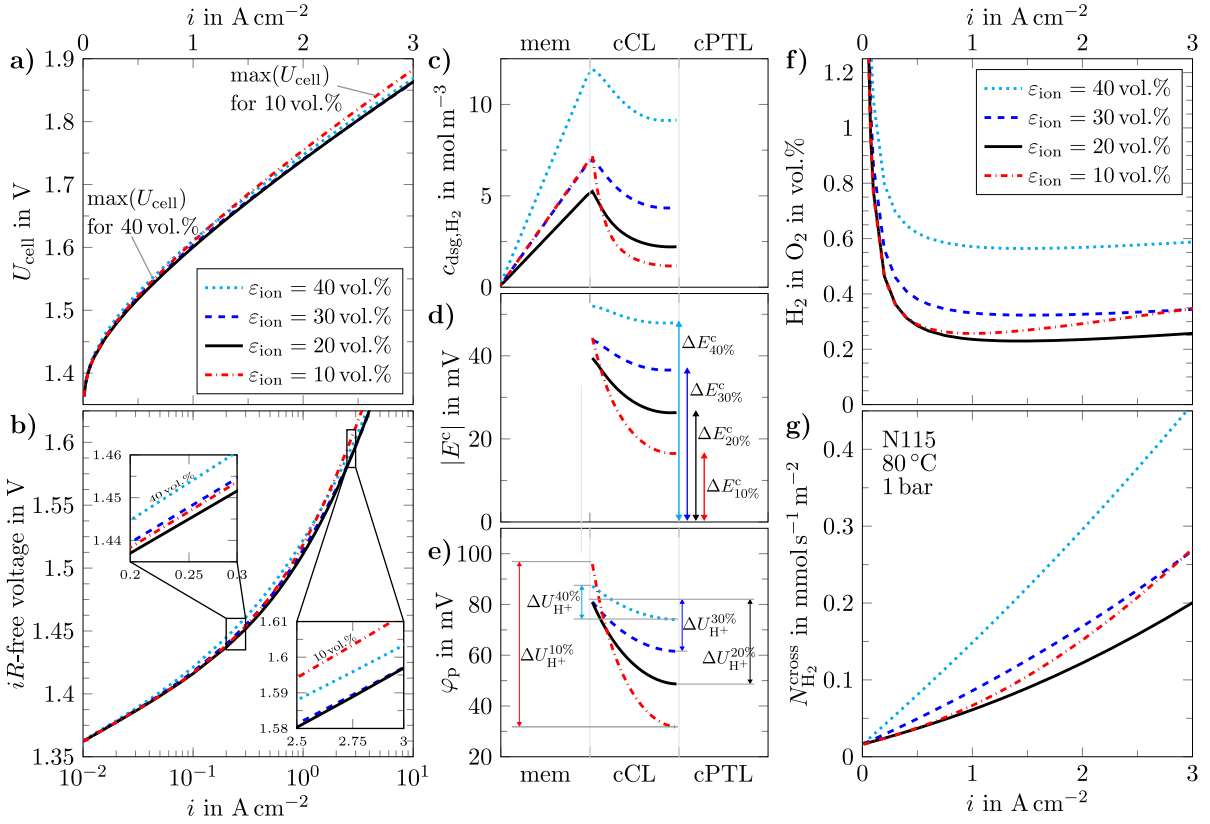


Figure 7.7: Ionomer variation within the cathode catalyst layer. On the left side the effect on cell performance is shown a), b) and on the right side the effect on hydrogen crossover f), g) is shown. In the middle important local profiles at 3 A cm^{-2} are presented.

Similar to the experimental findings, the model results also show that the crossover increases with increasing ionomer content (between 20 and 40 vol.%), which can be seen in Fig. 7.7g). Thereby, the H_2 in O_2 content is highest for the 40 vol.% case (s. Fig. 7.7f)). That means, the crossover increases with increasing ionomer content. However, the hydrogen crossover can also increase again at low ionomer contents, e.g. the hydrogen crossover for the 10 vol.% ionomer content case is even higher as for the 20 vol.% ionomer case and at 3 A cm^{-2} it is also higher as for the 30 vol.% case.

The reason for this behavior can be seen within the local dissolved hydrogen concentrations in Fig. 7.7c). The highest ionomer content results in the highest hydrogen concentration level at the membrane interface. However, the concentration profile of the lowest ionomer content has a strong increase towards the membrane. This is caused by the strongly decreased proton conductivity, if only 10 vol.% ionomer is set, which can be seen in Fig. 7.7d) according to the very high ohmic losses due to the proton transport.

Consequently, the reaction front is shifted much closer towards the membrane. This leads to a very high gas evolution rate/production rate at the membrane interface that results in combination with mass transfer resistances to highly supersaturated dissolved gas concentrations directly at the membrane. Hence, the crossover increases very strongly with increasing current density at low ionomer contents.

The cell voltage shown in Fig. 7.7a) also increases with higher ionomer contents at medium current densities up to 1 A cm^{-2} . This in particular is caused by the increase in cathodic half-cell potential (Nernst), which is shown in Fig. 7.7d). These mass transport losses originate from the strongly supersaturated hydrogen concentrations of high ionomer contents. However, at high current densities the profiles of the lowest ionomer content of 10 vol.% have the worst polarization behavior. The increased cell voltage can not be explained by the increased half-cell potential, but rather by the higher ohmic losses ΔU_{H^+} due to decreased proton conductivity, which is shown in Fig. 7.7e).

The following can be summarized: at high ionomer contents the cell voltage and crossover are high due to increased mass transfer resistances, which originate from thicker ionomer films that lead to highly supersaturated dissolved gas concentrations, which cause the increases in crossover and mass transport losses. At low ionomer contents the crossover and cell voltage are also increased. Because of the decreased proton conductivity the ohmic losses within the catalyst layer are increased and hence the voltage losses. Additionally, this leads to a reaction front close to the membrane and consequently the supersaturation directly at the membrane is very high, which causes the strong increases in crossover.

The previous results highlight that there exist optimal ionomer contents concerning the cell voltage and gas crossover. The optimal ionomer content have the best trade-off between proton conductivity and mass transfer (cf. Fig. 7.6), as it was shown by Bernt and Gasteiger [23] for the anode ionomer content.

The optimal ionomer content is investigated in more detail within the following. Fig. 7.8a) shows the iR -free cell voltages plotted versus ionomer content including cathodic voltage loss breakdowns at 0.5 and 3 A cm^{-2} . The breakdowns show clearly that for low ionomer contents the ohmic losses $\Delta U_{\text{H}^+}^c$ predominate, whereas at higher ionomer contents the mass transport losses ΔE^c have the highest share. The optimal ionomer contents are highlighted by filled dots. It can be seen that the optimal ionomer content is not constant for both current densities. At low current densities the optimal ionomer content should be slightly lower, since ohmic losses are less important. Inversely, for higher current densities the ohmic losses gain importance and consequently the optimal ionomer content is shifted to higher values.

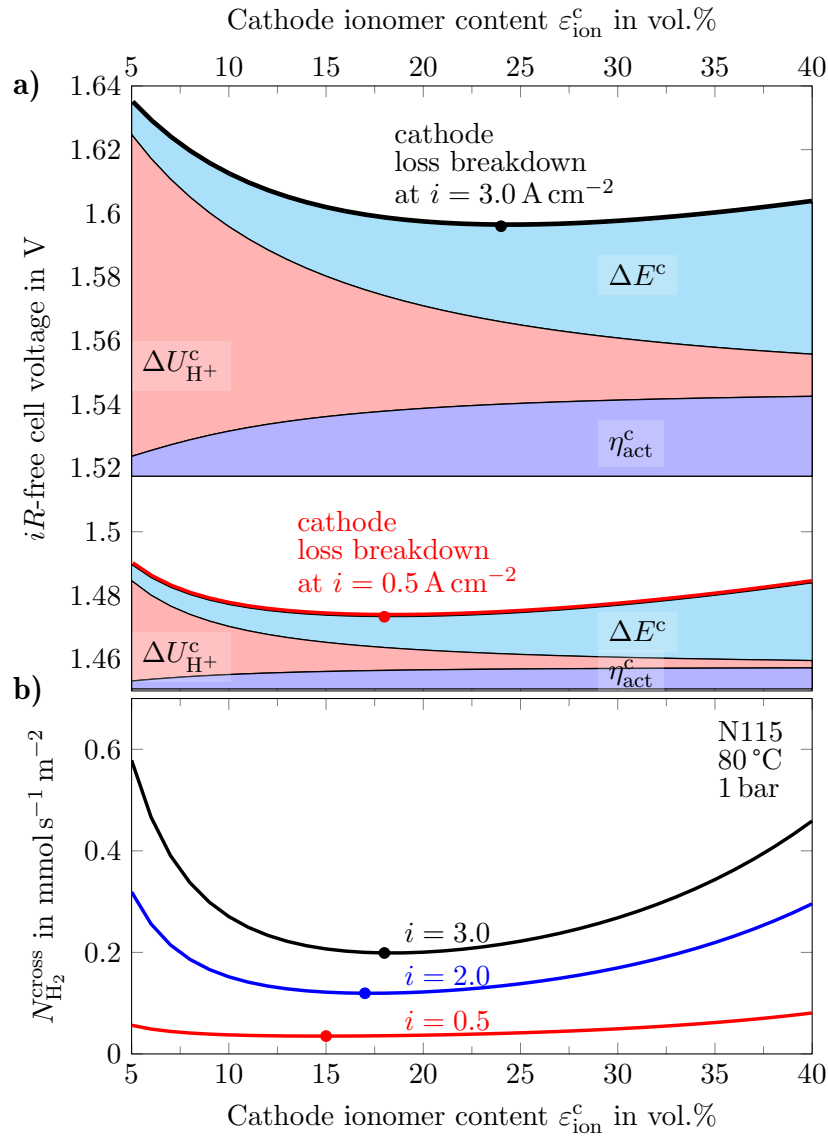


Figure 7.8: Optimal ionomer contents depending on current density for a) the iR -free cell voltage including cathodic loss breakdowns at 0.5 and 3.0 A cm^{-2} and b) the hydrogen crossover flux.

Fig. 7.8b) shows the hydrogen crossover flux also plotted versus cathode ionomer content. The crossover increases strongly with ionomer content due to the previously discussed higher mass transfer resistances. These mass transfer resistances decrease with decreasing ionomer content. Furthermore, as previously discussed the crossover increases again at very low ionomer contents. This can be explained by the shifted reaction front towards the membrane, because of the reduced proton conductivity. Hence, the local gas evolution rate is very high and leads to highly supersaturated gas concentrations directly at the membrane interface. Consequently, the concentration gradient across the membrane is increased and therefore the crossover. This effect is strengthened at higher

current densities, since the production profile is moved closer towards the membrane.

As well as for the cell voltage there exist not one ideal ionomer content, since it is slightly dependent on the applied current density. Furthermore, the value of optimal ionomer content for the electrochemical performance and crossover are not the same, though the optima are close to each other.

7.5 System Considerations

Within the previous sections the model was used to investigate the influence of certain changes in operating conditions and structural parameters on cell voltage and gas crossover, which have also been experimentally observed in the framework of this dissertation. In the following section the model is further used to investigate cell efficiency and system relevant issues.

7.5.1 Cell Efficiency

The cell efficiency η_{cell} as discussed within chapter 2, is the product of the voltage efficiency and Faraday efficiency:

$$\eta_{\text{cell}} = \eta_U \eta_{\text{H}_2} \quad (7.1)$$

Faraday Efficiency In the following the Faraday efficiency related to hydrogen η_{H_2} is investigated at different pressure conditions. Therefore, the definition of the Faraday efficiency is stated again:

$$\eta_{\text{H}_2} = \frac{N_{\text{H}_2}^{\text{c,out}}}{N_{\text{H}_2}^{\text{theo}}} = 1 - \frac{N_{\text{H}_2}^{\text{cross}} + N_{\text{H}_2}^{\text{recomb}} + \frac{i_{\text{short}}}{2F}}{\frac{i}{2F}} \quad (7.2)$$

For this investigation it is assumed that all of the permeating oxygen recombines with evolved hydrogen to water, i. e. $N_{\text{H}_2}^{\text{recomb}} = 2N_{\text{O}_2}^{\text{cross}}$. Consequently, the oxygen crossover and hence the recombination reaction causes a reduction in the Faraday efficiency of hydrogen. The oxygen crossover is often neglected due to the smaller diffusion coefficient in comparison to hydrogen [66, 78, 99], but even if the oxygen crossover is half of the hydrogen crossover it has the same effect on the Faraday efficiency, since two hydrogen molecules recombine per one oxygen molecule.

Fig. 7.9 shows the Faraday efficiency of hydrogen for balanced and differential pressure conditions. The higher the pressure level, the lower the Faraday efficiency [11]. Especially, at low up to moderate current densities the losses are up to several percents. At balanced pressure conditions, the previously mentioned effect of the hydrogen recombination with permeating oxygen can directly be seen, e. g. the case of 30 bar balanced pressure has a lower Faraday efficiency than the 50 bar differential pressure case. Consequently, at higher anode pressures the oxygen pressure has also a non-negligible impact on Faraday efficiency and consequently on the cell efficiency.

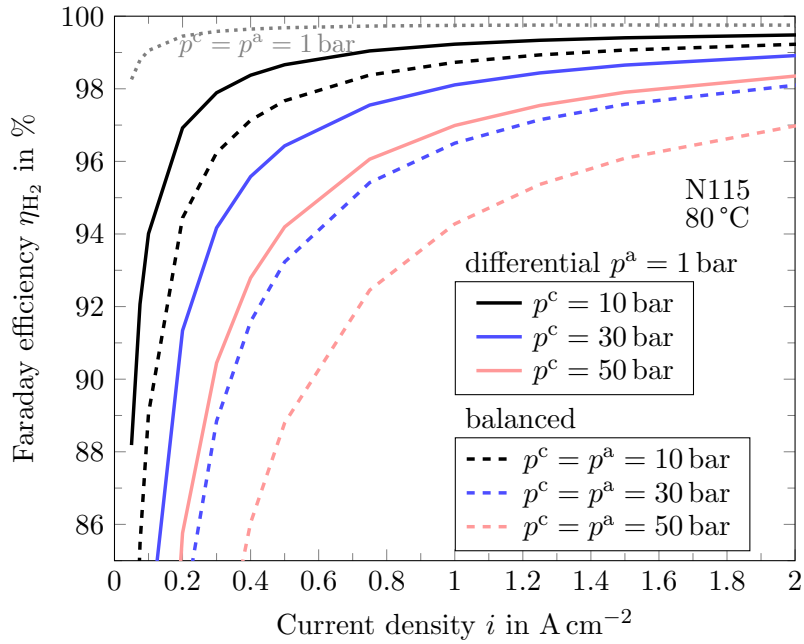


Figure 7.9: Faraday efficiency of hydrogen for balanced and differential pressure conditions. At balanced pressure the recombination of hydrogen with permeated oxygen to water shows a strong effect on the Faraday efficiency.

Cell Efficiency Fig. 7.10 shows cell efficiency maps for three different cathode pressures: 1, 30 and 50 bar at differential pressure conditions, i. e. atmospheric anode pressure. For each pressure a) – c) four different membrane thicknesses are shown: N117 (178 μm), N115 (127 μm), N212 (51 μm) and N211 (25 μm). The colored areas show the individual parts of the respective loss mechanisms, which are namely, Faraday, ohmic (only membrane), kinetic and remaining mtz losses, which include the mass transport losses and ohmic losses within the catalyst layers. For the thick membranes the ohmic losses due to proton transport are very high, whereas the Faraday losses are small. The influence of these two losses are inversely with the membrane thickness. Especially, the combinations of high pressures and thin membranes show distinct Faraday losses.

Additionally, the thick magenta colored lines of Fig. 7.10 highlight the highest cell efficiencies of each subfigure a) – c) as a function of current density and membrane thickness. For example in case of a differential pressure of 50 bar (Fig. 7.10c)) the thick N117 membrane has the highest cell efficiency at low current densities of 0 – 0.6 A cm^{-2} and in a current density range of 0.6 – 1.15 A cm^{-2} the N115 membrane has the highest cell efficiency, followed by the N212 membrane in the range of 1.15 – 2.7 A cm^{-2} and finally, for current densities above 2.7 A cm^{-2} the N211 membrane has the highest efficiency.

These efficiency maps are shown at differential operating conditions, at balanced pressure conditions the Faraday efficiency would be even lower because of the increased oxygen crossover and recombination reaction on the cathode (s. Fig. 7.9). Consequently, for balanced pressure conditions the thicker membranes would gain importance. This is not intuitive and it is only true in terms of cell efficiency, since at differential pressure

conditions the membrane has to be thicker to withstand the increased mechanical stress.

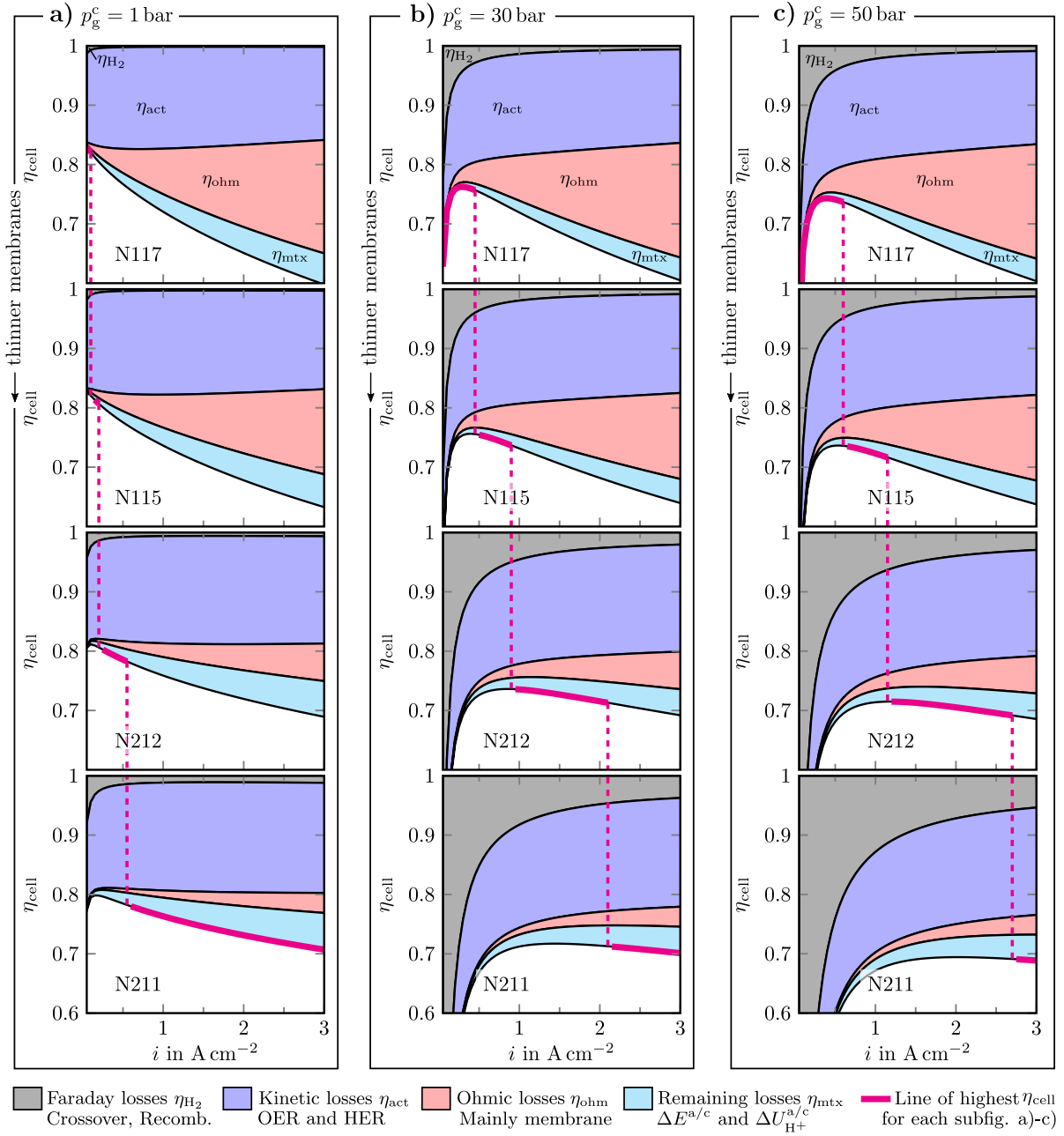


Figure 7.10: Cell efficiency maps for three different cathode pressures and 4 membrane thicknesses at 80 °C and differential pressure conditions ($p^a = 1$ bar). The cell efficiency is separated into 4 different parts, namely: faradaic, ohmic (membrane), kinetic and mtx losses. The highest cell efficiency of each subfigure is highlighted with the thick magenta line.

The following conclusions can be drawn from the efficiency maps: i) high efficiencies can be achieved for a wide current density range with thin membranes due to the strong

reduction of ohmic losses, but only at low pressures, while the Faraday losses are small. ii) Whereas, high efficiencies at high pressures can be achieved with thick and medium membrane thicknesses, but only for small till moderate current densities. Although, the fraction of Faraday losses decrease at higher current densities, however the ohmic losses increase significantly. Nevertheless, at very high current densities thin membranes can be useful again.

7.5.2 Operating Window

The previously shown efficiency maps do not contain information about safety issues. Although, hydrogen crossover is considered by the Faraday efficiency, but the hydrogen in oxygen content is not considered. Therefore, in the following the operating window is investigated.

The operating range is limited due to i) safety issues (minimal current density) and ii) a specific voltage limit (maximal current density). For this investigation a safety limit of 2 vol.% H₂ in O₂ [10] and a cell voltage of 2 V [10] are applied. The range between those limitations is the operating window. Fig. 7.11 shows the achievable current density ranges by variation of the membrane thickness at four different pressure levels.

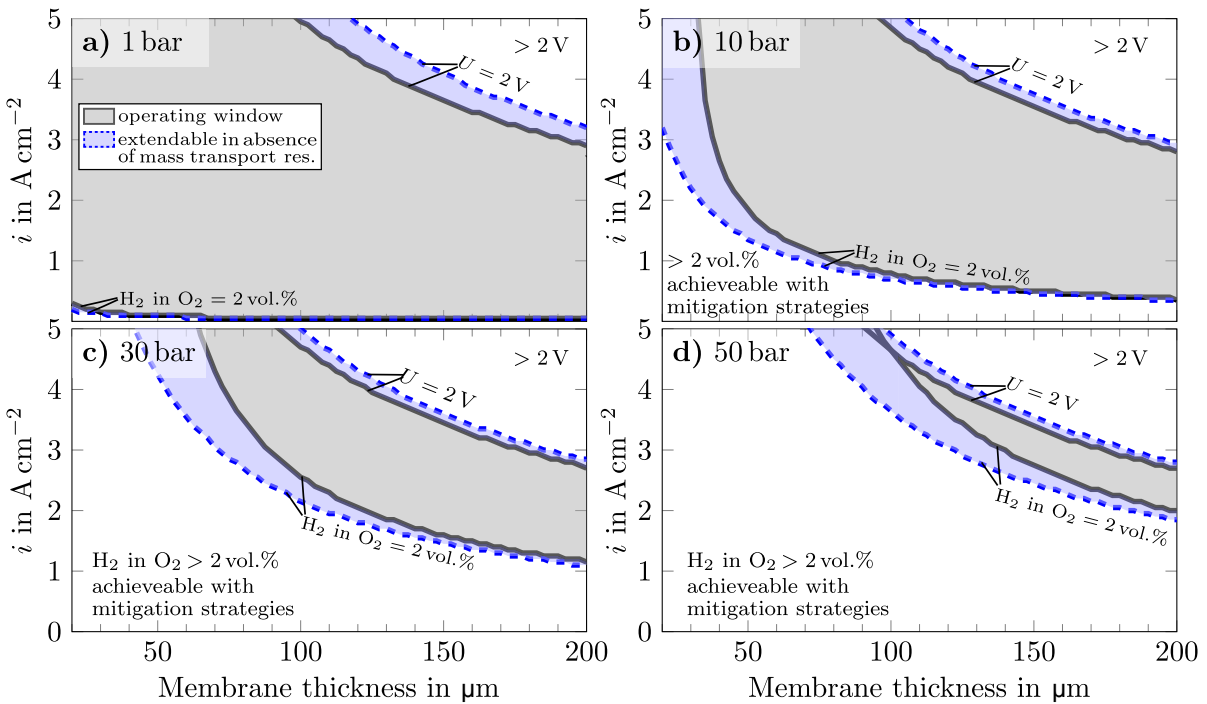


Figure 7.11: Operating window by variation of the membrane thickness at four cathode pressures: a) 1 bar, b) 10 bar, c) 30 bar and d) 50 bar. Operational limits are set to 2 V and 2 vol.% H₂ in O₂. The area between the resulting maximal and minimal current density is the operating window. Solid lines represent the cases with mass transfer resistances (supersaturation) and dashed lines in the absence of mass transport resistances.

It can be seen that especially at high pressures and for thin membranes the operating window is strongly reduced (Fig. 7.11d)). Particularly, this is caused by the safety issue due to hydrogen crossover.

Furthermore, Fig. 7.11 shows the effect of mass transfer resistances. The solid lines are calculated with the full model (including mass transfer resistances), whereas the dashed lines are calculated by assuming no mass transfer resistances. For this purpose, the mass transfer coefficient was multiplied by a factor of 10^8 to disable the mass transfer losses, as done already within section 7.1. As previously discussed, the mass transfer resistances lead to supersaturated dissolved gas concentrations within both catalyst layers. Consequently, mass transport resistances lead to performance decreases and gas crossover increases, which also leads to a smaller operating window. Fig. 7.11 shows the importance of a proper design of catalyst layers and porous transport layers to reduce mass transfer resistances. This enables higher efficiencies and also larger operating windows. Nevertheless, Fig. 7.11 shows that even without any mass transport resistances, mitigation strategies are essential for an operation at high pressures and thin membranes to overcome the safety issues.

7.6 Concluding Remarks

In context of RQ 5 the one-dimensional model, which is presented in ch. 6, is used to investigate different effects in more detail. The model results confirmed that the temperature increase and local pressure enhancement are not strong enough to explain the crossover increase with current density and also have only small effects on cell voltage. Whereas, the supersaturation of dissolved gases due to mass transfer resistances can explain the experimental findings very well. These mass transfer resistances are considered as the diffusion process of dissolved gases from the catalyst particles to the pore volume within the ionomer water, which is parameterized by literature data. In contrast to the local pressure enhancement, this approach can explain the almost constant increase of gas crossover with current density at different pressures.

Although, the mass transport losses are small in comparison to the kinetic losses and proton transport losses of the membrane, they can not be neglected. The same applies for the protonic losses within both catalyst layers, especially at high current densities. The model helps to understand the complex interplay between mass transport, ohmic and kinetic losses within the catalyst layers. The focus is not only to reduce kinetic losses or ohmic losses or protonic losses, but the sum of these to find the optimal catalyst structures. For example structural changes, e.g. the variation of the catalyst ionomer content, have strong influences on the mass transfer resistances and consequently on the supersaturation of dissolved gases and hence on gas crossover and cell voltage. It could be shown in detail that optimal ionomer contents reduce crossover and cell voltage. Furthermore, the optimal ionomer content is also depending on current density. This finding might lead to specifically designed catalyst layer according to the application (operating conditions: pressure, current density). Therefore, it is important to investigate the mass transport mechanisms in more detail and the effects of further structural changes,

as catalyst thickness, catalyst loading, catalyst particle diameter or gradients.

The final considerations to the cell efficiency and operating window show that the Faraday efficiency has a strong impact on the overall cell efficiency, especially for thin membranes and high cathode pressures, but also at high balanced pressure conditions due to the increased oxygen crossover and hence increased recombination of permeated oxygen with hydrogen at the cathode side. Depending on operating conditions, such as pressure levels and current densities, different membrane thicknesses achieve the highest cell efficiencies. This means again that the applied cell setup has to be specifically designed to the corresponding application (operating conditions).

However, the anodic hydrogen in oxygen content lead to relevant safety issues, so that the most efficient operating points could not be operated safely at all. One important aspect here is also to reduce the mass transfer resistances in order to reduce the safety issue and increase the performance, but this will not be sufficient without additional mitigation strategies. Consequently, it is very important to research and develop suitable mitigation strategies to overcome the safety problems, but also to improve the cell efficiency and reduce degradation.

8 Summary, Conclusion and Outlook

Focus of the present work is the investigation and understanding of gas crossover during PEM water electrolyzers operation. For this purpose, experiments at various operating conditions and for different catalyst structures were carried out. Based on the experimental findings an one-dimensional, physically meaningful model is formulated, enabling the investigation of the underlying mechanisms regarding gas crossover as well as cell voltage in more detail. In the following, the results and conclusions are summarized by answering the research questions formulated at the beginning of this work.

Research Question 1: *“What are the effects of different operating conditions on the increase of hydrogen crossover with current density?”*

This question is examined in section 4.1. The available literature results show a strong crossover increase with current density. However, the slopes of this crossover increase according to the literature data differ significantly (s. Fig. 4.1). One reason for these differences could be the different operating conditions. To investigate this in more detail the anodic hydrogen in oxygen content was measured during PEM water electrolysis at different temperatures between 30 and 80 °C and cathode pressures in a range of 1 to 31 bar. The corresponding hydrogen crossover fluxes of this work show strong, linear increases with current density. These crossover increases are steeper at higher temperatures, whereas the crossover increase with current density is almost independent of pressure (s. Fig. 4.2 and 4.3). This means that the underlying mechanisms of the crossover increase also have to be independent of pressure. This finding rebuts the most prominent literature explanatory approach that the gas crossover increases due to local pressure enhancements. Since gas transport is strongly dependent on pressure, the crossover increase with current density should decrease at higher pressures. This is also discussed within the critical considerations to possible explanation approaches (s. sec. 2.3).

Neither the local pressure enhancement, nor a raise in temperature with increasing current density are significant or even cannot explain the experimental findings qualitatively. Additionally, there is no evidence for structural changes of the ionomer during PEM water electrolysis, which could explain the crossover increases (s. sec. 2.3).

Research Question 2: *“Which alternative theory can be formulated to explain the current density dependence?”*

This research question is discussed in section 4.2. The most probable explanation of the hydrogen crossover increase with current density is the supersaturation of dissolved hydrogen due to a limited hydrogen mass transfer from the cathode catalyst layer towards the cathode outlet. The previous experimental finding that the crossover increases with

current density is almost independent of pressure leads to the assumption that the relevant mass transfer limitations are also pressure independent. Therefore, the diffusive transport of dissolved hydrogen from the catalyst particles through the ionomer/water films towards the pore space is the most evident transport step, since the diffusion coefficient of dissolved gases in water is pressure independent.

Consequently, this theory can explain the almost pressure independent correlation and it is further supported by literature measurements of supersaturated dissolved gas concentrations. A rough supersaturation model shows that mass transfer coefficients in the order of $1 \cdot 10^{-3} \text{ m s}^{-1}$ are required to explain the strong crossover increases with current density (s. Fig. 4.5). Even lower mass transfer coefficients can be found for comparable systems in the literature. Consequently, it can be concluded that this theory is a promising explanatory approach. It seems likely that this supersaturation effect also occurs on the anode side with dissolved oxygen.

Research Question 3: *“Is the oxygen crossover also influenced by current density?”*

Unfortunately, the oxygen crossover cannot be measured as simple as the hydrogen crossover, since the permeating oxygen recombines with evolved hydrogen to water at the cathodic state-of-the-art catalyst, Pt. For this experimental investigation (sec. 4.3), a special cathode catalyst material is used that has a low activity towards the oxygen reduction reaction and thus probably also to the recombination reaction of oxygen with hydrogen to water.

Using the Pt-free catalyst results in significant higher oxygen in hydrogen contents of the cathodic product gas compared to a measurement series with Pt (s. Fig. 4.7). The calculated oxygen crossover fluxes reveal also strong linear increases with current density. However, at small current densities the calculated crossover fluxes are below the theoretical oxygen crossover. This leads to the assumption that oxygen still recombines with hydrogen to water at the cathode. Due to this uncertainty the oxygen crossover is not further analyzed in this work, since the main focus lies on the investigation of the hydrogen crossover. Nevertheless, the oxygen crossover represents also a very important research topic due to degradation issues, impurity of the hydrogen product gas and Faraday losses due to the recombination reaction.

Research Question 4: *“What is the influence of the electrode structure on the current density effect on gas crossover”*

The comparison of crossover increases with current density according to literature data and the experimental results of this work reveal strong differences of the slopes. In the context of the experiments according to RQ 1, the operating conditions can be excluded to explain these differences. Another reason could be the material variation, e. g. different membranes or catalyst layers. According to the alternative supersaturation theory of RQ 2 it is considered that the mass transfer resistances mainly originate from the ionomer film within the catalyst layers. Therefore, in chapter 5 an experimental variation of the ionomer content within the cathode catalyst layer is carried out to examine the effect of

different electrode structures on the current density effect on gas crossover.

The cathode ionomer content was varied between 10 and 40 wt.%. For the observed range of the cathode ionomer content, the hydrogen crossover increases with increasing ionomer content. Consequently, the electrodes with higher ionomer contents have higher mass transfer resistances. All manufactured cathode catalyst layers have almost the same thickness. This means that the ionomer fraction within the catalyst layer is increased and thus leads to thicker ionomer films, which is the reason for the increased mass transfer resistances, increased hydrogen crossover, respectively.

Additionally, the polarization behavior of the different electrodes is investigated (s. sec. 5.3). It can be seen that the cell voltage increases with increasing ionomer content within the observed range also. Based on the crossover measurements, the supersaturated dissolved hydrogen concentration can be calculated. Due to this additional information the mass transport losses within the cathode side can be estimated by the Nernst equation. The correction of the cell voltage by the calculated mass transport losses leads to quite comparable polarization curves (s. Fig. 5.6). Consequently, the major part of the cell voltage differences can be explained by the different mass transport losses that are determined via the crossover measurement.

These mass transport losses are still part of the iR -free cell voltage. Therefore, by carrying out a Tafel analysis from iR -free cell voltage, kinetic parameters may contain mass transport effects, even at low current densities. Consequently, measurements of hydrogen crossover can be used to determine mass transport losses, contribute to a comprehensive breakdown of overpotential sources and improve the determination of kinetic parameters by the Tafel analysis.

These findings highlight the importance of the catalyst layer structure. Not only in the context of electrochemical activity, but also related to a reduction of mass transfer resistances, which reduce the supersaturation and thus improve the cell performance as well as decrease the crossover. The ionomer content is one key parameter, among several others, e.g. catalyst loading, which could also be changed to reduce the electrode mass transfer resistance of catalyst layers. It is important to investigate the different mass transport/transfer steps in more detail for systematic development of improved catalyst layers.

Research Question 5: *“How can the current density influence on gas crossover be described adequately by a physically meaningful model? How can the developed model help to analyze the observed effects in more detail?”*

The first part of the fifth research question is addressed in chapter 6. It contains the formulation of the physically meaningful model in through plane direction of a common five layer PEM water electrolysis cell setup. This comprehensive model includes the description of the electron and proton potentials, the dissolved gas (hydrogen and oxygen) and dissolved water concentrations, the two-phase flow of liquid water and gases (hydrogen, oxygen, water vapor) and temperature. Special focus is on the transport of dissolved gases within the catalyst layers and membrane to implement the supersaturation theory of section 4.2. This model is only parameterized by data from literature without

any fitting parameters. The model results according to the base case parameter set can be validated by the experimental results.

The ability to investigate the local profiles allows a detailed view of different effects. Particularly important is the profile of the production rate (s. Fig. 6.8a)). The gas production rate is very high directly at the membrane interface, due to the low proton conductivity in comparison to the electric conductivity within the CL. This leads to increased dissolved gas concentrations, half-cell potentials and activation overpotentials directly at the membrane interface and consequently is one reason of the crossover increase with current density.

In chapter 7 the second part of the last research question is discussed. It includes the investigation of i) the influence of the different transport mechanisms on gas crossover and cell voltage, ii) a complete voltage loss breakdown, iii) the effect of a pressure variation, iv) the detailed investigation of the variation of the ionomer content and v) system considerations according gas crossover.

The model results confirmed that the effects of temperature increase and local pressure enhancement are too small to explain the crossover increase with current density and also have only small effects on cell voltage. Instead, the supersaturation of dissolved gases due to mass transfer resistances can explain the experimental findings very well.

Although the mass transport losses are small in comparison to the kinetic and proton transport losses within the membrane, they cannot be neglected. The same applies for protonic losses within both catalyst layers, especially at high current densities. The model helps to understand the complex interaction between mass transport, ohmic and kinetic losses within the catalyst layers. The focus is not to reduce each of these losses alone, but the sum of these to find optimal catalyst structures. For example, structural changes, e.g. the variation of the catalyst ionomer content, have strong influence on the mass transfer resistances and consequently on the supersaturation of dissolved gases and hence on gas crossover and cell voltage. It is shown in detail that optimal ionomer contents reduce crossover and cell voltage.

Furthermore, the optimal ionomer content also depends on current density. This finding might lead to specifically designed catalyst layers according to the application influenced by the operating conditions: pressure, current density. Therefore, it is important to investigate the mass transport mechanisms in more detail and the effects of further structural changes, such as the catalyst layer thickness, catalyst loading, catalyst particle diameter or gradients.

The final considerations to the cell efficiency and operating window show that the Faraday efficiency has a strong impact on the overall cell efficiency, especially for thin membranes and high cathode pressures, but also at high balanced pressure conditions due to the increased oxygen crossover and hence increased recombination of permeated oxygen with hydrogen at the cathode side. Different membrane thicknesses achieve the highest cell efficiencies, depending on operating conditions, such as pressure levels and current densities. This means again that the applied cell setup has to be specifically designed to the corresponding application.

The findings and conclusions described above form the basis for further investigations. Following, three important research questions are identified and described below.

Further Research Question I: *“What are possible gas crossover mitigation strategies? Which are the most suitable strategies according to different applications?”*

It is clearly shown that the anodic hydrogen in oxygen content leads to relevant safety issues. Following, the most efficient operating points cannot be operated safely. One important aspect is also to reduce the mass transfer resistances in order to reduce the safety issue and increase the performance, but this will not be sufficient without additional mitigation strategies. Consequently, it is very important to research and develop suitable mitigation strategies to overcome the safety problems, but also to improve the cell efficiency and reduce degradation.

Further Research Question II: *“What are the separate mass transfer steps? Which transfer steps are the dominant ones and how can they be optimized?”*

Within this work integral mass transfer coefficients are experimentally determined. For the model the mass transfer coefficients are considered by the transport of dissolved gas from the catalyst particles towards the gas phase through the ionomer. However, there are various other possible steps that could lead to distinct mass transfer resistances (cf. Fig. 4.4). Additionally, it is important to investigate how the separate mass transfer steps contribute to the integral coefficient. Therefore, the separate steps have to be investigated in more detail to further optimize the catalyst structures.

Further Research Question III: *“How is it possible to measure the complete oxygen crossover during PEM water electrolysis? What are the effects of the oxygen crossover?”*

The oxygen crossover is an important research topic due to degradation mechanisms, impurity of the hydrogen product gas and Faraday losses. So far, this is not addressed adequately, especially during PEM water electrolysis operation.

References

- [1] G. R. Shaver, J. Canadell, F. S. Chapin, J. Gurevitch, J. Harte, G. Henry, P. Ineson, S. Johansson, J. Melilo, L. S. Pitelka, and L. Rustad. Global Warming and Terrestrial Ecosystems: A Conceptual Framework for Analysis. *BioScience*, 50(10):871, 2000.
- [2] C. Boano, R. Zetter, and T. Moris. Environmentally Displaced People: Understanding the linkages between environmental change, livelihoods and forced migration, 2008.
- [3] Paris Agreement, FCCC/CP/2015/L.9/Rev.1, <https://unfccc.int/resource/docs/2015/cop21/eng/109r01.pdf>, last access: 10.12.2019.
- [4] T. Klaus, A. Vollmer, K. Werner, H. Lehmann, and K. Müschen. Energieziel 2050: 100% Strom aus erneuerbaren Quellen, 2010.
- [5] F. Petersen, L. Bühre, R. Niepelt, R. Brendel, and R. Hanke-Rauschenbach. Wasserstoff als Energieträger und Rohstoff - Wirkung auf das Gesamtenergiesystem, 5.11.2019.
- [6] R. Elder, D. Cumming, and M. B. Mogensen. High Temperature Electrolysis. In P. Styring, E. A. Quadrelli, and K. Armstrong, editors, *Carbon dioxide utilisation*, pages 183–209. Elsevier, Amsterdam and Boston and Heidelberg, 2015.
- [7] T. Smolinka. FUELS – HYDROGEN PRODUCTION | Water Electrolysis. In J. Garche, editor, *Encyclopedia of electrochemical power sources*, pages 394–413. Elsevier, Amsterdam, 2009.
- [8] M. Carmo, D. L. Fritz, J. Mergel, and D. Stolten. A comprehensive review on PEM water electrolysis. *Int. J. Hydrogen Energ.*, 38(12):4901–4934, 2013.
- [9] *PEM ELECTROLYSIS FOR HYDROGEN PRODUCTION: Principles and applications*. CRC Press, 2017.
- [10] U. Babic, M. Suermann, F. N. Büchi, L. Gubler, and T. J. Schmidt. Critical Review—Identifying Critical Gaps for Polymer Electrolyte Water Electrolysis Development. *J. Electrochem. Soc.*, 164(4):F387–F399, 2017.
- [11] S. A. Grigoriev, P. Millet, S. V. Korobtsev, V. I. Porembskiy, M. Pepic, C. Etievant, C. Puyenchet, and V. N. Fateev. Hydrogen safety aspects related to high-pressure polymer electrolyte membrane water electrolysis. *Int. J. Hydrogen Energ.*, 34(14):5986–5991, 2009.
- [12] S. A. Grigoriev, V. I. Porembskiy, S. V. Korobtsev, V. N. Fateev, F. Auprêtre, and P. Millet. High-pressure PEM water electrolysis and corresponding safety issues. *Int. J. Hydrogen Energ.*, 36(3):2721–2728, 2011.
- [13] M. Schalenbach, M. Carmo, D. L. Fritz, J. Mergel, and D. Stolten. Pressurized PEM water electrolysis: Efficiency and gas crossover. *Int. J. Hydrogen Energ.*, 38(35):14921–14933, 2013.
- [14] H. Ito, N. Miyazaki, M. Ishida, and A. Nakano. Cross-permeation and consumption of hydrogen during proton exchange membrane electrolysis. *Int. J. Hydrogen Energ.*, 41(45):20439–20446, 2016.
- [15] M. Chandesris, V. Médeau, N. Guillet, S. Chelghoum, D. Thoby, and F. Fouda-Onana. Membrane degradation in PEM water electrolyzer: Numerical modeling and experimental evidence of the influence of temperature and current density. *Int. J. Hydrogen Energ.*, 40(3):1353–1366, 2015.
- [16] S. H. Frensch, G. Serre, F. Fouda-Onana, H. C. Jensen, M. L. Christensen, S. S. Araya, and S. K. Kær. Impact of iron and hydrogen peroxide on membrane degradation for polymer electrolyte membrane water electrolysis: Computational and experimental investigation on fluoride emission. *J. Power Sources*, 420:54–62, 2019.

- [17] H. Janssen. Safety-related studies on hydrogen production in high-pressure electrolyzers. *Int. J. Hydrogen Energ.*, 29(7):759–770, 2004.
- [18] P. Trinke, P. Haug, J. Brauns, B. Bensmann, R. Hanke-Rauschenbach, and T. Turek. Hydrogen Crossover in PEM and Alkaline Water Electrolysis: Mechanisms, Direct Comparison and Mitigation Strategies. *J. Electrochem. Soc.*, 165(7):F502–F513, 2018.
- [19] D. G. Bessarabov and P. Millet. *PEM water electrolysis: Volume 1*. Hydrogen and fuel cells primer series. Academic Press an imprint of Elsevier, London, United Kingdom, 2018.
- [20] S. Shiva Kumar and V. Himabindu. Hydrogen production by PEM water electrolysis – A review. *Mat. Sci. Energ. Tech.*, 2(3):442–454, 2019.
- [21] Qi Feng, Xiao–Zi Yuan, G. Liu, B. Wei, Z. Zhang, H. Li, and H. Wang. A review of proton exchange membrane water electrolysis on degradation mechanisms and mitigation strategies. *J. Power Sources*, 366:33–55, 2017.
- [22] S. A. Grigoriev, D. G. Bessarabov, and V. N. Fateev. Degradation mechanisms of MEA characteristics during water electrolysis in solid polymer electrolyte cells. *Russ. J. Electrochem.*, 53(3):318–323, 2017.
- [23] M. Bernt and H. A. Gasteiger. Influence of Ionomer Content in IrO₂/TiO₂ Electrodes on PEM Water Electrolyzer Performance. *J. Electrochem. Soc.*, 163(11):F3179–F3189, 2016.
- [24] C. Immerz, M. Schweins, P. Trinke, B. Bensmann, M. Paidar, T. Bystrůň, K. Bouzek, and R. Hanke-Rauschenbach. Experimental characterization of inhomogeneity in current density and temperature distribution along a single-channel PEM water electrolysis cell. *Electrochim. Acta*, 260:582–588, 2018.
- [25] J. Nie and Y. Chen. Numerical modeling of three-dimensional two-phase gas–liquid flow in the flow field plate of a PEM electrolysis cell. *Int. J. Hydrogen Energ.*, 35(8):3183–3197, 2010.
- [26] J. O. Majasan, J. I.S. Cho, I. Dedigama, D. Tsaoulidis, P. Shearing, and D. J. L. Brett. Two-phase flow behaviour and performance of polymer electrolyte membrane electrolyzers: Electrochemical and optical characterisation. *Int. J. Hydrogen Energ.*, 43(33):15659–15672, 2018.
- [27] E. T. Ojong. *Characterization of the performance of PEM water electrolysis cells operating with and without flow channels, based on experimentally validated semi-empirical coupled-physics models*. BTU Cottbus - Senftenberg, Cottbus, 2018.
- [28] P. Lettenmeier, S. Kolb, N. Sata, A. Fallisch, L. Zielke, S. Thiele, A. S. Gago, and K. A. Friedrich. Comprehensive investigation of novel pore-graded gas diffusion layers for high-performance and cost-effective proton exchange membrane electrolyzers. *Energy Environ. Sci.*, 10(12):2521–2533, 2017.
- [29] M. Langemann, D. L. Fritz, M. Müller, and D. Stolten. Validation and characterization of suitable materials for bipolar plates in PEM water electrolysis. *Int. J. Hydrogen Energ.*, 40(35):11385–11391, 2015.
- [30] K. E. Ayers, E. B. Anderson, C. Capuano, B. Carter, L. Dalton, G. Hanlon, J. Manco, and M. Niedzwiecki. Research Advances towards Low Cost, High Efficiency PEM Electrolysis. ECS Transactions, pages 3–15. ECS, 2010.
- [31] A. S. Gago, S. A. Ansar, B. Saruhan, U. Schulz, P. Lettenmeier, N. A. Cañas, P. Gazdzicki, T. Morawietz, R. Hiesgen, J. Arnold, and K. A. Friedrich. Protective coatings on stainless steel bipolar plates for proton exchange membrane (PEM) electrolyzers. *J. Power Sources*, 307:815–825, 2016.
- [32] P. Lettenmeier, R. Wang, R. Abouatallah, B. Saruhan, O. Freitag, P. Gazdzicki, T. Morawietz, R. Hiesgen, A. S. Gago, and K. A. Friedrich. Low-Cost and Durable Bipolar Plates for Proton Exchange Membrane Electrolyzers. *Sci. Rep.-UK*, 7:44035, 2017.

- [33] S. S. Dhirab, K. Sopian, M. A. Alghoul, and M. Y. Sulaiman. Review of the membrane and bipolar plates materials for conventional and unitized regenerative fuel cells. *Renew. Sust. Energ. Rev.*, 13(6-7):1663–1668, 2009.
- [34] F. Barbir. *PEM fuel cells: Theory and practice*. Elsevier/Academic Press, Amsterdam and Boston, 2nd ed. edition, 2013.
- [35] E. Tal-Gutelmacher and D. Eliezer. The hydrogen embrittlement of titanium-based alloys. *JOM-US*, 57(9):46–49, 2005.
- [36] T. Smolinka, E. T. Ojong, and J. Garche. Hydrogen Production from Renewable Energies—Electrolyzer Technologies. In J. Garche, P. T. Moseley, and P. Adelmann, editors, *Electrochemical energy storage for renewable sources and grid balancing*, pages 103–128. Elsevier, Amsterdam, Netherlands, 2015.
- [37] M. Suermann, K. Takanohashi, A. Lamibrac, T. J. Schmidt, and F. N. Büchi. Influence of Operating Conditions and Material Properties on the Mass Transport Losses of Polymer Electrolyte Water Electrolysis. *J. Electrochem. Soc.*, 164(9):F973–F980, 2017.
- [38] A. El-Kharouf, T. J. Mason, D. J. L. Brett, and B. G. Pollet. Ex-situ characterisation of gas diffusion layers for proton exchange membrane fuel cells. *J. Power Sources*, 218:393–404, 2012.
- [39] S. El Oualid, R. Lachat, D. Candusso, and Y. Meyer. Characterization process to measure the electrical contact resistance of Gas Diffusion Layers under mechanical static compressive loads. *Int. J. Hydrogen Energ.*, 42(37):23920–23931, 2017.
- [40] C. Lim and C. Y. Wang. Effects of hydrophobic polymer content in GDL on power performance of a PEM fuel cell. *Electrochim. Acta*, 49(24):4149–4156, 2004.
- [41] T. van Nguyen, A. Ahosseini, X. Wang, V. Yarlagadda, A. Kwong, A. Z. Weber, P. Deevanhxay, S. Tsushima, and S. Hirai. Hydrophobic Gas-Diffusion Media for Polymer-Electrolyte Fuel Cells by Direct Fluorination. *J. Electrochem. Soc.*, 162(14):F1451–F1460, 2015.
- [42] C. H. Lee, R. Banerjee, F. Arbabi, J. Hinebaugh, and A. Bazylak. Porous Transport Layer Related Mass Transport Losses in Polymer Electrolyte Membrane Electrolysis: A Review. In *Proceedings of the ASME 14th International Conference on Nanochannels, Microchannels, and Minichannels - 2016*, New York, N.Y., 2016. The American Society of Mechanical Engineers.
- [43] J. K. Lee, C. H. Lee, and A. Bazylak. Pore network modelling to enhance liquid water transport through porous transport layers for polymer electrolyte membrane electrolyzers. *J. Power Sources*, 437:226910, 2019.
- [44] P. Lettenmeier, S. Kolb, F. Burggraf, A. S. Gago, and K. A. Friedrich. Towards developing a backing layer for proton exchange membrane electrolyzers. *J. Power Sources*, 311:153–158, 2016.
- [45] J. O. Majasan, F. Iacoviello, P. R. Shearing, and D. J. L. Brett. Effect of Microstructure of Porous Transport Layer on Performance in Polymer Electrolyte Membrane Water Electrolyser. *Engng. Proced.*, 151:111–119, 2018.
- [46] C. Liu, M. Carmo, G. Bender, A. Everwand, T. Lickert, J. L. Young, T. Smolinka, D. Stolten, and W. Lehnert. Performance enhancement of PEM electrolyzers through iridium-coated titanium porous transport layers. *Electrochem. Commun.*, 97:96–99, 2018.
- [47] E. Oakton, D. Lebedev, M. Povia, D. F. Abbott, E. Fabbri, A. Fedorov, M. Nachttegaal, C. Copéret, and T. J. Schmidt. IrO₂-TiO₂: A High-Surface-Area, Active, and Stable Electrocatalyst for the Oxygen Evolution Reaction. *ACS Catal.*, 7(4):2346–2352, 2017.
- [48] L. Ma, S. Sui, and Y. Zhai. Investigations on high performance proton exchange membrane water electrolyzer. *Int. J. Hydrogen Energ.*, 34(2):678–684, 2009.

- [49] S. Siracusano, V. Baglio, N. van Dijk, L. Merlo, and A. S. Aricò. Enhanced performance and durability of low catalyst loading PEM water electrolyser based on a short-side chain perfluorosulfonic ionomer. *Appl. Energ.*, 192:477–489, 2017.
- [50] M. H. Miles. Periodic Variations of Overvoltages for Water Electrolysis in Acid Solutions from Cyclic Voltammetric Studies. *J. Electrochem. Soc.*, 123(10):1459, 1976.
- [51] S. Cherevko, S. Geiger, O. Kasian, N. Kulyk, J.-P. Grote, A. Savan, B. R. Shrestha, S. Merzlikin, B. Breitbach, A. Ludwig, and K. J.J. Mayrhofer. Oxygen and hydrogen evolution reactions on Ru, RuO₂, Ir, and IrO₂ thin film electrodes in acidic and alkaline electrolytes: A comparative study on activity and stability. *Catal. Today*, 262:170–180, 2016.
- [52] M. Bernt, A. Siebel, and H. A. Gasteiger. Analysis of Voltage Losses in PEM Water Electrolyzers with Low Platinum Group Metal Loadings. *J. Electrochem. Soc.*, 165(5):F305–F314, 2018.
- [53] R. Wu, J. Zhang, Y. Shi, D. Liu, and B. Zhang. Metallic WO₂-Carbon Mesoporous Nanowires as Highly Efficient Electrocatalysts for Hydrogen Evolution Reaction. *J. Am. Chem. Soc.*, 137(22):6983–6986, 2015.
- [54] W.-F. Chen, C.-H. Wang, K. Sasaki, N. Marinkovic, W. Xu, J. T. Muckerman, Y. Zhu, and R. R. Adzic. Highly active and durable nanostructured molybdenum carbide electrocatalysts for hydrogen production. *Energy Environ. Sci.*, 6(3):943, 2013.
- [55] N. H. Jalani, K. Dunn, and R. Datta. Synthesis and characterization of Nafion®-MO₂ (M=Zr, Si, Ti) nanocomposite membranes for higher temperature PEM fuel cells. *Electrochim. Acta*, 51(3):553–560, 2005.
- [56] A. D’Epifanio, M. A. Navarra, F. C. Weise, B. Mecheri, J. Farrington, S. Licocchia, and S. Greenbaum. Composite Nafion/sulfonated zirconia membranes: effect of the filler surface properties on proton transport characteristics. *Chem. Mater.*, 22(3):813–821, 2010.
- [57] A. M. Baker, L. Wang, W. B. Johnson, A. K. Prasad, and S. G. Advani. Nafion Membranes Reinforced with Ceria-Coated Multiwall Carbon Nanotubes for Improved Mechanical and Chemical Durability in Polymer Electrolyte Membrane Fuel Cells. *J. Phys. Chem. C*, 118(46):26796–26802, 2014.
- [58] F. A. de Bruijn, R. C. Makkus, R. K.A.M. Mallant, and G. J.M. Janssen. Materials for State-of-the-Art PEM Fuel Cells, and Their Suitability for Operation Above 100°C. In K.-D. Kreuer, T. van Nguyen, and T. Zhao, editors, *Advances in Fuel Cells*, volume 1 of *Advances in Fuel Cells*, pages 235–336. Elsevier professional, s.l., 2007.
- [59] A. Albert, A. O. Barnett, M. S. Thomassen, T. J. Schmidt, and L. Gubler. Radiation-Grafted Polymer Electrolyte Membranes for Water Electrolysis Cells: Evaluation of Key Membrane Properties. *ACS Appl. Mater. Inter.*, 7(40):22203–22212, 2015.
- [60] C. K. Mittelstaedt and J. A. Staser. Electrolyzer Membranes. In K. Matyjaszewski and M. Möller, editors, *Polymer science*, pages 849–871. Elsevier, Amsterdam, 2012.
- [61] J. A. Kerres. Design Concepts for Aromatic Ionomers and Ionomer Membranes to be Applied to Fuel Cells and Electrolysis. *Polym. Rev.*, 55(2):273–306, 2015.
- [62] K.-D. Kreuer, A. Rabenau, and W. Weppner. Vehicle Mechanism, A New Model for the Interpretation of the Conductivity of Fast Proton Conductors. *Angew. Chem. Int. Edit.*, 21(3):208–209, 1982.
- [63] G. A. Ludueña, T. D. Kühne, and D. Sebastiani. Mixed Grotthuss and Vehicle Transport Mechanism in Proton Conducting Polymers from Ab initio Molecular Dynamics Simulations. *Chem. Mater.*, 23(6):1424–1429, 2011.
- [64] T. A. Zawodzinski. Water Uptake by and Transport Through Nafion® 117 Membranes. *J. Electrochem. Soc.*, 140(4):1041, 1993.

- [65] Y. Sone. Proton Conductivity of Nafion 117 as Measured by a Four-Electrode AC Impedance Method. *J. Electrochem. Soc.*, 143(4):1254, 1996.
- [66] H. Ito, T. Maeda, A. Nakano, and H. Takenaka. Properties of Nafion membranes under PEM water electrolysis conditions. *Int. J. Hydrogen Energ.*, 36(17):10527–10540, 2011.
- [67] S. Shi, A. Z. Weber, and A. Kusoglu. Structure/property relationship of Nafion XL composite membranes. *J. Membrane Sci.*, 516:123–134, 2016.
- [68] L. Bertuccioli, A. Chan, D. Hart, F. Lehner, B. Madden, and E. Standen. Study on Development of Water Electrolysis in the EU, 2014.
- [69] A. J. Bard and L. R. Faulkner. *Electrochemical methods: Fundamentals and applications*. Wiley, Hoboken, NJ, 2. ed. edition, 2001.
- [70] J. O’M. Bockris, A. K. N. Reddy, and M. Gamboa-Aldeco. *Modern Electrochemistry 2A: Fundamentals of Electrodeics*. Kluwer Academic Publishers, Boston, MA, 2 edition, 2002.
- [71] C. Immerz, B. Bensmann, P. Trinke, M. Suermann, and R. Hanke-Rauschenbach. Local Current Density and Electrochemical Impedance Measurements within 50 cm Single-Channel PEM Electrolysis Cell. *J. Electrochem. Soc.*, 165(16):F1292–F1299, 2018.
- [72] Petr Mazúr, J. Polonský, M. Paidar, and K. Bouzek. Non-conductive TiO₂ as the anode catalyst support for PEM water electrolysis. *Int. J. Hydrogen Energ.*, 37(17):12081–12088, 2012.
- [73] M. Suermann, T. J. Schmidt, and F. N. Büchi. Cell Performance Determining Parameters in High Pressure Water Electrolysis. *Electrochim. Acta*, 211:989–997, 2016.
- [74] G. de Moor, N. Charvin, C. Bas, N. Caque, E. Rossinot, and L. Flandin. *In Situ* Quantification of Electronic Short Circuits in PEM Fuel Cell Stacks. *IEEE Ind. Electron.*, 62(8):5275–5282, 2015.
- [75] T. Sakai. Gas Permeation Properties of Solid Polymer Electrolyte (SPE) Membranes. *J. Electrochem. Soc.*, 132(6):1328, 1985.
- [76] M. H. Eikerling and P. Berg. Poroelastoelectroelastic theory of water sorption and swelling in polymer electrolyte membranes. *Soft Matter*, 7(13):5976, 2011.
- [77] T. Sakai. Gas Diffusion in the Dried and Hydrated Nafions. *J. Electrochem. Soc.*, 133(1):88, 1986.
- [78] M. Schalenbach, T. Hoefner, P. Paciok, M. Carmo, W. Lueke, and D. Stolten. Gas Permeation through Nafion. Part 1: Measurements. *J. Phys. Chem. C*, 119(45):25145–25155, 2015.
- [79] R. B. Bird, W. E. Stewart, and E. N. Lightfoot. *Transport phenomena*. Wiley, New York, NY, 2. ed. edition, 2002.
- [80] F. Marangio, M. Santarelli, and M. Cali. Theoretical model and experimental analysis of a high pressure PEM water electrolyser for hydrogen production. *Int. J. Hydrogen Energ.*, 34(3):1143–1158, 2009.
- [81] H. Kim, M. Park, and K. S. Lee. One-dimensional dynamic modeling of a high-pressure water electrolysis system for hydrogen production. *Int. J. Hydrogen Energ.*, 38(6):2596–2609, 2013.
- [82] Ross Taylor and R. Krishna. *Multicomponent mass transfer*. Wiley series in chemical engineering. Wiley, New York, 1993.
- [83] M. Lindstrom and B. Wetton. A comparison of Fick and Maxwell–Stefan diffusion formulations in PEMFC gas diffusion layers. *Heat Mass Transfer*, 53(1):205–212, 2017.
- [84] J. Fimrite, B. Carnes, H. Struchtrup, and N. Djilali. Transport Phenomena in Polymer Electrolyte Membranes. *J. Electrochem. Soc.*, 152(9):A1815, 2005.

- [85] R. B. Evans, G. M. Watson, and E. A. Mason. Gaseous Diffusion in Porous Media at Uniform Pressure. *J. Chem. Phys.*, 35(6):2076–2083, 1961.
- [86] P. Trinke, B. Bensmann, S. Reichstein, R. Hanke-Rauschenbach, and K. Sundmacher. Hydrogen Permeation in PEM Electrolyzer Cells Operated at Asymmetric Pressure Conditions. *J. Electrochem. Soc.*, 163(11):F3164–F3170, 2016.
- [87] C. L. Young, editor. *Hydrogen and deuterium*, volume 5/6 of *Solubility data series*. Pergamon Press, Oxford, 1981.
- [88] R. Wiebe and V. L. Gaddy. The Solubility of Hydrogen in Water at 0, 50, 75 and 100° from 25 to 1000 Atmospheres. *J. Am. Chem. Soc.*, 56(1):76–79, 1934.
- [89] D. R. Stull. Vapor Pressure of Pure Substances. Organic and Inorganic Compounds. *Ind. Eng. Chem.*, 39(4):517–540, 1947.
- [90] S. A. Grigoriev, A. A. Kalinnikov, P. Millet, V. I. Poremsky, and V. N. Fateev. Mathematical modeling of high-pressure PEM water electrolysis. *J. Appl. Electrochem.*, 40(5):921–932, 2010.
- [91] P. Medina and M. Santarelli. Analysis of water transport in a high pressure PEM electrolyzer. *Int. J. Hydrogen Energy*, 35(11):5173–5186, 2010.
- [92] M. Mulder. *Basic Principles of Membrane Technology*. Springer Netherlands, Dordrecht, 1996.
- [93] F. Meier and G. Eigenberger. Transport parameters for the modelling of water transport in ionomer membranes for PEM-fuel cells. *Electrochim. Acta*, 49(11):1731–1742, 2004.
- [94] M. Schalenbach, W. Lueke, and D. Stolten. Hydrogen Diffusivity and Electrolyte Permeability of the Zirfon PERL Separator for Alkaline Water Electrolysis. *J. Electrochem. Soc.*, 163(14):F1480–F1488, 2016.
- [95] F. Barbir. PEM electrolysis for production of hydrogen from renewable energy sources. *Sol. Energy*, 78(5):661–669, 2005.
- [96] S. S. Kocha, J. Deliang Yang, and J. S. Yi. Characterization of gas crossover and its implications in PEM fuel cells. *AIChE J.*, 52(5):1916–1925, 2006.
- [97] F. Arena, J. Mitzel, and R. Hempelmann. Permeability and Diffusivity Measurements on Polymer Electrolyte Membranes. *Fuel Cells*, 13(1):58–64, 2013.
- [98] M. Inaba, T. Kinumoto, M. Kiriake, R. Umebayashi, A. Tasaka, and Z. Ogumi. Gas crossover and membrane degradation in polymer electrolyte fuel cells. *Electrochim. Acta*, 51(26):5746–5753, 2006.
- [99] K. Broka and P. Ekdunge. Oxygen and hydrogen permeation properties and water uptake of Nafion® 117 membrane and recast film for PEM fuel cell. *J. Appl. Electrochem.*, 27(2):117–123, 1997.
- [100] M. Schalenbach. Corrigendum to “Pressurized PEM water electrolysis: Efficiency and gas crossover” [Int J Hydrogen Energy 38 (2013) 14921–14933]. *Int. J. Hydrogen Energy*, 41(1):729–732, 2016.
- [101] D. Bessarabov, A. Kruger, S. M. Luopa, J. Park, A. A. Molnar, and K. A. Lewinski. Gas Crossover Mitigation in PEM Water Electrolysis: Hydrogen Cross-over Benchmark Study of 3M’s Ir-NSTF Based Electrolysis Catalyst-Coated Membranes. *ECS Transactions*, 75(14):1165–1173, 2016.
- [102] Z. H. Wang and C. Y. Wang. Mathematical Modeling of Liquid-Feed Direct Methanol Fuel Cells. *J. Electrochem. Soc.*, 150(4):A508, 2003.
- [103] Bo Han, J. Mo, Z. Kang, and F.-Y. Zhang. Effects of membrane electrode assembly properties on two-phase transport and performance in proton exchange membrane electrolyzer cells. *Electrochim. Acta*, 188:317–326, 2016.
- [104] M.R.J. Wyllie. *Petroleum production handbook: relative permeabilities*. 1962.

- [105] D. Tehlar, R. Flückiger, A. Wokaun, and F. N. Büchi. Investigation of Channel-to-Channel Cross Convection in Serpentine Flow Fields. *Fuel Cells*, 10(6):1040–1049, 2010.
- [106] J. T. Gostick, M. W. Fowler, M. D. Pritzker, M. A. Ioannidis, and L. M. Behra. In-plane and through-plane gas permeability of carbon fiber electrode backing layers. *J. Power Sources*, 162(1):228–238, 2006.
- [107] J. Benziger, J. Nehlsen, D. Blackwell, T. Brennan, and J. Itescu. Water flow in the gas diffusion layer of PEM fuel cells. *J. Membrane Sci.*, 261(1-2):98–106, 2005.
- [108] M. Wang, Zhi Wang, and Z. Guo. Water electrolysis enhanced by super gravity field for hydrogen production. *Int. J. Hydrogen Energ.*, 35(8):3198–3205, 2010.
- [109] T. Rosén, J. Eller, J. Kang, N. I. Prasianakis, J. Mantzaras, and F. N. Büchi. Saturation Dependent Effective Transport Properties of PEFC Gas Diffusion Layers. *J. Electrochem. Soc.*, 159(9):F536–F544, 2012.
- [110] *VDI-Wärmeatlas*. Springer, Berlin, 10., bearb. und erw. Aufl. edition, 2006.
- [111] P. J.S. Vie and S. Kjelstrup. Thermal conductivities from temperature profiles in the polymer electrolyte fuel cell. *Electrochim. Acta*, 49(7):1069–1077, 2004.
- [112] S.-K. Lee, K. Ito, T. Ohshima, S. Noda, and K. Sasaki. In Situ Measurement of Temperature Distribution across a Proton Exchange Membrane Fuel Cell. *Electrochem. Solid St.*, 12(9):B126, 2009.
- [113] S. Goswami, S. Klaus, and J. Benziger. Wetting and absorption of water drops on Nafion films. *Langmuir*, 24(16):8627–8633, 2008.
- [114] P. Majsztrik, A. Bocarsly, and J. Benziger. Water permeation through Nafion membranes: the role of water activity. *J. Phys. Chem. B*, 112(51):16280–16289, 2008.
- [115] Q. Zhao, P. Majsztrik, and J. Benziger. Diffusion and interfacial transport of water in Nafion. *J. Phys. Chem. B*, 115(12):2717–2727, 2011.
- [116] B. Bensmann, R. Hanke-Rauschenbach, and K. Sundmacher. In-situ measurement of hydrogen crossover in polymer electrolyte membrane water electrolysis. *Int. J. Hydrogen Energ.*, 39(1):49–53, 2014.
- [117] D. L. Wise and G. Houghton. The diffusion coefficients of ten slightly soluble gases in water at 10–60°C. *Chem. Eng. Sci.*, 21(11):999–1010, 1966.
- [118] S. Shibata. The concentration of molecular hydrogen on the platinum cathode. *Bull. Chem. Soc. Jpn.*, 36(1):53–57, 1963.
- [119] H. Matsushima, D. Kiuchi, and Y. Fukunaka. Measurement of dissolved hydrogen supersaturation during water electrolysis in a magnetic field. *Electrochim. Acta*, 54(24):5858–5862, 2009.
- [120] H. Vogt. Interfacial supersaturation at gas evolving electrodes. *J. Appl. Electrochem.*, 23(12), 1993.
- [121] Y. Tanaka, K. Kikuchi, Y. Saihara, and Z. Ogumi. Bubble visualization and electrolyte dependency of dissolving hydrogen in electrolyzed water using Solid-Polymer-Electrolyte. *Electrochim. Acta*, 50(25-26):5229–5236, 2005.
- [122] R. Hiegbe. The rate of absorption of a pure gas into a still liquid during short period of exposure. *Trans. Am. Inst. Chem. Eng.*, 31:365–389, 1935.
- [123] W. G. Whitman. The two film theory of gas absorption. *Chem. Metall Eng.*, 29(4):146–149, 1923.
- [124] M. Ohishi, Y. Ono, and K. Fushinobu. Measurement of Gas Transport Characteristics in PEFC Electrolyte Membrane by Using Microprobes. *Nanosc. Microsc. Therm.*, 17(2):69–78, 2013.

- [125] B. Benschmann, R. Hanke-Rauschenbach, G. Müller-Syring, M. Henel, and K. Sundmacher. Optimal configuration and pressure levels of electrolyzer plants in context of power-to-gas applications. *Appl. Energ.*, 167:107–124, 2016.
- [126] S. Shibata. Supersaturation of oxygen in acidic solution in the vicinity of an oxygen-evolving platinum anode. *Electrochim. Acta*, 23(7):619–623, 1978.
- [127] K. Kikuchi, Aoi Ioka, T. Oku, Y. Tanaka, Y. Saihara, and Z. Ogumi. Concentration determination of oxygen nanobubbles in electrolyzed water. *J. Colloid Interf. Sci.*, 329(2):306–309, 2009.
- [128] A. Z. Weber and J. Newman. Transport in Polymer-Electrolyte Membranes. *J. Electrochem. Soc.*, 151(2):A311, 2004.
- [129] F. Hegge, R. Moroni, P. Trinke, B. Benschmann, R. Hanke-Rauschenbach, S. Thiele, and S. Vierrath. Three-dimensional microstructure analysis of a polymer electrolyte membrane water electrolyzer anode. *J. Power Sources*, 393:62–66, 2018.
- [130] S. S. Kocha. Electrochemical Degradation. In M. M. Mench, editor, *Polymer electrolyte fuel cell degradation*, pages 89–214. Academic Press, Oxford, 2012.
- [131] T. E. Springer. Polymer Electrolyte Fuel Cell Model. *J. Electrochem. Soc.*, 138(8):2334, 1991.
- [132] A. Z. Weber and J. Newman. Macroscopic Modeling of Polymer-Electrolyte Membranes. In K.-D. Kreuer, T. van Nguyen, and T. Zhao, editors, *Advances in Fuel Cells*, volume 1 of *Advances in Fuel Cells*, pages 47–117. Elsevier professional, s.l., 2007.
- [133] M. Nič, Jiří Jirátk, B. Kořata, A. Jenkins, and Alan McNaught. *IUPAC Compendium of Chemical Terminology*. IUPAC, Research Triangle Park, NC, 2009.
- [134] B. Benschmann and R. Hanke-Rauschenbach. (Invited) Engineering Modeling of PEM Water Electrolysis: A Survey. *ECS Transactions*, 75(14):1065–1072, 2016.
- [135] M. B. Satterfield and J. B. Benziger. Non-Fickian water vapor sorption dynamics by Nafion membranes. *J. Phys. Chem. B*, 112(12):3693–3704, 2008.
- [136] C. Ziogou, S. Voutetakis, S. Papadopoulou, and M. C. Georgiadis. Modeling, simulation and experimental validation of a PEM fuel cell system. *Comput. Chem. Eng.*, 35(9):1886–1900, 2011.
- [137] M. Grötsch, R. Hanke-Rauschenbach, and M. Mangold. Bifurcation Analysis of a Two-Phase PEMFC Model. *J. Fuel Cell Sci. Tech.*, 5(2):021001, 2008.
- [138] W. He, Jung S. Yi, and T. van Nguyen. Two-phase flow model of the cathode of PEM fuel cells using interdigitated flow fields. *AIChE J.*, 46(10):2053–2064, 2000.
- [139] J. W. Veldsink, R.M.J. van Damme, G. F. Versteeg, and W.P.M. van Swaaij. The use of the dusty-gas model for the description of mass transport with chemical reaction in porous media. *Chem. Eng. J. Bioch. Eng.*, 57(2):115–125, 1995.
- [140] Chao Si, X.-D. Wang, W.-M. Yan, and T.-H. Wang. A Comprehensive Review on Measurement and Correlation Development of Capillary Pressure for Two-Phase Modeling of Proton Exchange Membrane Fuel Cells. *J. Chem.*, 2015(1):1–17, 2015.
- [141] P. Trinke, B. Benschmann, and R. Hanke-Rauschenbach. Current density effect on hydrogen permeation in PEM water electrolyzers. *Int. J. Hydrogen Energ.*, 42(21):14355–14366, 2017.
- [142] Toray. Toray Industries Inc., GDL specification sheet.
- [143] J. C. Cruz, V. Baglio, S. Siracusano, R. Ornelas, L. Ortiz-Frade, L. G. Arriaga, V. Antonucci, and A. S. Aricò. Nanosized IrO₂ electrocatalysts for oxygen evolution reaction in an SPE electrolyzer. *J. Nano. Res.*, 13(4):1639–1646, 2011.

- [144] Gen Inoue, K. Yokoyama, J. Ooyama, T. Terao, T. Tokunaga, N. Kubo, and M. Kawase. Theoretical examination of effective oxygen diffusion coefficient and electrical conductivity of polymer electrolyte fuel cell porous components. *J. Power Sources*, 327:610–621, 2016.
- [145] Q. Duan, H. Wang, and J. Benziger. Transport of liquid water through Nafion membranes. *J. Membrane Sci.*, 392-393:88–94, 2012.
- [146] A. Z. Weber and J. Newman. Effects of Microporous Layers in Polymer Electrolyte Fuel Cells. *J. Electrochem. Soc.*, 152(4):A677, 2005.
- [147] H. Kim, M.-S. Kang, D. H. Lee, J. Won, J. Kim, and Y. S. Kang. Proton exchange membranes with high cell performance based on Nafion/poly(p-phenylene vinylene) composite polymer electrolyte. *J. Membrane Sci.*, 304(1-2):60–64, 2007.
- [148] R. García-Valverde, N. Espinosa, and A. Urbina. Simple PEM water electrolyser model and experimental validation. *Int. J. Hydrogen Energy.*, 37(2):1927–1938, 2012.
- [149] H. Wu, P. Berg, and X. Li. Non-isothermal transient modeling of water transport in PEM fuel cells. *J. Power Sources*, 165(1):232–243, 2007.
- [150] M. Siemer, T. Marquardt, G. Valadez Huerta, and S. Kabelac. Local Entropy Production Rates in a Polymer Electrolyte Membrane Fuel Cell. *J. Non-Equil. Thermody.*, 42(1):1–30, 2017.
- [151] H. Wu, X. Li, and P. Berg. Numerical analysis of dynamic processes in fully humidified PEM fuel cells. *Int. J. Hydrogen Energy.*, 32(12):2022–2031, 2007.
- [152] K. C. Neyerlin, W. Gu, J. Jorne, A. Clark, and H. A. Gasteiger. Cathode Catalyst Utilization for the ORR in a PEMFC. *J. Electrochem. Soc.*, 154(2):B279, 2007.
- [153] U. Babic, T. J. Schmidt, and L. Gubler. Communication—Contribution of Catalyst Layer Proton Transport Resistance to Voltage Loss in Polymer Electrolyte Water Electrolyzers. *J. Electrochem. Soc.*, 165(15):J3016–J3018, 2018.
- [154] B. Benschmann, R. Hanke-Rauschenbach, I. K. Peña Arias, and K. Sundmacher. Energetic evaluation of high pressure PEM electrolyzer systems for intermediate storage of renewable energies. *Electrochim. Acta*, 110:570–580, 2013.
- [155] P. Trinke, B. Benschmann, and R. Hanke-Rauschenbach. Experimental evidence of increasing oxygen crossover with increasing current density during PEM water electrolysis. *Electrochem. Commun.*, 82:98–102, 2017.
- [156] NIST Chemistry WebBook, NIST Standard Reference Database 69, doi.org/10.18434/T4D303, last access: 10.12.2019.
- [157] R. Battino, editor. *Oxygen and ozone*, volume 7 of *Solubility data series*. Pergamon Press, Oxford, 1981.
- [158] K. Onda, T. Murakami, T. Hikosaka, M. Kobayashi, R. Notu, and K. Ito. Performance Analysis of Polymer-Electrolyte Water Electrolysis Cell at a Small-Unit Test Cell and Performance Prediction of Large Stacked Cell. *J. Electrochem. Soc.*, 149(8):A1069, 2002.
- [159] J. O. Hirschfelder, C. F. Curtiss, and R. B. Bird. *Molecular theory of gases and liquids*. Structure of matter series. Wiley, New York, NY, corr. print. with notes added. edition, 1964.
- [160] NIST data: <https://janaf.nist.gov/tables/H-063.html>, last access: 10.12.2019.

A Supporting Equations

The appendix A includes the supporting equations, parameters of the described model (s. ch. 6). In Tab. A.1 the supporting equations for the charge balances are listed. In the Tabs. A.2 till A.4 the supporting equations for the mass balances are summarized. And Tab. A.5 shows the supporting equations for the energy balance.

Table A.1: Supporting equations for the charge balances (s. sec. 6.1).

Equation with parameters	Note/Source
$\kappa_p = (0.514 \text{ S m}^{-1} \lambda - 0.326 \text{ S m}^{-1}) \exp \left[1268 \text{ K} \left(\frac{1}{303 \text{ K}} - \frac{1}{T} \right) \right]$ (A.1)	Springer et al. [131]
$i_0 = i_0^{\text{ref}} \exp \left[E_A (RT)^{-1} \right]$ (A.2)	$a_{\text{cat}} = 6 \varepsilon_{\text{cat}} d_{\text{cat}}^{-1}$ (A.3)
$E_{\text{rev}}^0 = 1.478 \text{ V} - 8.347 \cdot 10^{-4} \text{ V K}^{-1} T$ (A.4)	Activation energy E_A from [148] Based on data from NIST [156]

Table A.2: Supporting equations for the dissolved gas mass balances (s. sec. 6.2.1).

Equation with parameters	Note/Source
$D_{\text{dsg},i} = D_{\text{dsg},i}^0 \exp \left(\frac{-E_i}{RT} \right)$ (A.5)	$c_{\text{dsg}}^{\text{sat}} = p_i S_i$ (A.6)
$i = \text{H}_2: D_{\text{dsg},\text{H}_2}^0 = 4.9 \cdot 10^{-7} \text{ m}^2 \text{ s}^{-1}, E_{\text{H}_2} = 16.51 \cdot 10^3 \text{ J mol}^{-1}$	Arrhenius Eq. and Henry's law Hydrogen diffusion parameters from [117]
$i = \text{O}_2: D_{\text{dsg},\text{O}_2}^0 = 4.2 \cdot 10^{-7} \text{ m}^2 \text{ s}^{-1}, E_{\text{O}_2} = 18.38 \cdot 10^3 \text{ J mol}^{-1}$	Oxygen diffusion parameters from [117]
$S_i = 0.55 \exp \left[A_i + \frac{B_i}{T} + C_i \ln \left(\frac{T}{100 \text{ K}} \right) \right] \text{ in } \frac{\text{mol}}{\text{m}^3 \text{ Pa}}$ (A.7)	Original Eq. (A.2) stated as the mole fraction [66]
$i = \text{H}_2: A_{\text{H}_2} = -48.1611, B_{\text{H}_2} = 5528.45 \text{ K}, C_{\text{H}_2} = 16.8893$	Hydrogen solubility parameters from [87]
$i = \text{O}_2: A_{\text{O}_2} = -66.73538, B_{\text{O}_2} = 8747.547 \text{ K}, C_{\text{O}_2} = 24.45264$	Oxygen solubility parameters from [157]
$\varepsilon_{\text{H}_2\text{O}} = \frac{\lambda \frac{M_{\text{H}_2\text{O}}}{\rho_l}}{\frac{EW}{\rho_{\text{dry}}^{\text{ion}}} + \lambda \frac{M_{\text{H}_2\text{O}}}{\rho_l}}$ (A.8)	$EW = 1.1 \text{ kg mol}^{-1}, \varrho_{\text{dry}}^{\text{ion}} = 2000 \text{ kg m}^{-3}$ from [128]

Table A.3: Supporting equations for the dissolved water mass balance (s. sec. 6.2.2).

Equation with parameters	Note/Source
$n_{\text{drag}} = (0.0134 \text{ K}^{-1} T + 0.03) \frac{\lambda}{\lambda_{\text{sat}}} \quad (\text{A.9})$	Combination of $f(T)$ from Onda et al. [158] and $f(\lambda)$ from Springer et al. [131]
$D_{\text{dsw}}^{\text{eff}} = (3.6\lambda - 7.8) \cdot 10^{-6} \exp(-3350 \text{ K } T^{-1}) \text{ in m}^2/\text{s} \quad (\text{A.10})$	Fitted on data of Zhao et al. [115]
$c_{\text{dsw}} = \lambda \left(\frac{EW}{\rho_{\text{dry}}^{\text{ion}}} + \lambda \frac{M_{\text{H}_2\text{O}}}{\rho_l} \right)^{-1} \quad (\text{A.11})$	$EW = 1.1 \text{ kg mol}^{-1}$, $\rho_{\text{dry}}^{\text{ion}} = 2000 \text{ kg m}^{-3}$ from [128]

Table A.4: Supporting equations for the gas and liquid mass balances (s. sec. 6.2.3).

Equation with parameters	Note/Source
$c_{\text{g},i} = p_{\text{g},i} T R^{-1} \quad (\text{A.12})$	Gaseous and liquid concentrations
$c_l = M_{\text{H}_2\text{O}} \varrho_l^{-1} \quad (\text{A.13})$	
$\mu_i = \mu_i^0 \frac{T^0 + C_i}{T + C_i} \left(\frac{T}{T^0} \right)^{1.5} \quad (\text{A.14})$	Dynamic viscosity of gases: Sutherland's law fitted on data [110], $T^0 = 298 \text{ K}$
$y_i = p_{\text{g},i} p_{\text{g}}^{-1} \quad (\text{A.15})$	Viscosity w/o correction factor
$\mu_{\text{g}} = \sum_i y_i \mu_i \quad (\text{A.16})$	
$\mu_l = 16.8 \cdot 10^{-6} 10^{308.5 \text{ K}(T-120.2 \text{ K})^{-1}}, \text{ in Pa s} \quad (\text{A.17})$	Fitted on data [110]
$D_{ij}^{\text{free}} = \frac{AT^{1.5} \sqrt{M_i^{-1} + M_j^{-1}}}{p_{\text{g}} \sigma_{ij}^2 \Omega} \quad (\text{A.18})$	Chapman-Enskog theory, parameters from Hirschfelder et al. [159]
$D_i^{\text{free}} = \frac{1 - y_i}{\sum_j \frac{\varepsilon_{\text{pore}}}{\tau_{\text{pore}}} \frac{y_j}{D_{ij}^{\text{free}}}} \quad (\text{A.19})$	
$D_i^{\text{Kn}} = \frac{1}{3d_{\text{pore}}} \sqrt{\frac{8RT}{\pi M_i}} \quad (\text{A.20})$	Knudsen diffusion coef. [79]
$k_{\text{g}}^{\text{rel}} = (1 - s_l)^3 \quad (\text{A.21})$	Wyllie's cubic law [104]
$k_l^{\text{rel}} = s_l^3 \quad (\text{A.22})$	
$p_{\text{c}} = \begin{cases} \gamma \cos(\theta_{\text{phil}}) \sqrt{\frac{\varepsilon}{K}} J \left(1 - \frac{s_l}{f_{\text{phil}}} \right) & , \text{ if } s_l \leq f_{\text{phil}} \\ \gamma \cos(\theta_{\text{phob}}) \sqrt{\frac{\varepsilon}{K}} J \left(\frac{s_l - f_{\text{phil}}}{1 - f_{\text{phil}}} \right) & , \text{ if } s_l > f_{\text{phil}} \end{cases} \quad (\text{A.23})$	Capillary pressure [137]
$J(x) = 1.417(x) - 2.12(x)^2 + 1.262(x)^3 \quad (\text{A.24})$	Leverett J-function [140]
$\gamma = 0.07275 \text{ N m}^{-1} (1 - 0.002 \text{ K}^{-1}(T - 291 \text{ K})) \quad (\text{A.25})$	Eötvös rule fitted on data from [110]
$p_{\text{vap}}^{\text{sat}} = 10^{4.6543 - 1435.264 \text{ K}(T - 64.848 \text{ K})^{-1}} \cdot 10^5 \text{ Pa} \quad (\text{A.26})$	Antoine equation: Stull [89]
$k_{\text{vap}} = \frac{Sh D_{\text{vap}}}{d_{\text{pore}}} \quad (\text{A.27})$	Assumed by a minimal Sherwood number of 2

Table A.5: Supporting equations for the energy balance (s. sec. 6.3).

Equation with parameters	Note/Source
$\Delta S = 193 - 0.1 T$, in $\text{J mol}^{-1} \text{K}^{-1}$ (A.28)	Based on data from NIST [156]
$\Delta H^{\text{vap}} = 4514 (T_c - T)^{0.3836}$, in J mol^{-1} ; $T_c = 647.1 \text{ K}$ (A.29)	Fitted on data from [110]
$\Delta H^{\text{recomb}} = -31.62 \text{ J K}^{-1} \text{ mol}^{-1} T + 295\,527 \text{ J mol}^{-1}$ (A.30)	Fitted on data from [160]

List of Abbreviations and Symbols

Abbreviations and Indices

★	Actual
0	Standard Conditions
a	Anode
aCL	Anode Catalyst Layer
act	Activation
AEL	Alkaline Electrolysis
aPTL	Anode Porous Transport Layer
BV	Butler-Volmer
c	Cathode
cat	Catalyst, Catalyst Particles
cCL	Cathode Catalyst Layer
CCM	Catalyst Coated Membrane
CL	Catalyst Layer
cons	Consumption
conv	Convective
cPTL	Cathode Porous Transport Layer
cross	Crossover
DC	Direct Current
DI	Deionized
diff	Diffusion
drag	Electro-osmotic Drag Coefficient
dry	dry - w/o Liquid Water, w/o Water Vapor
dsg	Dissolved Gas
dsw	Dissolved Water
e	Electron
EDS	Energy-Dispersive X-ray Spectrometry
eff	Effective
EIS	Electrochemical Impedance Spectroscopy
el	Electric
entr	Entropy
evo	Evolution
FIB	Focused Ion Beam
g	Gas
GC	Gas Chromatography
GDL	Gas Diffusion Layer
HER	Hydrogen Evolution Reaction
HFR	High Frequency Resistance
hyd	Hydraulic
ion	Ionomer

joule	Joule Heating
Kn	Knudsen
l	liquid
LEL	Lower Explosion Limit
LFR	Low Frequency Resistance
MEA	Membrane Electrode Assembly
mem	Membrane
MFC	Mass Flow Controller
MPL	Micro Porous Layer
mt	Mass Transport
mtf	Mass Transfer
mtx	Mass Transport and X
OER	Oxygen Evolution Reaction
ORR	Oxygen Reduction Reaction
out	Outlet
ox	Oxidation
P	Permeation
p	Proton
PCV	Pressure Control Valve
PEM	Polymer Electrolyte Membrane
PFSA	Perfluorosulfonic Acid
PGM	Platinum Group Metals
phil	Hydrophilic
phob	Hydrophobic
pore	Pore, Pore Space
PTFE	Polytetrafluoroethylene
PTL	Porous Transport Layer
recomb	Recombination
red	Reduction
ref	Reference
rel	Relative
RQ	Research Question
sat	Saturation
SEM	Scanning Electron Microscope
SOE	Solid Oxide Electrolysis
sorp	Sorption/Desorption
theo	Theoretical
vap	Vapor, Vaporization
Symbols with Greek letters	
α	Charge Transfer Coefficient
Δ	Difference, Nabla Operator
δ	Thickness
η	Efficiency
η_{act}	Activation overvoltage
γ	Surface Tension

κ	Conductivity
λ	Ionomer Water Content
λ_T	Thermal Conductivity
μ	Dynamic Viscosity
σ	Source/Sink Term
τ	Tortuosity
θ	Contact Angle
ε	Porosity/Volume Fraction
φ	Potential
ρ	Density

Symbols with Latin letters

A	Area
a	Volume Specific Surface
b	Tafel Slope
c	Concentration
D	Diffusion Coefficient
d	Diameter, Film Thickness
E	Half-cell Potential
E_A	Activation Energy
EW	Equivalent Weight
f	Hydrophilic Fraction
H	Enthalpy
I	Current
i	Current Density
i_0	Exchange Current Density
J	Leverett Function
j	Running Index for H ₂ , O ₂ and Water Vapor
K	Permeability
k	Mass Transfer Coefficient, Reaction Constant
L	Loading
M	Molecular Mass
N	Molar Fluxes
n_{drag}	Electro-osmotic Drag Coefficient
p	Pressure, Partial Pressure
R	Area Normalized Resistances
S	Solubility Coefficient, Entropy
s	Saturation
Sh	Sherwood Number
T	Temperature
U	Voltage
v	Velocity
y	Gas Volume Fraction
z	Number of Transferred Electrons
F	Faraday Constant
R	Gas Constant

96 485 A s mol⁻¹
8.314 J mol⁻¹ K⁻¹

Scientific Career

Curriculum Vitae

Work Experiences

11/2014 – today **Research Assistant** at the Institute for Electric Power Systems (IfES) – Electric Energy Storage Systems with the following topic: experimental and model-based analysis of the gas crossover in PEM water electrolysis

Study and School

04/2013 – 10/2014 **Study of Process Engineering**, Master of Science at the Otto-von-Guericke-Universität Magdeburg: “Parameterermittlung und Sensitivitätsanalyse eines 3D-PEM-Brennstoffzellen-Simulationsmodells”, grade of the thesis: 1.0, final grade: 1.2

03/2014 – 10/2014 **Internship and Master Thesis** at Volkswagen AG: formulation and implementation of a dynamic model for fast parametrization of an internal 3D-PEM fuel cell model.

10/2013 – 01/2014 **Research Project** at the Max Planck Institute for Dynamics of Complex Technical Systems in Magdeburg: Implementation of a state model for an PEM electrolyzer model

04/2012 – 10/2014 **Scholar** in the “Deutschland-Stipendium” program

10/2009 – 05/2013 **Study of Process Engineering**, Bachelor of Science at the Otto-von-Guericke-Universität Magdeburg: “Experimentelle Ermittlung des Wärmeübergangs bei Einsatz von Flachstrahlröhren zur Kühlung aufgeheizter Bleche”, grade of the thesis: 1.0, final grade: 1.8

02/2013 – 08/2013 **Bachelor Thesis and Student Assistant** at the Institute of Fluid Dynamics and Thermodynamics: modification and commissioning of a test stand for the measuring of the heat transfer coefficient and automation of the data evaluation

08/2012 – 11/2012 **Industrial Internship** at Solvay in Bad Hönningen: Development of a thermal recovery concept from the process exhaust gases upstream of a flue-gas desulfurization plant

08/2002 – 06/2009 **Abitur**, Gymnasium Soltau: final grade 2.7

Peer-reviewed Journal Publications

- C. Immerz, B. Bensmann, P. Trinke, M. Suermann and R. Hanke-Rauschenbach: Understanding Electrical Under- and Overshoots in Proton Exchange Membrane Water Electrolysis Cells (2019). *J. Electrochem. Soc.* **166** (15), F1200-F1208, doi.org/10.1149/2.0881914jes
- P. Trinke, G. P. Keeley, M. Carmo, B. Bensmann and R. Hanke-Rauschenbach: Elucidating the effect of mass transport resistances on hydrogen crossover and cell performance in PEM water electrolyzers by varying the cathode ionomer content (2019). *J. Electrochem. Soc.* **166** (8), F465-F471, doi.org/10.1149/2.0171908jes
- C. Klose, P. Trinke, T. Böhm, B. Bensmann, S. Vierrath, R. Hanke-Rauschenbach and S. Thiele: Membrane Interlayer with Pt Recombination Particles for Reduction of the Anodic Hydrogen Content in PEM Water Electrolysis (2018). *J. Electrochem. Soc.* **165** (16), F1271-F1277, doi.org/10.1149/2.1241814jes
- C. Immerz, B. Bensmann, P. Trinke, M. Suermann and R. Hanke-Rauschenbach: Local current density and electrochemical impedance measurements within 50 cm single-channel PEM electrolysis cell (2018). *J. Electrochem. Soc.* **165** (16), F1292-F1299, doi.org/10.1149/2.0411816jes
- F. Hegge, R. Moroni, P. Trinke, B. Bensmann, R. Hanke-Rauschenbach, S. Thiele and S. Vierrath: Three-dimensional microstructure analysis of a polymer electrolyte membrane water electrolyzer anode (2018). *J. Power Sources* **393**, 62-66, doi.org/10.1016/j.jpowsour.2018.04.089
- C. Immerz, M. Schweins, P. Trinke, B. Bensmann, M. Paidar, T. Bryston, K. Bouzek and R. Hanke-Rauschenbach: Experimental characterization of inhomogeneity in current density and temperature distribution along a single-channel PEM water electrolysis cell (2018). *Electrochim. Acta* **260** (10), 582-588, doi.org/10.1016/j.electacta.2017.12.087
- P. Trinke, P. Haug, J. Brauns, B. Bensmann, R. Hanke-Rauschenbach and T. Turek: Hydrogen crossover in PEM and alkaline water electrolysis: Mechanisms, direct comparison and mitigation strategies (2018). *J. Electrochem. Soc.* **165** (7), F502-F513, doi.org/10.1149/2.0541807jes
- I. K. Pena Arias, P. Trinke, R. Hanke-Rauschenbach and K. Sundmacher: Understanding PEM fuel cell dynamics: The reversal curve (2017). *Int. J. Hydrogen Energ.* **42** (24), 15818-15827, doi.org/10.1016/j.ijhydene.2017.05.087
- P. Trinke, B. Bensmann and R. Hanke-Rauschenbach: Experimental Evidence of Increasing Oxygen Crossover with Increasing Current Density during PEM Water Electrolysis (2017). *Electrochem. Commun.* **82**, 98-102, doi.org/10.1016/j.elecom.2017.07.018

- P. Trinke, B. Bensmann and R. Hanke-Rauschenbach: Current density impact on hydrogen permeation during PEM water electrolysis (2017). *Int. J. Hydrogen Energ.* **42**, 14355-14366, doi.org/10.1016/j.ijhydene.2017.03.231
- P. Trinke, B. Bensmann, S. Reichstein, R. Hanke-Rauschenbach and K. Sundmacher: Hydrogen permeation in PEM electrolyzer cells operated at asymmetric pressure conditions (2016). *J. Electrochem. Soc.* **163** (11), F3164-F3170, doi.org/10.1149/2.0221611jes

Oral Presentations

- P. Trinke, B. Bensmann and R. Hanke-Rauschenbach: System relevant Observation of Gas Crossover — Necessity of Mitigation Strategies, ICE 2019: 2nd International Conference on Electrolysis, Loen, Norway
- P. Trinke, B. Bensmann and R. Hanke-Rauschenbach: In search of the best Catalyst Layer — Application based Catalyst Design, ModVal 2019: 16th Symposium on Modeling and Experimental Validation of Electrochemical Energy Devices, Braunschweig, Germany
- P. Trinke, B. Bensmann and R. Hanke-Rauschenbach: Modelling of the supersaturation of dissolved gas in PEM electrolysis cells, ModVal 2018: 15th Symposium on Modeling and Experimental Validation of Electrochemical Energy Devices, Aarau, Switzerland
- P. Haug, M. Koj, B. Kreitz, P. Trinke, B. Bensmann, R. Hanke-Rauschenbach and T. Turek: Gas purity in PEM and alkaline water electrolysis, ESEE 2017: 11th European Symposium on Electrochemical Engineering, Prague, Czech Republic
- P. Trinke, B. Bensmann, S. Reichstein, R. Hanke-Rauschenbach and K. Sundmacher: Impact of Pressure and Temperature on H₂ Permeation in PEM Water Electrolyzers Operated at Asymmetric Pressure Conditions, PRiME 2016: Pacific Rim Meeting on Electrochemical and Solid-State Science, Honolulu, Hawaii

Publications and Statements on Authorship

This dissertation contains material that has previously been published by the author in the following peer-reviewed journals: Journal of the Electrochemical Society, International Journal of Hydrogen Energy and Electrochemistry Communications. Below the publications, which were included for this work, are listed with statements on authorship:

- P. Trinke, B. Bensmann and R. Hanke-Rauschenbach: Current density impact on hydrogen permeation during PEM water electrolysis (2017). *Int. J. Hydrogen Energ.* **42**, doi.org/10.1016/j.ijhydene.2017.03.231. The author planned and carried out the experiments. He analyzed the data and wrote the manuscript. The co-authors were assisting in the writing of the manuscript. The co-authors supported the writing process. Parts of this paper are included in the following chapters: 2, 3 and 4.
- P. Trinke, B. Bensmann and R. Hanke-Rauschenbach: Experimental Evidence of Increasing Oxygen Crossover with Increasing Current Density during PEM Water Electrolysis (2017). *Electrochem. Commun.* **82**, doi.org/10.1016/j.elecom.2017.07.018. The author planned and carried out the experiments. He analyzed the data and wrote the manuscript. The co-authors supported the writing process. Parts of this paper are included in the following chapters: 3 and 4.
- P. Trinke, G. P. Keeley, M. Carmo, B. Bensmann and R. Hanke-Rauschenbach: Elucidating the effect of mass transport resistances on hydrogen crossover and cell performance in PEM water electrolyzers by varying the cathode ionomer content (2019). *J. Electrochem. Soc.* **166** (8), doi.org/10.1149/2.0171908jes. The author planned and carried out the experiments. The electrodes and the physical characterization were done at the Forschungszentrum Jülich. The author analyzed the data and wrote the manuscript. The co-authors supported the writing process. Parts of this publication are included in the following chapters: 3 and 5.

Chapter 6 and 7 include the model formulation and analysis of different effects by means of the implemented model. This is based on a not yet submitted manuscript of P. Trinke, B. Bensmann and R. Hanke-Rauschenbach. The author formulated and implemented the model. He carried out the simulations, analyzed the data and wrote the manuscript. The co-authors supported the writing process.